이학박사 학위논문

Lattice preferred orientation and dislocation microstructure of olivine and amphibole: Implications for microstructural evolution and seismic anisotropy

감람석과 각섬석의 격자선호방향과 전위미세구조:
미구조 진화와 지진파 비등방성에의 적용

2020년 8월

서울대학교 대학원

지구환경과학부

정 세 진

Lattice preferred orientation and dislocation microstructure of olivine and amphibole: Implications for microstructural evolution and seismic anisotropy

지도 교수 정 해 명

이 논문을 이학박사 학위논문으로 제출함
2020년 7월

서울대학교 대학원
지구환경과학부
정 세 진

정세진의 이학박사 학위논문을 인준함
2020년 7월

위 원 장 _____ 이 인 성 (인)

부위원장 _____ 정 해 명 (인)

위 원 _____ 길 영 우 (인)

위 원 _____ 이 준 기 (인)

위 원 _____ 박 문 재 (인)

ABSTRACT

Lattice preferred orientation and dislocation microstructure of olivine and amphibole: Implications for microstructural evolution and seismic anisotropy

Sejin Jung
School of Earth and Environmental Sciences
The Graduate School
Seoul National University

Seismic anisotropy observed in the mantle wedge and subducting slab may be largely influenced by lattice preferred orientation (LPO) of olivine and amphibole. LPO of the minerals can be developed in dislocation creep and, therefore, it is important to understand dislocation microstructure and dominant slip system of the minerals. In this thesis, LPOs of olivine and tremolite and dislocation microstructures of olivine in the amphibole peridotites in Åheim, Norway, were analyzed to understand deformation condition and microstructural evolution of amphibole peridotites during the orogenic event and their implications for seismic anisotropy in the mantle wedge. In addition, microstructures of experimentally deformed amphibole (glaucophane) in blueschists were studied to understand the dislocation slip system of amphibole and to understand fault zone properties at the top of a subducting slab. LPO of the mineral was determined by an electron back-scattered diffraction (EBSD) analysis and the slip system of dislocation was determined by a transmission electron microscope (TEM).

Åheim amphibole peridotites showed a porphyroclastic texture with abundant subgrain boundaries and some samples contained many hydrous minerals such as tremolite. Detailed microstructural analysis on the Åheim peridotites revealed the evidence of multiple stages of deformation. The coarse-grained olivine showed A-type LPO of olivine, which can be interpreted as the initial stage of deformation. The spinel-bearing samples showed a mixture of B-type and C-type LPO of olivine,

which is considered to represent the 2nd stage of deformation under water-rich conditions. The recrystallized fine-grained olivine displays B-type LPO, which can be interpreted as the third stage of deformation under water-rich conditions. The observation of the B-type LPO of olivine is important for an interpretation of trench-parallel seismic anisotropy in the mantle wedge. The calculated seismic anisotropy of the tremolite showed that tremolite can contribute to the trench-parallel seismic anisotropy in the mantle wedge.

The EBSD mapping and the TEM observation of olivine were conducted for the Åheim amphibole peridotites showing both A- and B-type LPO of olivine. The dominant slip system of olivine which was determined by subgrain boundaries was (001)[100] for both samples, and these subgrain boundaries might have resulted from the deformation under moderate water content in olivine or low strain deformation. TEM observation of olivine dislocation with the thickness-fringe method revealed that the free dislocations with (010)[100] slip system of olivine were dominant for both samples. These results suggest that the subgrain boundaries and free dislocations in the olivines represent the later stage deformation associated with the exhumation process. EBSD mapping of the tremolite-rich layer revealed intracrystalline plasticity in the amphibole which can be interpreted as activation of (100)[001] slip system in the tremolite. The LPO of tremolite coincided with the slip system, suggesting that the LPO of tremolite was significantly influenced by the dislocation creep.

To understand the fault-triggering mechanism in the subducting slab and the deformation mechanism of the glaucophane, both lawsonite and epidote blueschist which were deformed experimentally in simple shear were studied. Amorphous material and nanocrystals of glaucophane were found in the fault gouge by TEM observation, which can enable the initiation of the instability by reducing the frictional coefficient of the blueschist. Detailed TEM observation of glaucophane in the epidote blueschist revealed abundant dislocations, which can be evidence of the activation of the dislocation creep.

Keywords: microstructure, lattice preferred orientation, dislocation, slip system, amphibole peridotite, seismic anisotropy.

Student Number: 2011-30922

TABLE OF CONTENTS

LIST OF FIGURES

LIST OF TABLES

LIST OF PUBLICATIONS

Jung, S., Jung, H., Austrheim, H., 2020. Microstructural Evolution of Amphibole Peridotites in Åheim, Norway, and the Implications for Seismic Anisotropy in the Mantle Wedge. *Minerals* 10, 345.

Jung, S., Jung, H., Austrheim, H., 2014. Characterization of olivine fabrics and mylonite in the presence of fluid and implications for seismic anisotropy and shear localization. *Earth Planets Space* 66, 21.

Cao, Y., Jinxue, D., Park, M., **Jung, S.**, Park, Y., Kim, D., Choi, S., Jung, H., Austrheim, H., 2020. Metastability and non-dislocation based deformation mechanisms of the Flem eclogites in the Western Gneiss Region, Norway. *Journal of Geophysical Research: Solid Earth*, in press, doi: 10.1029/2020JB019375.

Cao, Y., Jung, H., Song, S.G., Park, M., **Jung, S.**, Lee, J., 2015. Plastic Deformation and Seismic Properties in Fore-arc Mantles: A Petrofabric Analysis of the Yushigou Harzburgites, North Qilian Suture Zone, NW China. *Journal of Petrology* 56, 1897-1943.

Jung, H., Lee, J., Ko, B., **Jung, S.**, Park, M., Cao, Y., Song, S.G., 2013. Natural type-C olivine fabrics in garnet peridotites in North Qaidam UHP collision belt, NW China. *Tectonophysics* 594, 91-102.

CHAPTER 1

Introduction

Observation of seismic anisotropy has been a powerful tool to obtain information on the upper mantle dynamics, mantle flow, and tectonics (Hess, 1964; Long and Becker, 2010; Long and Silver, 2008; Savage, 1999; Silver, 1996; Smith et al., 2001; Zhao et al., 2016). One of the major factors controlling the seismic anisotropy of the upper mantle and lower crust is lattice preferred orientation (LPO) of the anisotropic minerals developed by the deformation (Ben Ismail and Mainprice, 1998; Jung and Karato, 2001a; Karato et al., 2008; Mainprice, 2007; Nicolas and Christensen, 1987; Tommasi and Vauchez, 2015). Thus, it is crucial to understanding the development of LPO of the mineral by the deformation of the crust and upper mantle. Plastic deformation of the mineral by the motion of dislocation through the glide plane is one of the important mechanisms for the development of the LPO. The relationship between the LPO of mineral and the active slip system of the dislocation is well understood by the various theoretical models such as the Taylor-Bishop-Hill model (Lister et al., 1978; van Houtte and Wagner, 1985) and the self-consistent approach (Molinari et al., 1987; Winger et al., 1980). The LPO of mineral generally follows the easiest slip system of dislocation for the given deformation condition (Karato, 2008; Mainprice and Nicolas, 1989).

The knowledge of the deformation characteristic of olivine, which is the most abundant mineral in the upper mantle condition, is important to understand the physical characteristics and the seismic anisotropy of the upper mantle. Plastic deformation of the olivine in the upper mantle condition can produce LPO of olivine, which has a great influence on the seismic anisotropy of the upper mantle (Ben Ismail and Mainprice, 1998; Jung, 2017; Karato et al., 2008; Nicolas and Christensen, 1987; Skemer and Hansen, 2016). Experimental deformation studies in the high-pressure and temperature condition suggested that there can be various types of olivine LPO depending on the deformation condition and mechanisms such as deformation under water-rich conditions (Jung and Karato, 2001a; Jung et al., 2006), deformation under high pressure (Jung et al., 2009; Ohuchi et al., 2011; Wang et al., 2013), an enhancement of grain boundary sliding (Cao et al., 2017; Hansen et al., 2011; Precigout and Hirth, 2014), diffusional creep (Sundberg and Cooper, 2008), the presence of partial melt (Holtzman et al., 2003; Qi et al., 2018) or the deformation geometry (Mainprice, 2007; Tommasi et al., 2000; Tommasi et al., 1999). For example, the A-type olivine LPO is expected under the dry condition, which is characterized by the [100] axes aligned subparallel to the shear direction and the [010] axes aligned subnormal to the shear plane. Under water-rich conditions, olivine LPO can change to B-, C-, or E-types LPOs (Jung and Karato, 2001; Jung et al., 2006; Katayama et al., 2004). For the B-type LPO, the [001] axes are aligned subparallel to the shear direction, and the [010] axes are aligned normal to the shear plane. For the C-type LPO, the [001] axes are subparallel to the shear direction and the [100] axes are normal to the shear plane. For the E-type LPO, the [100] axes are subparallel to the shear direction and the [001] axes are normal to the shear plane. Fabric transition of olivine in the mantle wedge from the A-type to B-, C, and E-type

LPO of the olivine is suggested as a possible mechanism for the change in the shear wave splitting pattern observed in the subduction zone (Cao et al., 2015; Jung and Karato, 2001a; Jung et al., 2006; Karato et al., 2008; Long and van der Hilst, 2006; Nakajima and Hasegawa, 2004; Precigout and Almqvist, 2014). It is reported that there is a close relationship between the LPO of olivine and the dominant dislocation slip system from high-pressure deformation experiments (Demouchy et al., 2014; Jung et al., 2006; Raterron et al., 2009). But the actual research that reported actual evidence of the correlation between the olivine LPO and the dislocation slip system from the naturally deformed olivine is still very limited.

Amphibole is one of the major components in the middle to lower crust and the LPO of amphibole have a significant influence on the seismic anisotropy of the continental crust (Cao et al., 2010; Ji et al., 2013; Mainprice and Nicolas, 1989; Tatham et al., 2008). Because the amphibole can also be present in the subduction zone as a part of subducting oceanic crust (Schmidt and Poli, 1998) or a product of the hydration reaction of pyroxene (Cao et al., 2016; Evans, 1977), the LPO of the amphibole can also contribute to the seismic anisotropy in the subduction zone (Jung et al., 2020; Kang and Jung, 2019; Kim et al., 2013a; Kim and Jung, 2019; Ko and Jung, 2015). Recent experiment studies reported that four different LPO types (I–IV) of amphibole were produced depending on the temperature, stress, and shear strain (Kim and Jung, 2019; Ko and Jung, 2015). Type-I LPO of amphibole is characterized by the [001] axes aligned subparallel to the shear direction and the [100] axes aligned subnormal to the shear plane. Type-II LPO of amphibole is characterized by the {010 poles aligned subparallel to the shear direction and the [100] axes aligned subnormal

to the shear plane. Type-III LPO of amphibole is characterized by the [001] axes and {010 poles forming a girdle distribution along the shear plane with [100] axes that are aligned subnormal to the shear plane. Type-IV LPO of amphibole is characterized by the [001] axes aligned subparallel to the shear direction and the [100] axes forming a girdle subnormal to the shear plane. Previous studies proposed that the LPO of amphibole can be developed by a variety of deformation mechanisms: rigid body rotation (Aspiroz et al., 2007; Getsinger et al., 2013; Tatham et al., 2008), cataclastic flow (Kim and Jung, 2019; Ko and Jung, 2015; Nyman et al., 1992), or diffusional creep (dissolution–precipitation creep) (Getsinger and Hirth, 2014; Imon et al., 2004). However, dislocation creep is one of the important deformation mechanism for the amphibole (Biermann and Vanroermund, 1983; Cumbest et al., 1989; Morrison-Smith, 1976; Rooney et al., 1975; Skrotzki, 1992) and there is some reports of LPO of amphibole related to the dislocation creep from natural amphibole sample (Cao et al., 2010; Elyaszadeh et al., 2018). However, the study on the relationship between the dislocation slip system and the LPO of amphibole is still limited.

The main research interest in this study is to combine the result of the LPO of mineral determined by an electron back-scattered diffraction (EBSD) and dislocation slip system determined by a transmission electron microscope (TEM) observation. Using the EBSD detector attached to a scanning electron microscope (SEM), the crystallographic orientation of the minerals can be easily and quickly determined and recorded so that the detailed studies on the fabric of the olivine can be performed even for the fine grains or for the specific locations (Adams et al., 1993; Prior et al.,

1999). With the recent progress of the automated EBSD data acquisition, it is possible to identify the intragranular distortion of the mineral, which can provide information relevant to understanding deformation mechanisms and development of LPO (Marquardt et al., 2017; Prior et al., 1999; Wheeler et al., 2001; Wright et al., 2015). By using TEM, it is possible to image specimen micro- to nanoscale and to observe crystalline defects such as dislocations or subgrain boundaries. The slip system of the dislocation can only be precisely determined by using visibility criterion with the weak-beam dark-field images obtained by the TEM observation (Ishida et al., 1980; Miyajima and Walte, 2009). Because the LPO of the mineral and the activation of the dislocation slip system have a close relationship with each other, a true understanding of the fabric development in the various physic-chemical conditions can be obtained when the LPO and dislocation slip system are compared. In addition, the microstructural evolution of the naturally deformed peridotite during the complex deformation history through the orogenic events can also be analyzed.

In Chapter 2, microstructural analysis on the amphibole peridotites in Åheim, Norway, was performed to identify the microstructural evolution of samples during the Scandian orogeny. The EBSD analysis showed that the olivine in the Åheim amphibole peridotites had a different LPOs of olivine depending on the grain size of olivine and the mineral assemblage of peridotite, and these different LPOs of the olivine represent multiple stages of deformation during the orogenic event. Fourier-transform infrared spectroscopy (FTIR) analysis on the olivine revealed that the fabric transition of olivine is related to the fluid infiltration during the exhumation process. Based on the EBSD data, the influence of the partial fabric transition of the olivine on seismic anisotropy in the mantle wedge was simulated. Strong fabric

strength of the amphibole and the resultant seismic anisotropy of the amphibole suggest an important impact of the LPO of the amphibole on seismic anisotropy in the mantle wedge.

In Chapter 3, the deformation mechanism and microstructural evolution of olivine and amphibole in the Åheim amphibole peridotites were studied. The slip system of the olivine was determined by EBSD mapping and TEM observation. Subgrain boundaries can be related to the deformation with moderate water content in olivine or low strain deformation. Free dislocations in the olivines might be resulted from the low-stress deformation. It is found that subgrain boundaries and free dislocations represent the later stage deformation associated with the exhumation process. EBSD mapping of the tremolite-rich layer revealed that (100)[001] slip system was activated in the tremolite and contributed to the development of the LPO of the tremolite.

In Chapter 4, both lawsonite and epidote blueschist which were deformed experimentally in simple shear were studied to understand the fault-triggering mechanism in the subducting slab and the deformation mechanism of the glaucophane. During the TEM observation, amorphous material and nanocrystals were found in the fault gouge crosscutting glaucophane grain. The presence of amorphous materials and nanocrystals in the blueschists might enable the initiation of the instability, which can be related to the fault-triggering mechanism in the subducting slab. The glaucophane in the epidote blueschist showed abundant dislocations and Burgers vector was characterized as [001]. In addition, the possible implication of the dislocation creep in glaucophane to the seismic anisotropy in the

subducting slab was discussed.

CHAPTER 2

Microstructural evolution of amphibole peridotites in Åheim, Norway, and the implications for seismic anisotropy in the mantle wedge

This chapter has been published:

Jung, S., Jung, H., and Austrheim, H., 2020. Microstructural Evolution of Amphibole Peridotites in Åheim, Norway, and the Implications for Seismic Anisotropy in the Mantle Wedge. Minerals, 10, 345.

Abstract

The microstructure of amphibole peridotites from Åheim, Norway were analyzed to understand the evolution of the lattice-preferred orientation (LPO) of olivine throughout the Scandian Orogeny and its implication for the seismic anisotropy of the subduction zone. The Åheim peridotites had a porphyroclastic texture and some samples contained an abundant amount of hydrous minerals such as tremolite. Detailed microstructural analysis on the Åheim peridotites revealed multiple stages of deformation. The coarse grains showed A-type LPO of olivine, which can be interpreted as the initial stage of deformation. The spinel-bearing samples showed a mixture of B-type and C-type LPO of olivine, which is considered to represent the deformation under water-rich conditions. The recrystallized fine-grained olivine displays B-type LPO, which can be interpreted as the final stage of deformation. Microstructures and water content of olivine indicate that the dominant deformation mechanism of olivine showing B-type LPO is dislocation creep under water-rich condition. The observation of the B-type LPO of olivine is important for an interpretation of trench-parallel seismic anisotropy in the mantle wedge. The calculated seismic anisotropy of the tremolite showed that tremolite can contribute to the trench-parallel seismic anisotropy in the mantle wedge.

2.1. Introduction

The deformation behavior of olivine is a key to understanding mantle flow and seismic anisotropy in the upper mantle (Ben Ismail and Mainprice, 1998; Jung, 2017; Karato et al., 2008; Nicolas and Christensen, 1987; Skemer and Hansen, 2016). Many experimental studies concerning the deformation of olivine have reported that it has various types of lattice preferred orientations (LPOs), depending on the physicochemical conditions during its deformation, and that the different LPOs of olivine may influence the seismic anisotropy of the upper mantle (Boneh and Skemer, 2014; Jung and Karato, 2001a; Jung et al., 2006; Karato et al., 2008; Katayama et al., 2004; Ohuchi et al., 2011; Soustelle and Manthilake, 2017). For example, the fabric transition of olivine in the mantle wedge from an A-type to a B-type LPO of olivine is proposed as a possible mechanism for the change in the shear wave splitting pattern observed in the subduction zone (Jung and Karato, 2001a; Jung et al., 2006; Karato et al., 2008; Long and van der Hilst, 2006; Nakajima and Hasegawa, 2004; Precigout and Almqvist, 2014). Many studies have proposed a hypothesis for this change in fabric: deformation under water-rich conditions (Jung and Karato, 2001a; Jung et al., 2006), deformation under high pressure (Jung et al., 2009; Ohuchi et al., 2011; Wang et al., 2013), an enhancement of grain boundary sliding (Cao et al., 2017; Hansen et al., 2011; Precigout and Hirth, 2014), diffusional creep (Sundberg and Cooper, 2008), or the presence of partial melt (Holtzman et al., 2003; Qi et al., 2018). There have been many reports of such fabric transitions recorded in naturally deformed peridotites from various localities: the Bergen arc, Norway (Jung et al., 2014), Ronda massif, Spain (Precigout and Hirth, 2014), Lien, Almklovdalen,

Norway (Kim and Jung, 2015), the Navajo volcanic field, U.S.A. (Behr and Smith, 2016), and the Calatrava volcanic field, Spain (Puelles et al., 2016). However, the exact mechanism for the fabric transition of olivine in the mantle wedge is still under debate.

In subduction zones, various hydrous minerals such as serpentines, chlorites, and amphiboles can be produced via chemical reactions that take place in the presence of fluid released from the subducting slab (Fumagalli and Poli, 2005; Hacker et al., 2003a; Ohtani, 2005; Wada et al., 2012). Hydrous minerals in and near the subducting slab are elastically highly anisotropic (Almqvist and Mainprice, 2017; Lee et al., 2020; Mainprice and Ildefonse, 2009; Mookherjee and Mainprice, 2014), and thus very important for understanding seismic anisotropy at a subduction zone. Many studies have suggested that the trench-parallel shear wave anisotropy observed at various subduction zones (Liu and Zhao, 2017; Long, 2013; Walpole et al., 2017) can be induced by the LPO of hydrous minerals such as serpentine (Jung, 2011; Katayama et al., 2009; Nagaya et al., 2016), chlorite (Kang and Jung, 2019; Kim and Jung, 2015; Mainprice and Ildefonse, 2009), and amphibole (Ji et al., 2013; Kang and Jung, 2019; Kim and Jung, 2019; Ko and Jung, 2015). Amphibole can be present in the mantle wedge above the subducting slab as a product of the hydration reaction of pyroxene (Cao et al., 2016; Evans, 1977). However, studies on the influence of the amphibole fabric on seismic anisotropy in the mantle wedge are still very limited.

In this study, a detailed microstructural analysis of several samples of amphibole peridotite from Åheim, Norway, was performed to understand the evolution of its microstructures during the orogenic event and the subsequent

exhumation processes. The LPO of the olivine in the Åheim amphibole peridotites was analyzed to study the mechanism underlying the fabric transition of olivine in nature and its implication for seismic anisotropy at a subduction zone. The water content was measured using Fourier transform infrared (FTIR) analysis and the dislocation microstructures in the olivine were observed to identify a possible mechanism leading to its deformation. In addition, the LPO of the amphibole was analyzed to estimate the influence of amphibole fabric on seismic anisotropy in a subduction zone.

2.2. Geological setting and sample description

The Western Gneiss Region (WGR) in Norway is located between Bergen and Trondheim, with 25,000 km^2 of dominantly gneissic rocks representing the crustal root zone of the Caledonian mountain belt (Austrheim, 2013; Hacker et al., 2010). The Caledonian mountain belt was originated during the collision between Laurentia and Baltica (Gee, 1975; Roberts, 2003; Soper et al., 1992). The Scandian Orogenic event resulted in a series of high-pressure to ultra-high pressure (HP to UHP) metamorphism events in the WGR. Many orogenic peridotite bodies were emplaced into the crustal rocks of the WGR, which experienced multiple stages of metamorphism and deformation over the course of the Scandian Orogeny and the subsequent uplift (Beyer et al., 2012; Brueckner et al., 2010; Carswell, 1986; Cordellier et al., 1981; Jamtveit et al., 1991; Kylander-Clark et al., 2008; Lapen et al., 2009; Vrijmoed et al., 2006). During exhumation, many peridotite bodies were

infiltrated by fluid and retrograded to amphibole peridotite or chlorite peridotite.

The WGR is predominantly composed of orthogneisses and paragneisses with abundant emplaced peridotite or eclogite bodies (Fig. 2.1). The Proterozoic protolith, dated to 1,654 ± 1 Ma, underwent UHP metamorphism and subsequent retrogression associated with the Scandian Orogenic event (Austrheim et al., 2003; Hacker, 2007). A continent-continent collision between Baltica and Laurentia from 425–400 Ma resulted in HP-UHP metamorphism at P = 1.8–3.6 GPa and T = 600–800 °C (Beyer et al., 2012; Dobrzhinetskaya et al., 1995; Vrijmoed et al., 2006). Following this collision (400–380 Ma), the WGR was uplifted to a depth of 15–20 km where it underwent amphibolite facies retrogression at P = 0.5–1.5 GPa and T = 650–850 °C (Hacker et al., 2010; Kylander-Clark et al., 2008; Root et al., 2005). The orogenic peridotite bodies within the Nordfjord–Stadlandet UHP domains include garnet lherzolite and dunite trapped during the uplift stage. Brueckner et al. (2010) proposed that orogenic peridotites in the central and western WGR including Åheim amphibole peridotite were originated from the lithospheric mantle which were inserted into the crust as slab returned toward the surface. During the uplifting, these peridotites experienced multiple stages of deformation and associated recrystallization in the granulite facies (ol + opx + cpx + sp), high amphibolite facies (ol + opx + amp + sp), and low amphibolite facies (ol + opx + amp + chl) conditions (Brueckner et al., 2010; Carswell, 1986; Cordellier et al., 1981; Jamtveit et al., 1991; Kostenko et al., 2002; Lapen et al., 2009). The amphibole peridotite samples (426, 429, 443, 445, 446, 447, and 448) were collected from the Gusdal quarry in Åheim, Western Norway (Fig. 2.1) for a detailed study of their microstructures.

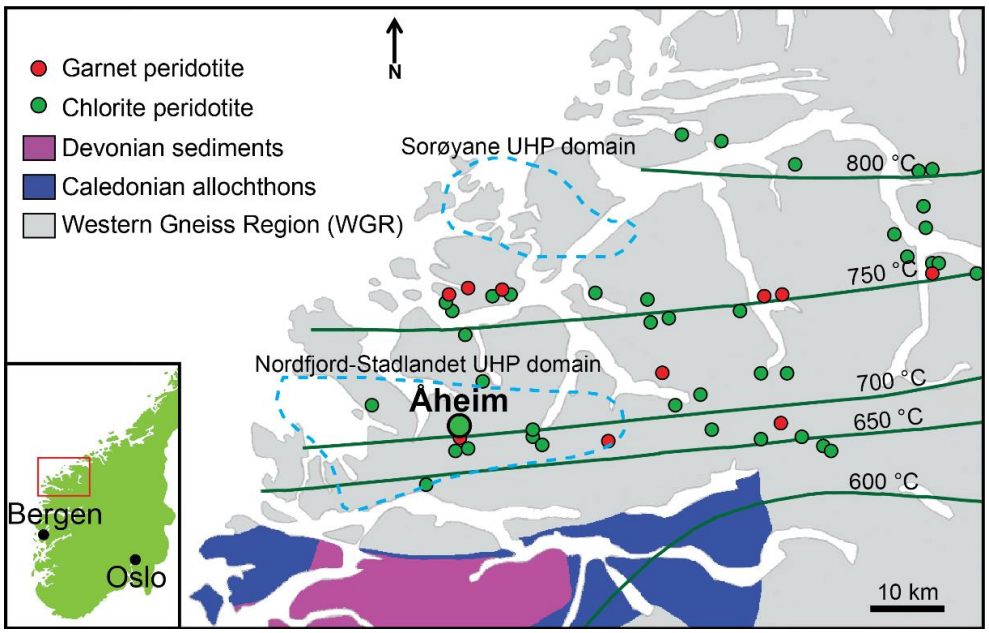

Figure 2.1. Simplified geological map and the distribution of peridotite bodies in the Western Gneiss Region, Norway (modified after Austrheim (2013), Brueckner et al. (2010), Root et al. (2005), and Wang et al. (2013)). Samples are from the Gusdal quarry in Åheim (larger green circle). The green lines indicate the approximate peak metamorphic temperature (Kylander-Clark et al., 2008). Locations of chlorite peridotite and a garnet peridotite body are marked with a green and red circle, respectively. Two UHP domains, Nordfjord-Stadlandet and Sorøyane, are marked by a dotted blue line.

2.3. Experimental method

2.3.1. The chemical composition of minerals

The chemical compositions of the representative minerals were analyzed using a Shimadzu 1600 electron probe micro-analyzer (EPMA), with an accelerating voltage of 15 kV and a beam size of 1 μm, at the Korea Basic Science Institute in Jeonju. Natural silicates and synthetic oxides were used as the Standard materials for the calibration. The chemical composition of the minerals was obtained from their cores. No chemical zoning was detected within the samples.

2.3.2. Measurement of LPO and seismic anisotropy

The foliation of the samples was determined from the compositional layering of the olivine, amphibole, and chlorite. Lineation was determined by examining the shape-preferred orientation of the elongated olivines in the foliation plane using the projection-function method (Panozzo, 1984). LPO of the olivine and tremolite were determined in thin sections which was prepared in the x-z plane (x: lineation, z: normal to foliation) to set the reference frame for comparison with previous studies. An electron backscattered diffraction (EBSD) detector attached to a scanning electron microscope (SEM) (JEOL JSM-6380) housed at the School of Earth and Environmental Sciences (SEES) at Seoul National University (SNU) was used to determine the LPO of each mineral. An HKL system with Channel 5 software was

used for the EBSD analysis. The accelerating voltage and working distance in the SEM observation were 20 kV and 15 mm, respectively. EBSD data was collected in a grid pattern with step size similar to the grain size of each samples so that EBSD data was acquired one point per grain. To ensure an accurate solution, each EBSD pattern of the individual grains was analyzed manually. The fabric strength of the LPO of the olivine and tremolite was calculated using the M-index (Skemer et al., 2005) and J-index (Bunge, 1982).

To estimate the impact that the multiple stages of deformation and presence of hydrous minerals had on the seismic anisotropy, the seismic velocity and anisotropy of the Åheim amphibole peridotites were calculated using the software ANIS2k and VpG (Mainprice, 1990) on the basis of the LPO data. The ambient-condition elastic constants for a single crystal of olivine (Abramson et al., 1997), tremolite (Brown and Abramson, 2016), and antigorite (Bezacier et al., 2010) were used for the crystallographic data. The thickness of the anisotropic layer (T_A) for a given delay time was estimated from shear wave splitting via the following equation (Pera et al., 2003) : $T_A = (100 \times \delta \times < V_S >)/AV_S$, where δ is the delay time of the S-wave, $< V_S >$ is the average velocity of the fast and slow shear waves (V_{S1} and V_{S2}), and AV_S is the seismic anisotropy of the S-wave expressed as a percentage.

2.3.3. *Measurement of water content in olivine*

The water content of the olivine was measured using FTIR spectroscopy. The FTIR specimens were thinned to a thickness of 100 μm and polished on both sides.

Each sample was then heated at a temperature of T = 120 °C for 24 h to eliminate water from the surface and the grain boundary. The FTIR analysis was performed using a Nicolet 6700 FTIR spectrometer with a continuum IR microscope housed at the Tectonophysics laboratory in the SEES at SNU. Unpolarized transmitted light with an aperture size of 50 μm × 50 μm was used to obtain the FTIR spectra. For each sample, FTIR spectra were collected from 10 different olivine grains without any cracks or inclusions, to avoid interference, and averaged. To identify the constituents of the inclusions in the olivine, additional FTIR analysis was performed on olivines with inclusions. A series of 128 scans were averaged for each spectrum to improve the quality of the spectra at a resolution of 4 cm^{-1}. The water content of the olivine was calculated at the wave numbers in the range of 3,400–3,750 cm^{-1} using the calibration method described by Paterson (1982).

2.3.4. *Dislocation microstructure*

An oxygen decoration technique (Jung and Karato, 2001b; Karato, 1987; Kohlstedt et al., 1976) was applied to allow observation of the dislocation microstructures in the olivine. The peridotite samples were polished on a single side with colloidal silica and were heated than in the oven for 1 h at T = 800 °C. Each sample was polished with colloidal silica after oxidation in order to remove the thin layer of oxide from its surface. The polished samples were then coated with carbon to prevent charging during the SEM observation (JEOL JSM-6380). To observe the dislocation microstructures in the olivine, backscattered electron images (BEI) were taken with an accelerating voltage of 15 kV and at a working distance of 10 mm

(Jung and Karato, 2001b).

2.4. Result

2.4.1. Microstructure

The majority of the samples had a porphyroclastic texture and contained primarily olivine (> 90%) with minor amounts of amphibole, orthopyroxene, chlorite, biotite, and chromite (Fig. 2.2A B, C, D), which represents low amphibolite facies (ol + opx + amp + chl) condition mineral assembly (Brueckner et al., 2010; Carswell, 1986; Lapen et al., 2009). However, some samples showed different mineral assemblages and modal compositions. For example, some samples (429 and 445) included layers of Cr-rich spinel (Fig. 2.2B), which can be related to the granulite facies (ol + opx + cpx + sp) or high amphibolite facies (ol + opx + amp + sp) conditions mineral assembly (Brueckner et al., 2010; Carswell, 1986; Lapen et al., 2009). Another sample (443) included a tremolite-rich layer with an approximately 50 % modal composition of tremolite (Fig. 2.2D).

The average grain size of each sample was measured using the linear intercept method (Gifkins, 1970) and the range was found to be 0.32–1.2 mm (Table 2.1) with an average of 0.51 mm. The average size of the grains in sample 448, with its clear porphyroclastic texture, was 0.35 mm for the recrystallized fine grains and 1.2 mm for the coarse grains including the porphyroclasts (Table 2.1). Olivine porphyroclasts

had curvy grain boundaries, indicating a recrystallization process that occurred via grain boundary migration (Fig. 2.2A, C). Straight grain boundaries and triple junctions were often observed in the recrystallized small grains, which indicated that annealing occurred during exhumation (Fig. 2.2C). A few four-grain junctions were also observed in the area of the recrystallized olivine grains (Fig. 2.2E, F). Undulose extinction and subgrain boundaries were frequently observed in all samples (Fig. 2.2A, C). Microstructures such as porphyroclastic texture, undulose extinction, subgrain boundaries, and abundant inclusions or fractures coincided with those of the grey peridotite described by Kostenko et al. (2002).

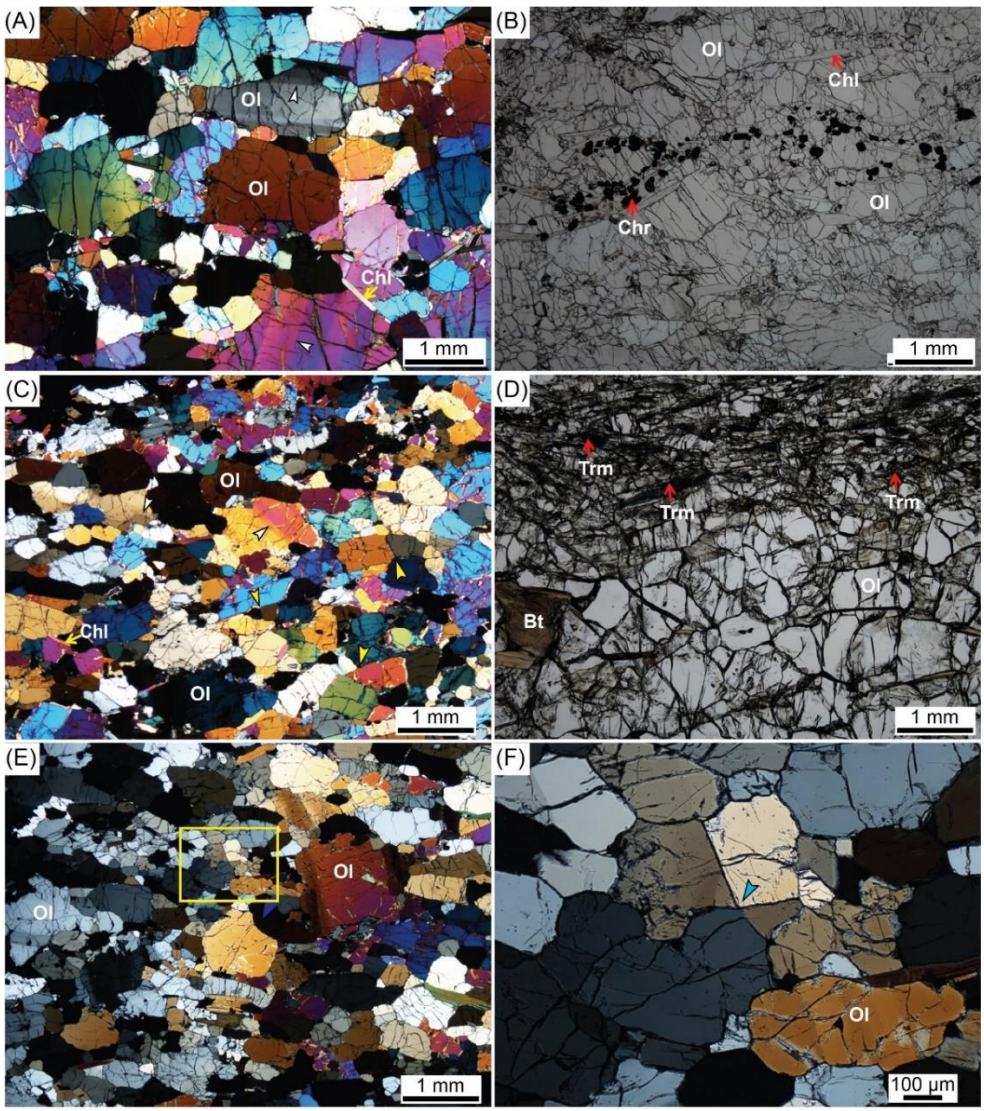

Figure 2.2. Optical photomicrographs of the samples in transmitted light. (A) Representative wide-view images of sample 448. White arrows mark the olivine crystals that show clear subgrain boundaries. Olivine and chlorite grain is indicated as Ol and Chl, respectively. (B) Spinel-rich layer observed in sample 429. Chromite and chlorite grains are indicated as Chr and Chl, respectively. (C) Representative wide-view images of sample 447. White arrows mark the olivine crystals showing clear subgrain boundaries. The yellow arrows mark the location of the triple junctions. Olivine and chlorite grains are indicated as Ol and Chl, respectively. (D)

Tremolite-rich layer observed from sample 443. Tremolite and biotite grains are indicated as Trm and Bt, respectively. (E) Wide view image of sample 447. The yellow rectangle indicates the location of Fig. 2.2F. (F) Four-grain junction is observed in sample 447. The blue arrow marks the location of the four-grain junction.

Table 2.1. The LPO, water content, and fabric strength of olivine.

Sample		LPO type of olivine	Water content of olivine[1] (ppm H/Si)	Average grain size[2] (mm)	M-index[3]	J-index[4]
426		A+B-type	500 ± 50	0.48	0.09	2.98
429	Spinel-rich	B+C-type	320 ± 50	0.36	0.05	2.00
	Spinel-poor	B-type		0.32	0.08	2.86
443	Tremolite-rich	B-type	230 ± 50	0.35	0.05 0.13*	2.34 5.89*
	Tremolite-poor	A-type		0.7	0.08	2.66
445		B+C-type	500 ± 50	0.51	0.05	1.89
446		B-type	310 ± 50	0.46	0.09	3.61
447		B-type	430 ± 50	0.38	0.19	4.55
448	Large grain	A-type	300 ± 50	1.2	0.1	3.25
	Small grain	B-type		0.35	0.08	4.46

[1] Water content of olivine was measured from the inclusion-free area. Paterson calibration was used to calculate water content (Paterson, 1982).

[2] Average grain size was measured using the linear intercept method (Gifkins, 1970).

[3] Fabric strength of the LPO of olivine calculated using the M-index (Skemer et al., 2005).

[4] Fabric strength of the LPO of olivine calculated using the J-index (Bunge, 1982).

* Fabric strength of the LPO of tremolite

2.4.2. Chemical compositions of minerals

The representative chemical compositions of the minerals obtained via EPMA analysis are presented in Table 2.2. High content of magnesium was found in the olivine and orthopyroxene; with an Mg# of 94 for the olivine and 93–95 for the orthopyroxene. Orthopyroxene had very low aluminum concentration (Al_2O_3 = 0.10, 0.08 wt. %; Table 2.2), which is expected for the orthophyroxene in the amphibolite facies (Carswell, 1986). No significant chemical difference was found between the coarse porphyroclasts and fine recrystallized grains. Spinel had a high concentration of chromium (Cr_2O_3 = 58.98 wt. %; Table 2.2) and can be classified as chromite. Amphiboles can be classified as tremolite with a very low aluminum concentration (Al_2O_3 = 1.1 wt. %; Table 2.2).

Table 2.2. The chemical compositions of the representative minerals in the specimen.

Sample	**447**					**448**				
Mineral	**ol-1**	**ol-2**	**opx-1**	**amp-1**	**bt-1**	**ol-1**	**ol-2**	**opx-1**	**chl-1**	**sp-1**
SiO_2	41.10	41.61	57.85	56.33	42.68	41.49	41.60	58.22	31.33	0.00
TiO_2	0.03	0.01	0.00	0.01	0.06	0.01	0.01	0.00	0.02	0.01
Al_2O_3	0.01	0.00	0.10	1.10	12.18	0.00	0.00	0.08	13.36	3.03
Cr_2O_3	0.02	0.01	0.02	0.25	0.68	0.01	0.00	0.01	3.79	58.98
FeO	6.17	6.17	4.47	1.46	1.77	6.30	6.46	4.14	1.93	25.70
MnO	0.09	0.08	0.13	0.06	0.00	0.07	0.12	0.14	0.02	0.49
MgO	51.39	51.43	36.11	23.69	27.06	51.79	51.93	36.84	34.53	5.85
CaO	0.01	0.02	0.12	12.74	0.24	0.00	0.00	0.08	0.01	0.01
Na_2O	0.00	0.00	0.00	0.53	1.09	0.00	0.00	0.01	0.00	0.00
K2O	0.00	0.00	0.00	0.09	6.93	0.00	0.00	0.01	0.00	0.00
NiO	0.40	0.41	0.08	0.00	0.18	0.32	0.40	0.11	0.00	0.03
Total	99.21	99.75	98.88	96.26	92.86	99.99	100.52	99.62	84.97	94.10

wt% oxides, ol : olivine, opx : orthopyroxene, amp : amphibole, bt : bitotite, chl : chlorite, sp: spinel.

2.4.3. *LPO of minerals*

The LPOs of the olivine in the amphibole peridotite samples are illustrated in Fig. 2.3. In samples 443 and 448, it is apparent that the [100] axes of the olivine are aligned subparallel to the lineation and the [010] axes are aligned subnormal to the foliation, which is known as an A-type LPO (Jung and Karato, 2001a). In samples 446 and 447, the [001] axes of the olivine are aligned subparallel to the lineation and the [010] axes are aligned subnormal to the foliation, which is B-type LPO (Jung and Karato, 2001a; Jung et al., 2006). Some samples showed a combination of the two different types of LPOs. In sample 426, both the [100] and [001] axes of the olivine are aligned subparallel to the lineation and the [010] axes are aligned subnormal to the foliation; this is an A+B-type LPO (Chatzaras et al., 2016; Jung et al., 2014; Precigout and Hirth, 2014). In samples 429 and 445 the [001] axes of the olivine are aligned subparallel to the lineation and both the [100] and [010] axes are aligned subnormal to the foliation; this is known as a mixed B- and C-type LPO (B+C-type LPO). This B+C-type LPO of olivine is quite similar to the type III LPO of olivine which is reported by Prelicz 2005 (Prelicz, 2005). The fabric strength of the samples, which was calculated as both the M-index and J-index values from the LPO of the olivine and tremolite, is listed in Table 2.1. Both M- and J-index values tend to be slightly lower in samples with a mixed olivine LPO, such as A+B or B+C (samples 426, 429, and 445; Table 2.1). The fabric strength of the tremolite was much higher than that of the olivine (Table 2.1).

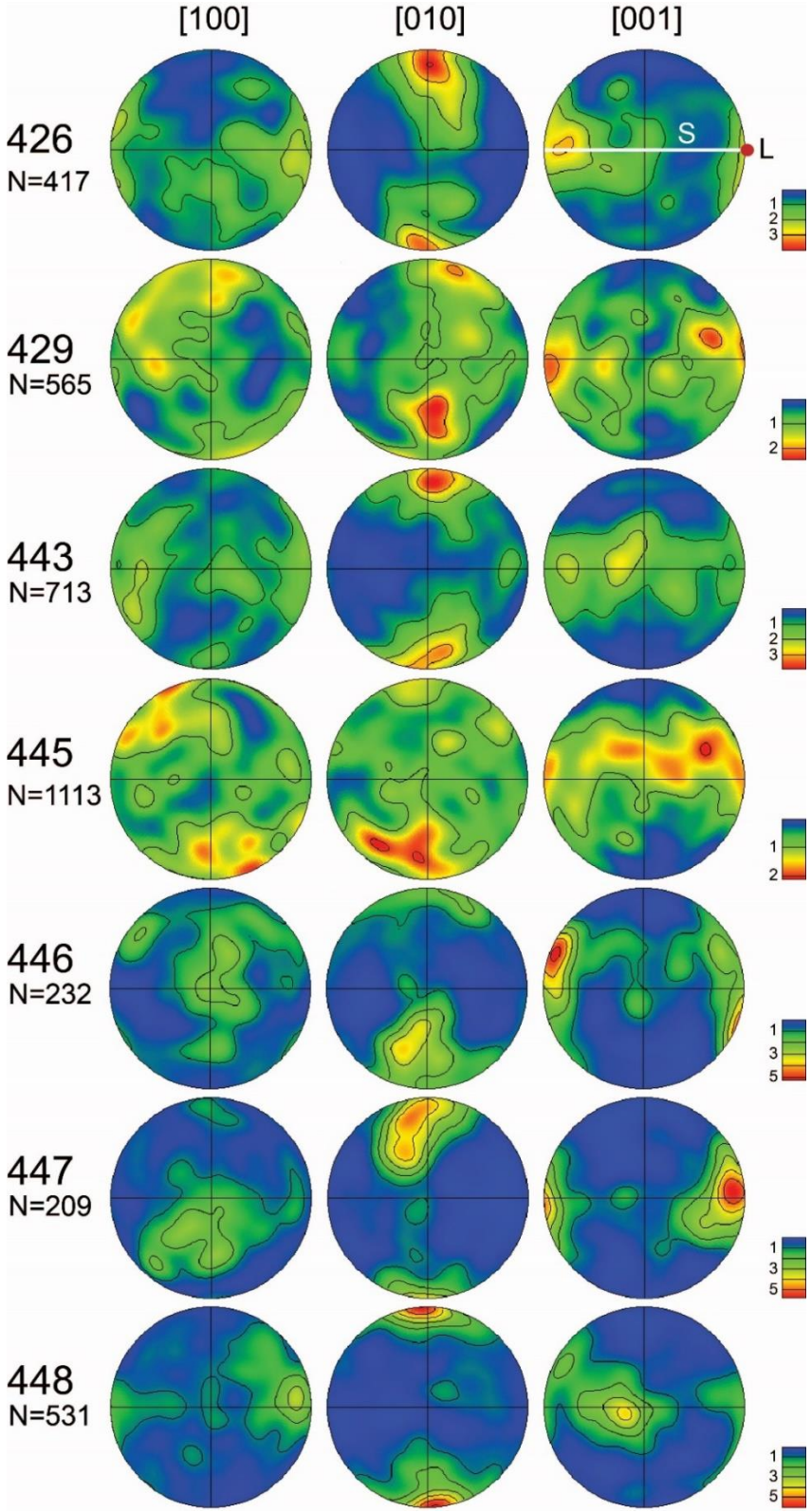

Figure 2.3. Pole figures of the olivine presented in the lower hemisphere using

equal-area projection. The white line (S) represents foliation and the red dot (L) represents lineation. A half-scatter width of 20° was used. “N” represents the number of grains. The color-coding indicates the density of the data points. The numbers in the legend correspond to multiples of uniform distribution.

To understand effects of grain size and mineral assemblage on the LPO of olivine, additional EBSD analysis was performed for three samples: sample 429, 443, and 448. Sample 429 was divided into the spinel-rich layer (Fig. 2.2B) and the spinel-poor layer. In case of sample 443, the LPOs of the olivine in the tremolite-rich and tremolite-poor layers were determined separately (Fig. 2.2D). Sample 448 was divided into the porphyroclasts and fine-grained recrystallized grains (Table 2.1). Detailed EBSD analysis of samples (429, 443, and 448) revealed that the LPO of olivine has a tendency to be varied within the mineral assemblage of the layer and the grain size of the samples (Fig. 2.4). In sample 429, the LPO of the olivine that was obtained from the spinel-rich layer (429 Sp-rich) was B+C-type, but the LPO of the olivine obtained from the spinel-poor layer (429 Sp-poor) was B-type (Fig. 2.4A). In sample 443, the LPO of the olivine obtained from the tremolite-rich layer (443 Tr-rich) was B-type, but the LPO of olivine obtained from the tremolite-poor layer (443 Tr-poor) was A-type (Fig. 2.4B). In sample 448, the LPO of the olivine observed from the coarse grains that included porphyroclasts (448 large grain) was A-type, but the LPO of the olivine in the recrystallized fine grains (448 small grain) was B-type (Fig. 2.4C).

The LPO of the tremolite in the tremolite-rich layer from sample 443 is also shown in Fig. 2.4B. The tremolite LPO exhibits the [001] axes and {010 poles forming a girdle distribution along the foliation with [100] axes that are aligned subnormal to the foliation; this is known as a type-III LPO of amphibole (Ko and Jung, 2015).

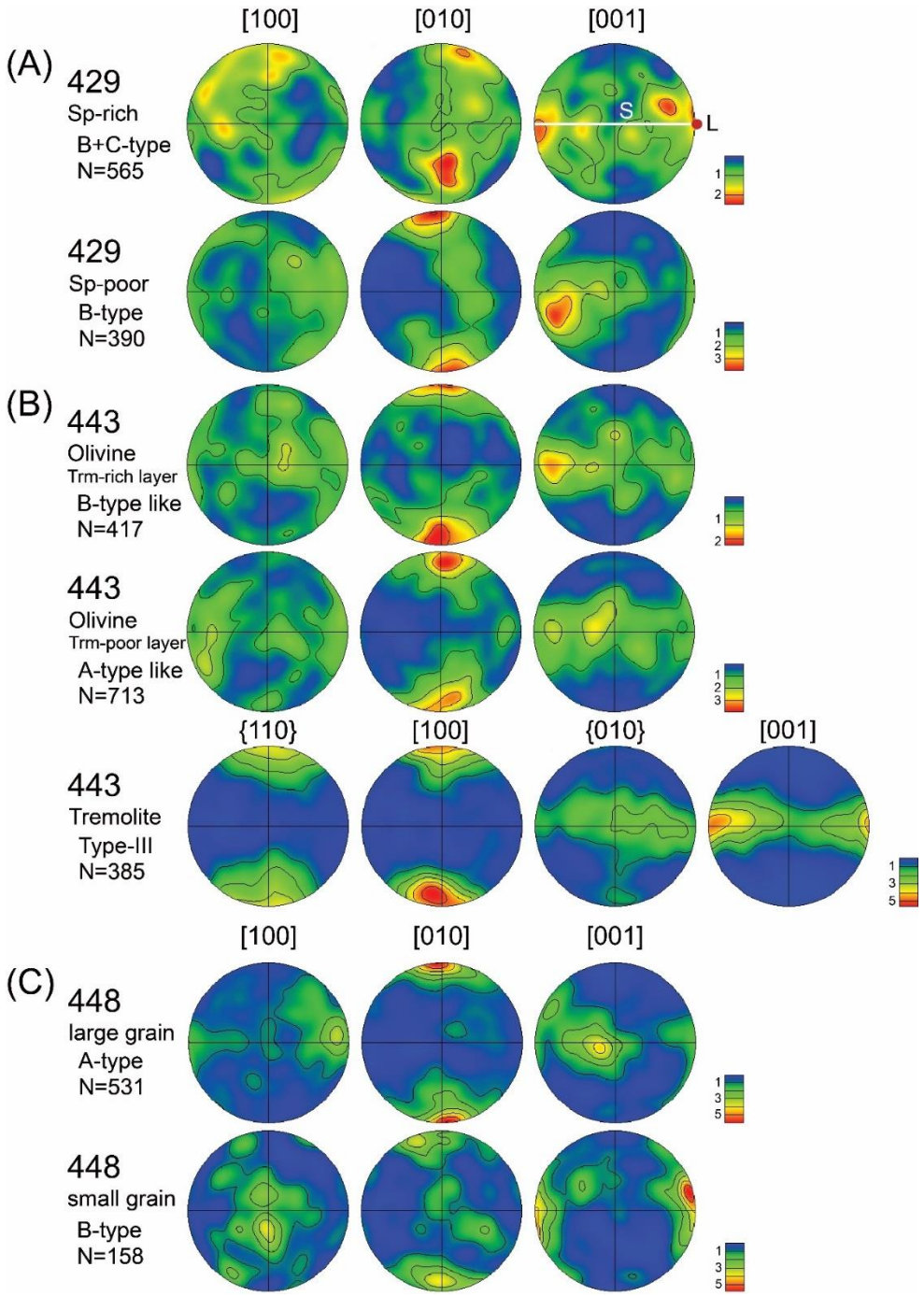

Figure 2.4. Pole figures of olivine presented in the lower hemisphere using an equal-area projection obtained from (A) the spinel-rich layer and a spinel-poor layer of sample 429, (B) the tremolite-poor layer and tremolite-rich layer of sample 443, and (C) large grains including the porphyroclasts and recrystallized small grains of

sample 448. The pole figure of the tremolite from the tremolite-rich layer of sample 443 is also included in (B). The white line (S) represents foliation and the red dot (L) represents lineation. A half-scatter width of 20° was used. “N” represents the number of grains. The color-coding indicates the density of data points. The numbers in the legend correspond to multiples of uniform distribution.

2.4.4. Seismic velocity and anisotropy

To simulate the changes in the seismic properties from the degree of the recrystallization, the LPO data from large porphyroclasts and fine-grained recrystallized grains were mixed with 6 different mixing ratios; 100:0, 80:20, 40:60, 60:40, 20:80, and 0:100. The LPO of the olivine in sample 448 was chosen as the original raw data because of its clear porphyroclastic texture (Fig. 2.2A). Because sample 448 mainly consisted of olivine (more than 90%), only the LPO of olivine was considered for the calculation. The seismic velocity and anisotropy of sample 448 are illustrated in Fig. 2.5. In the large grains of sample 448 (100 %), the P-wave anisotropy (AV_P) was found to be 5.7 %, maximum S-wave anisotropy (AV_S) was 3.63 %. Calculated AV_P and maximum AV_S values were similar to or slightly higher than those from the previous studies on the Almklovdalen chlorite peridotites; 2.4-8.2 % and 0.9-4.3 % from Prelicz (2005), 5.3-6.0 % and 3.72-4.46 % from Wang et al. (2013), and 1.8-3.8 % and 1.66-2.68 % from Kim and Jung (2015). For large grains of sample 448, the polarization direction of the fast shear wave at the center of stereonet was subparallel to the direction of flow (X-direction; Fig. 2.5). With the increasing ratio of small grains, the polarization direction of the fast shear wave started tilting and became subnormal to the flow direction at the large grains (40 %) and small grains (60 %) (Fig. 2.5). This result indicates that with the 60 % of recrystallization rate, a trench-parallel shear wave anisotropy is expected at the mantle wedge, assuming a 2D corner flow of the upper mantle. The estimated thickness of the anisotropic layer for the given delay time is noted in Table 2.3.

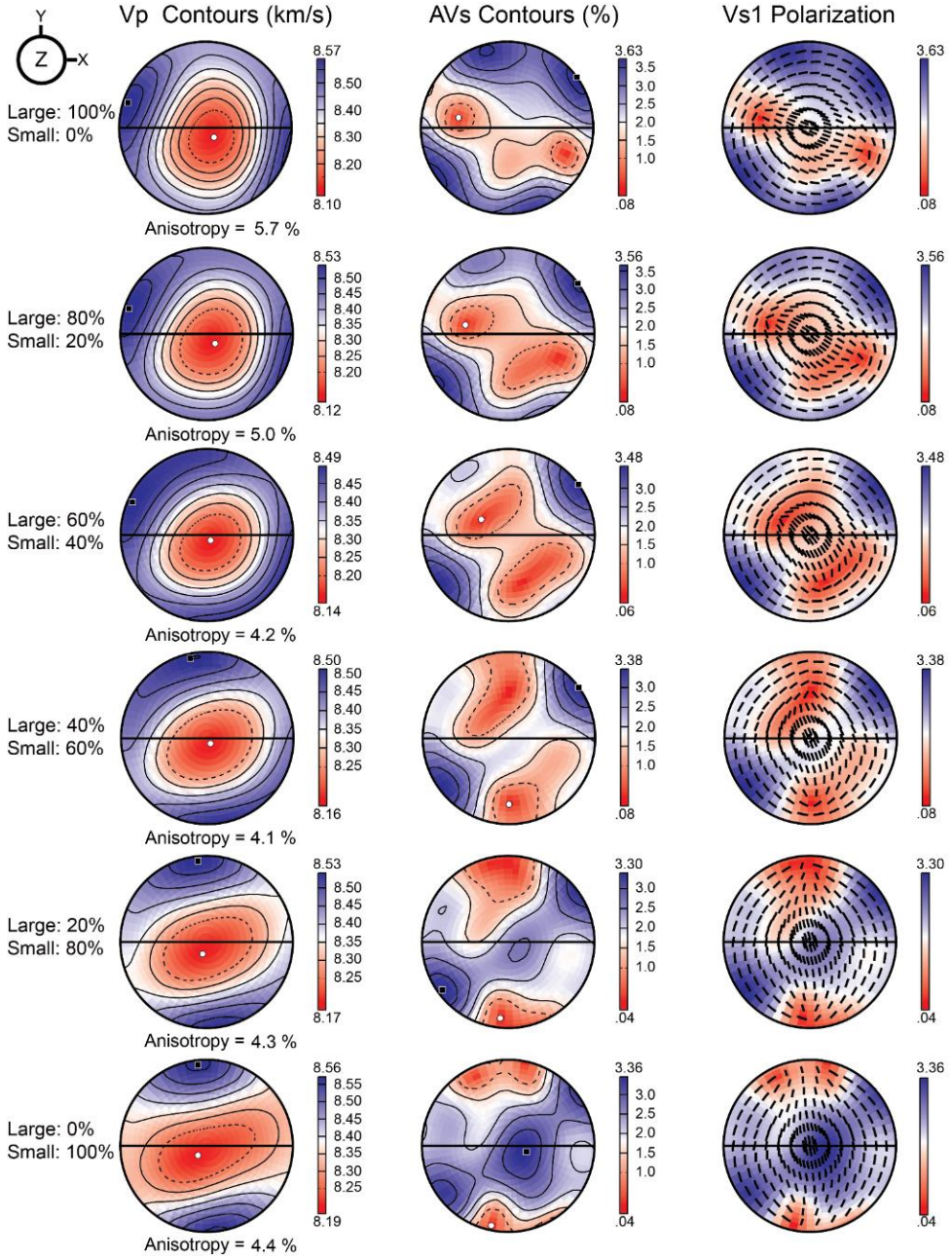

Figure 2.5. Effects of multiple stages of deformation on seismic velocity and anisotropy. LPO data of olivine from 448 large grains and 448 small grains (Fig. 2.4C) was mixed with 6 different mixing ratios; 100:0, 80:20, 40:60, 60:40, 20:80, and 0:100. Seismic velocity and anisotropy are calculated from the mixed LPO data to estimate the effect that the secondary deformation event had on the seismic

anisotropy. The P-wave velocity (V_P), the amplitude of the shear-wave anisotropy (AV_S), and the polarization direction of the faster shear wave (Vs1) are plotted in the lower hemisphere using an equal-area projection. The center of the stereonet corresponds to the direction normal to the foliation (Z), and the east-west direction corresponds to lineation (X).

Table 2.3. Estimated seismic anisotropy and the thickness of the anisotropic layer for the given delay time calculated from the LPOs of the olivine, amphibole, and serpentine.

The mixing ratio of 448 large grain and 448 small grain	**Horizontal AV_S (%)**[1]	**$<V_S>$ (km/s)**[1]	**The thickness of the anisotropic layer for the given delay time calculated from the seismic anisotropy (km)**		
			dt = 0.1 s	**dt = 0.2 s**	**dt = 0.3 s**
100:0	1.8	4.780	27	53	80
80:20	1.4	4.785	34	68	103
60:40	1.5	4.790	32	64	96
40:60	1.8	4.790	27	53	80
20:80	2.4	4.795	20	40	60
0:100	3.1	4.800	15	31	46
Mineral assemblage					
Olivine (443)[2]	1.4	4.813	34	69	103
Olivine + tremolite[2] (70%) (30%)	1.7	4.665	27	55	82
Olivine + tremolite[2] (50%) (50%)	2.5	4.595	18	37	55
Tremolite (443)[2]	5.5	4.340	8	16	24
Antigorite (VM3)[3]	1.6	3.735	23	47	70
Tremolite (443)[3]	6.0	3.975	7	13	20
Ol + Atg + Trm[3] (50%) (25%) (25%)	3.2	4.450	14	28	42

[1] Horizontal AV_S and $<V_S>$ were determined at the center of the stereonet (vertical S-wave propagation direction; Figs. 5, 6)

[2] The LPO data was rotated with a dipping angle of 45° to simulate the effect of flow dipping along the subducting slab.

[3] The LPO data was rotated with a dipping angle of 55° to simulate the effect of flow dipping along the subducting slab. The LPO data of the antigorite is from Jung (2011).

AVs: anisotropy of S-wave velocity, $<V_S>$: the average velocity of the fast and slow shear waves (V_{S1} and V_{S2}), dt: delay time of S-wave, Ol; olivine, Atg: antigorite, Trm: tremolite.

The LPOs of the olivine and tremolite in the tremolite-rich layer of sample 443 (Fig. 2.2D) were chosen to estimate the influence that the amphibole had on the seismic anisotropy of the mantle wedge. The LPO data of olivine and tremolite in the tremolite-rich layer were mixed in 70:30 and 50:50 ratio and was rotated with a dipping angle of 45° to simulate the effect of flow dipping along the subducting slab in the mantle wedge. The seismic velocity and anisotropy of the tremolite-rich layer of sample 443 are shown in Fig. 2.6. In the case of the olivine (443 Ol), AV_P is 3.8 %, maximum AV_S is 2.68 % and the polarization direction of the fast shear wave at the center is oblique to the flow direction (Fig. 2.6A). The tremolite of this sample (443 Trm) demonstrates AV_P of 21.8 %, maximum AV_S of 14.19 %, and the polarization direction of the fast shear wave at the center is aligned subnormal to the flow direction (Fig. 2.6A). When the olivine and tremolite are mixed with 70:30 ratio, the AV_P is 8.4 %, maximum AV_S is 5.79 %, and the polarization direction of the fast shear wave at the center is aligned subnormal to the flow direction (Fig. 2.6A). With 50:50 mixing ratio, the AV_P is 12.0 %, maximum AV_S is 8.07 %, and the polarization direction of the fast shear wave at the center is aligned subnormal to the flow direction (Fig. 2.6A). This result suggests that the presence of amphibole may significantly contribute to the trench-parallel S-wave anisotropy, assuming that the flow dips along the subducting slab in the mantle wedge. In addition, the P- to S-wave velocity ratio (V_P/V_S) of the tremolite was smaller than that of the olivine (Fig. 2.6A). The maximum V_P/V_S for the olivine, amphibole, and olivine + amphibole mixture (50:50) was 1.74, 1.70, and 1.71, respectively.

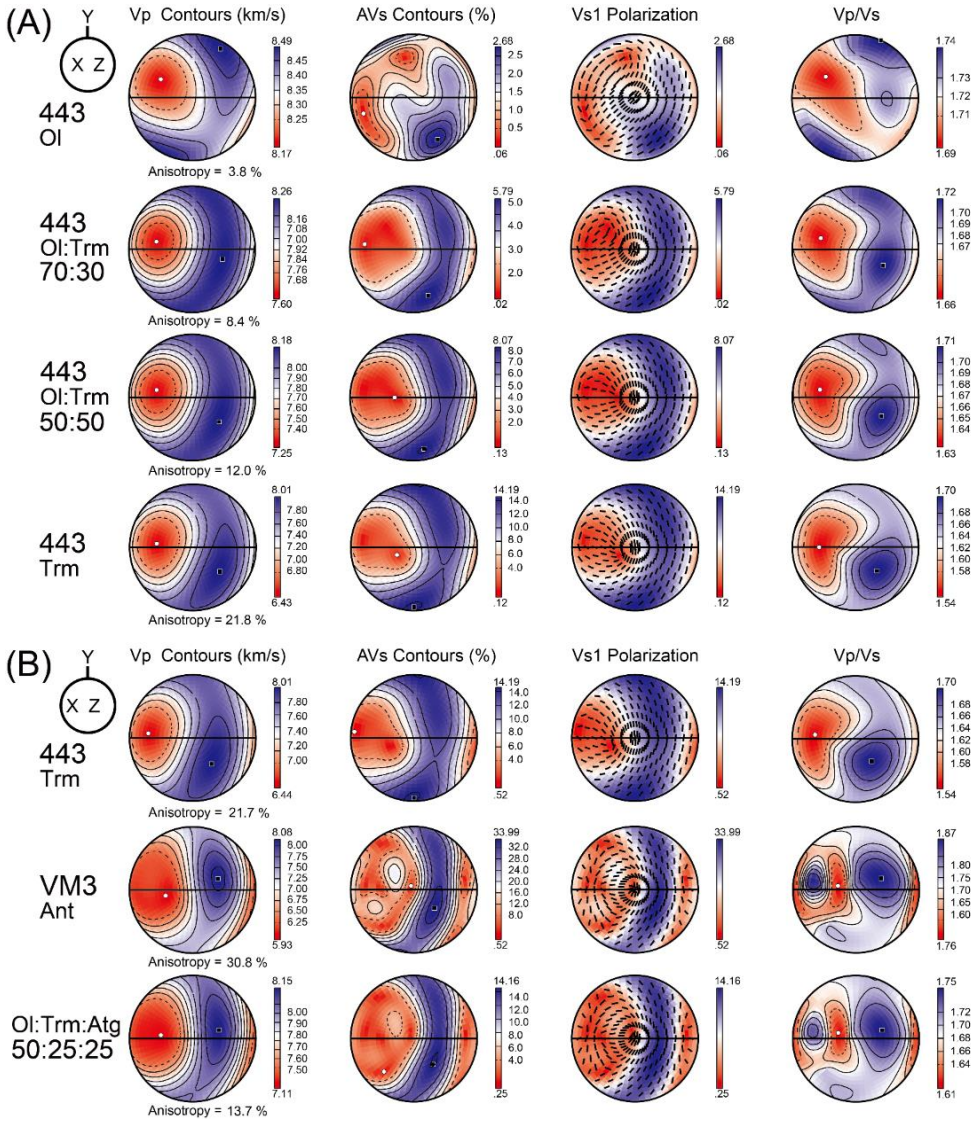

Figure 2.6. (A) Effect of amphibole on seismic velocity and anisotropy. LPO data of the olivine and tremolite in the tremolite-rich layer in sample 443 (Fig. 2.4B) was used. (B) Effect of amphibole and serpentine on seismic velocity and anisotropy. LPO data of the olivine and tremolite in the tremolite-rich layer in sample 443 (Fig. 2.4B) and LPO data of antigorite (VM3) reported by Jung [36] was used. The P-wave velocity (V_P), the amplitude of the shear-wave anisotropy (AV_S), the polarization direction of the faster shear wave (V_{S1}), and the P- to S-wave velocity ratio (V_P/V_S) are plotted in the lower hemisphere using an equal-area projection. The

x direction and the z direction correspond to the lineation and the direction normal to the foliation, respectively. Ol: olivine, Trm: tremolite, Atg: antigorite.

In addition, the LPO data of the serpentine was mixed with the LPO of the olivine and tremolite in the tremolite-rich layer of sample 443 in order to compare the influence of amphibole and serpentine on the seismic anisotropy in subduction zones. The LPO data of the antigorite from Val Malenco, Italy (sample VM3) reported by Jung (Jung, 2011) was mixed with the LPO data of the olivine and tremolite in the tremolite-rich layer of sample 443 in a 50:25:25 (olivine : tremolite : antigorite) ratio. Because serpentine requires a high dipping angle to produce trench-parallel seismic anisotropy [36], calculated data was rotated with a dipping angle of 55° in order to make a proper comparison. Calculated seismic velocity and anisotropy of the olivine, tremolite, and antigorite mixture are shown in Fig. 2.6B. The mixing ratio of olivine, tremolite, and antigorite was 50:25:25. The AV_P is 13.7 %, maximum AV_S is 14.16 %, and the polarization direction of the fast shear wave at the center is aligned subnormal to the flow direction (Fig. 2.6B). In addition, the pattern of the seismic velocity and anisotropy was similar to that of the antigorite (VM3; (Jung, 2011)), which indicates that the seismic anisotropy of the overall mixture is governed by the antigorite.

2.4.5. Water content of olivine

The representative FTIR spectra of olivines are illustrated in Fig. 2.7. In the case of the olivine grain without any inclusions or cracks, small absorption peaks were observed (Fig. 2.7A). The average water content of olivine calculated using the IR bands between 3,400 and 3,750 cm^{-1} was 370 ± 50 ppm H/Si (Table 2.1), which is above the boundary between the A-type and B-type LPO illustrated by the fabric

diagram for olivine (Jung et al., 2006). The average water content of olivine from this study was higher than that from previous studies on the Almklovdalen chlorite peridotites; 7-115 ppm H/Si from Wang et al., 2013 (Wang et al., 2013) and 170-310 ppm H/Si from Kim & Jung 2015 (Kim and Jung, 2015). No significant difference was apparent in the FTIR spectrum related to the grain size of the olivine or the mineral assemblage of the sample, and therefore all the FTIR spectra were averaged. Additional FTIR analyses were performed for the olivine grains with visible inclusions to study the components of these samples. The resulting FTIR spectra showed strong absorption bands in the range 3,400 to 3,750 cm^{-1} (Fig. 2.7B, C). IR peaks were found at the wave numbers of 3689, 3684, 3649, and 3630 cm^{-1}, which indicates the presence of serpentine as a hydrous inclusion in the olivine (Jung, 2009; Khisina et al., 2001; Miller et al., 1987).

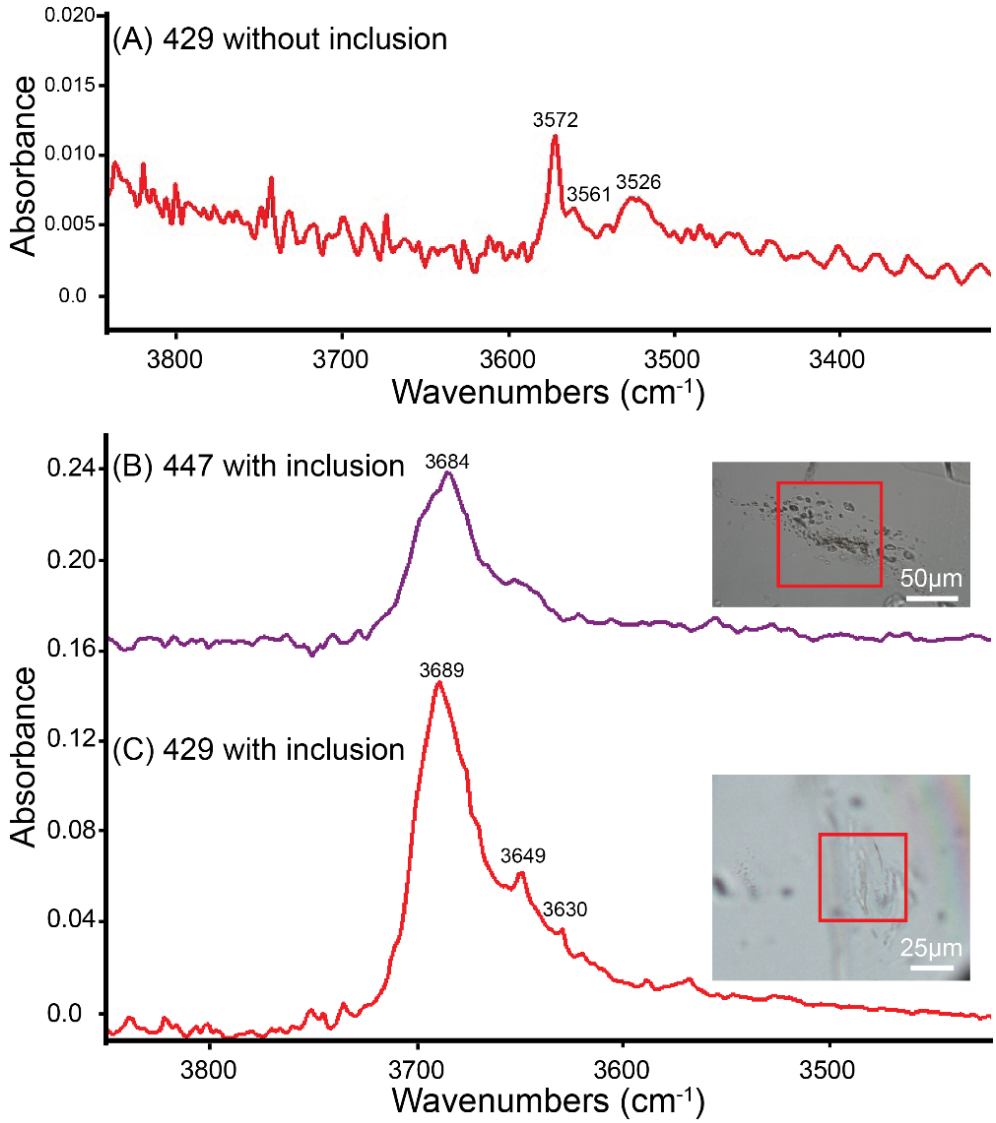

Figure 2.7. A representative unpolarized FTIR spectra of the olivine. (A) FTIR spectrum of olivine in sample 429 without any inclusions or grain boundaries. (B) FTIR spectrum of olivine in sample 447 where hydrous inclusions are found, and the optical micrograph image of the location from which the FTIR spectra are taken. (C) FTIR spectrum of olivine in sample 429 where a hydrous inclusion is found, and optical micrograph image of the location from which the FTIR spectra are taken.

2.4.6. Dislocation microstructure of olivine

Backscattered electron images of the dislocation microstructure of the olivine are shown in Fig. 2.8. All samples showed a homogeneous distribution of the dislocations, and there was no significant difference between the samples with different LPOs of olivine. In many cases, the dislocations were observed to be curved (Fig. 2.8A) or looped (Fig. 2.8C), suggesting the strong influence that obstacles have on the dislocation glide. Abundant subgrain boundaries were observed in the olivine grains (Fig. 2.8A, B, and C), which were similar to those observed with the optical microscope (Fig. 2.2A, C).

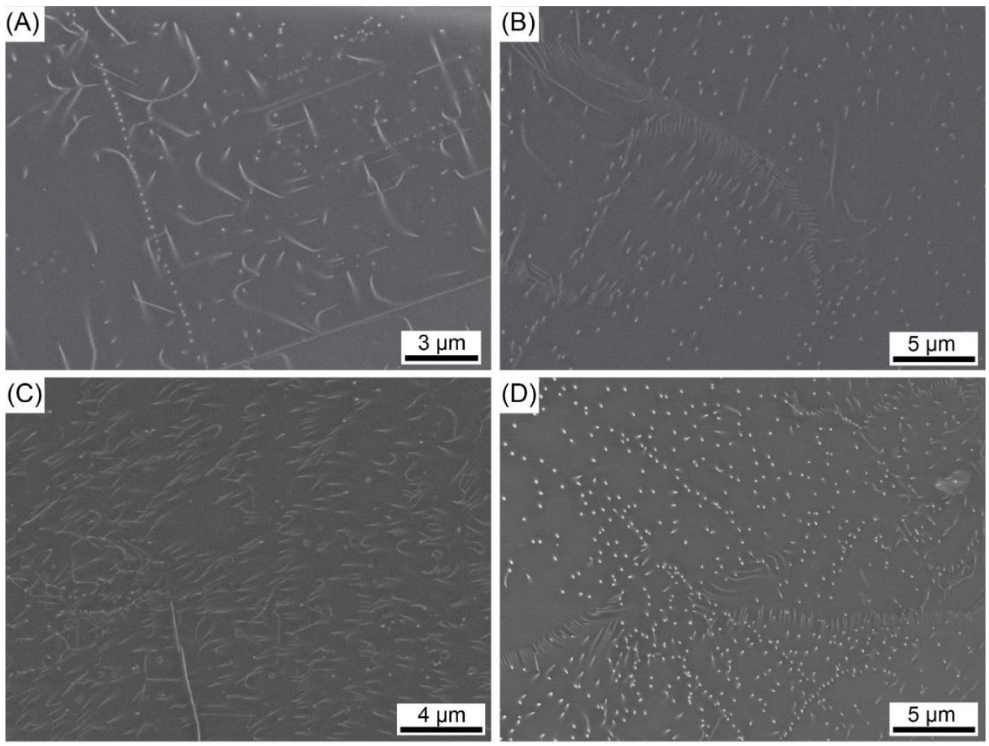

Figure 2.8. Backscattered electron images showing dislocation microstructures of olivine from (A) sample 426, (B) sample 429, (C) sample 447, and (D) sample 448. Dislocations are shown as white dots and lines.

2.5. Discussion

2.5.1. Development of LPO of olivine

Previous studies on the Almklovdalen chlorite peridotites located at a distance of 3 km from the Åheim peridotites, reported both A- and B-type LPOs of olivine (Wang et al., 2013), A-, B-, C-, and E-type LPO of olivine (Kim and Jung, 2015), and A-, B+C-type, and axial [010] pattern LPOs of olivine (Prelicz, 2005). Wang et al. (2013) interpreted that the A-type and B-type LPOs of olivine were formed under dry conditions (7–115 ppm H/Si) and the B-type LPO of olivine was developed under conditions of high stress and high strain. On the other hand, Kim and Jung (2015) reported that the A-type LPO was a result of deformation under dry conditions (170 ± 30 ppm H/Si), whereas the B-type LPO was developed due to the deformation of olivine under wet conditions (210–310 ± 30 ppm H/Si). Prelicz (2005) reported that B+C-type (type III) LPO of olivine developed in a mantle peridotite under water-rich retrograde conditions possible during the emplacement in crustal rock.

In this study, we observed that the LPO of the olivine in the Åheim amphibole peridotites has a close relationship with the grain size of olivine and the mineral assemblage of peridotite (Table 2.1, Fig. 2.4). The A-type LPO of olivine was observed in the coarse grains of sample 448 (with an average grain size of 1.2 mm, Table 2.1, Fig. 2.2A) and the tremolite-poor layer of sample 443 (with an average grain size of 0.7 mm, Table 2.1, Fig. 2.2D). On the other hand, B-type LPO was observed from the recrystallized fine grains of olivine in sample 448 (with an average

grain size of 0.35 mm, Table 2.1, Fig. 2.2A) and in the tremolite-rich layer of sample 443 (with an average grain size of 0.35 mm, Table 2.1, Fig. 2.2D). One possible mechanism for this fabric transition from A-type to B-type LPO observed in the olivine from the Åheim amphibole peridotites is olivine deformation under water-rich conditions. The water content of the olivine measured via the FTIR spectroscopy was in the range of 230–500 ± 50 ppm H/Si, which indicates that the olivine was deformed under water-rich condition (Jung and Karato, 2001a; Jung et al., 2006). The presence of hydrous minerals such as amphibole and chlorite (Fig. 2.2D), and the abundant hydrous inclusions observed in the olivine (Fig. 2.7B, C) suggest that the deformation of the recrystallized olivine grains occurred in the presence of a fluid. In addition, numerous dislocations were observed in the olivine samples (Fig. 2.8). These results indicate that the dominant deformation mechanism of olivine showing B-type LPO in the Åheim peridotites is dislocation creep under water-rich conditions.

The other possible mechanism for a fabric change from A-type to B-type LPO of olivine is an enhancement of dislocation-accommodated grain boundary sliding (DisGBS) (Cao et al., 2017; Hansen et al., 2011; Hirth and Kohlstedt, 2003; Precigout and Hirth, 2014). Precigout and Hirth (Precigout and Hirth, 2014) proposed that a fabric transition from an A-type to B-type LPO in olivine that was observed in the Ronda massif, Spain, could have resulted from the enhancement of GBS as the grain size decreased. The average grain size of the olivine in the Ronda peridotite was ~1 mm in the tectonites and 0.05–0.3 mm in the upper mylonite (Precigout and Hirth, 2014), which is similar to that of the Åheim amphibole peridotite (448 fine: 0.35 mm, and 448 coarse: 1.2 mm; Table 2.1). In addition, the few four-grain junctions (Fig. 2.2E, F) observed from the recrystallization of olivine

grains with B-type olivine fabric (Fig. 2.3) could be further evidence for a minor contribution from deformation via GBS (Ashby and Verral, 1973; Goldsby and Kohlstedt, 2001).

B+C-type LPO of olivine was observed in the olivine of sample 445 and the spinel-rich layer of sample 429. C-type LPO of olivine is known to be produced under conditions of low stress and water-rich conditions (Jung and Karato, 2001a; Jung et al., 2006; Katayama and Karato, 2006). Water may have been lost from the olivine during exhumation. A high water content (up to 500 ± 50 ppm H/Si; Table 2.1) and the presence of hydrous inclusions such as serpentine in the olivine (Fig. 2.7C) indicate that the B+C-type LPO of olivine observed in samples 429 and 445 can be related to deformation under water-rich conditions. In addition, numerous dislocations were observed in the olivine samples (Fig. 2.8B). These results indicate that the dominant deformation mechanism of olivine demonstrating the C-type LPO in the Åheim peridotites is dislocation creep under water-rich conditions. C-type LPO of olivine was also reported in the other previous studies where peridotites were deformed in water-rich conditions at various localities such as Cima di Gagnone in the Central Alps (Frese et al., 2003), Otrøy Island, in Western Norway (Katayama et al., 2005), the North Quidam UHP belt, NW China (Jung et al., 2013), and the Rio Grande rift, U.S.A. (Park et al., 2014).

2.5.2. The deformation history of Åheim peridotite

The LPO of the olivine in the Åheim amphibole peridotites showed four

different types of olivine fabric: A-, B-, A+B-, and B+C-type LPO of olivine (Fig. 2.3, 4). The Åheim peridotite bodies represent the lithospheric mantle where it was entrapped in the crust during the uplift process (Brueckner et al., 2010; Carswell, 1986). A-type LPO of olivine was observed in the coarse olivine grains including the porphyroclasts (Fig. 2.4B, 4C, Table 2.1), which can therefore be interpreted as the original mantle fabric prior to uplift. Deformation was localized in the fine recrystallized-grain area of the samples (Fig. 2.2B, 2C, 2D). Considering that a significant amount of strain is required to alter the LPO of olivine (Boneh et al., 2015; Boneh and Skemer, 2014), the strain of the deformation during the exhumation process is considered insufficient to change the pre-existing LPO of olivine porphyroclasts. During the uplift process, fluid infiltrated the samples in the amphibole peridotite stability field (Brueckner et al., 2010; Kostenko et al., 2002) enhancing the recrystallization of the olivine under water-rich conditions (Jung and Karato, 2001b), which is considered to have resulted in the fabric transition of olivine from A-type to C- and B-type.

The secondary olivine fabric which was developed in the Åheim peridotites is considered to be the C-type LPO of olivine, which is preserved as the B+C-type LPO of olivine in sample 445 and the spinel-rich layer of sample 429 (Fig. 2.4A). The C-type fabric in the Åheim amphibole peridotite can be correlated with the spinel bearing assemblage (Fig. 2.2B, 4A), which is related to the granulite facies (ol + opx + cpx + sp) condition and following high amphibolite facies (ol + opx + amp + sp) condition during the process of exhumation (Brueckner et al., 2010; Carswell, 1986; Lapen et al., 2009). After the granulite facies condition, a localized deformation associated with the fluid infiltration may have resulted in the fabric transition to the

C-type LPO of olivine (Fig. 2.7C). Because granulite facies metamorphism was recorded in the Åheim amphibole peridotite prior to amphibolite facies (Brueckner et al., 2010; Carswell, 1986; Lapen et al., 2009), this C-type LPO can be regarded as secondary olivine fabric.

The last olivine fabric which was developed in the Åheim peridotites is considered to be as the B-type LPO of olivine observed in the small recrystallized olivine grains (Fig. 2.4B, 4C). Samples with B-type LPO of olivine were of the smallest grain size. B-type LPO of olivine can be related to the deformation of samples during low amphibolite facies (ol + opx + amp + chl) conditions, following the granulite facies (Brueckner et al., 2010; Carswell, 1986; Lapen et al., 2009). Fluid infiltration and the enhanced recrystallization of olivine at the amphibolite facies condition could lead to the fine-grained olivine grains that were deformed under water-rich conditions, resulting in the B-type LPO of olivine in the small recrystallized olivine grains. Both the A+B-type or B+C-type LPO of the olivine observed in samples 426, 429, and 445 (Fig. 2.3) can be interpreted as a B-type LPO of olivine overprinting a preexisting A- or C-type LPO of the olivine. These mixed LPOs of olivines are believed to be the last olivine fabrics preserved in the Åheim amphibole peridotites.

2.5.3. Implications for the seismic anisotropy in the SW Norway

The polarization directions of the fast shear wave are NW-SE on the Proterozoic outcrop regions including WGR with delay time of 1~3 s (Roy and Ritter, 2013).

Seismic anisotropy beneath the continental crust is proposed to be caused by LPO of anisotropic minerals in the lithosphere (Silver, 1996) and asthenosphere (Savage, 1999). The A-type LPO of olivine observed from the coarse olivine grains might be originated from the lithospheric mantle fabric. Apparent subduction direction of the Baltican crust beneath Laurentia was NW-SE direction in SW Norway (Andersen, 1998; Andersen et al., 1991; Torsvik and Cocks, 2005), so the lithospheric mantle fabric would be oriented in NW-SE direction. Because there have been no major orogenic event after the Scandian orogeny and subsequent post-collisional collapse (Andersen, 1998; Austrheim et al., 2003; Torsvik and Cocks, 2005), the lithosphere beneath WGR might preserve lithospheric mantle fabric frozen after the Scandian Orogeny (Savage, 1999; Silver, 1996). The A-type LPO of olivine produces the fast shear wave polarization direction parallel to the flow direction with horizontal flow (Fig. 2.5). Thus, the NW-SE direction fast shear wave polarization observed from the Proterozoic outcrop regions can be influenced by the A-type LPO of olivine in the lithosphere beneath WGR frozen after the Scandian Orogeny.

However, calculated seismic anisotropy of the A-type LPO of olivine in the coarse olivine grains is insufficient for delay time > 1 s observed from the SW Norway. Depth of Moho and lithosphere-asthenosphere boundary in the SW Norway are 35–41 km and 100–130 km, respectively (Maupin et al., 2013). Assuming that there is 80 km thick lithosphere with the A-type LPO of olivine observed from the large grains of sample 448 (Fig. 2.4C), the delay time estimated 0.3 s (Table 2.3). In addition, there may be B-type LPO of olivine present in the lithosphere by the fabric transition of olivine related to the fluid (Fig. 2.4C; Jung and Karato, 2001a) or the pressure (Jung et al., 2009; Wang et al., 2013), which might weaken seismic

anisotropy of lithospheric mantle by negative interference between A- and B-type LPO of olivine (Table2.3; Fig. 2.5). Therefore, contribution of asthenosphere to the long delay time observed from the Proterozoic outcrop regions can be more important in the SW Norway (Savage, 1999). SW Norway has low seismic velocities in the upper mantle (Hejrani et al., 2017; Maupin et al., 2013; Wawerzinek et al., 2013), which can be interpreted as plume finger extended from the Iceland-Jan Mayen plume system (Koptev et al., 2017; Rickers et al., 2013). Fast shear wave polarization direction observed from the SW Norway might be resulted from the asthenospheric flow oriented in NW-SE direction beneath the SW Norway which is related to the Icelandic plume.

2.5.4. Implications for the seismic anisotropy in the mantle wedge

Trench-parallel seismic anisotropy has been observed at various subduction zones around the world (Long, 2013; Long and Silver, 2008; Mehl et al., 2003; Nakajima and Hasegawa, 2004; Savage, 1999; Smith et al., 2001). After experiments concerning the deformation of olivine under wet conditions at high pressures, a water-induced fabric change of the olivine in the subduction zone was suggested as one of the possible mechanisms for this phenomenon (Jung and Karato, 2001a; Jung et al., 2006). Because fabric transition from an A-type to B-type LPO of the olivine in the Åheim amphibole peridotite was driven by the fluid infiltration associated with the exhumation process during/after the Scandian orogeny, the olivine fabric data from this study cannot be directly applied to the current mantle wedge above the subducting slab. However, olivine fabric transition observed from the Åheim

amphibole peridotites could be a good example of water-induced fabric change to olivine in naturally deformed peridotites.

Prelicz (2005) reported the ultrasound velocities of P- and S-waves measured on cores obtained from Almklovdalen chlorite peridotites (Prelicz, 2005). The mean V_P and V_{S1} at confining pressure of 400 MPa were around 7.9-8.2 km/s and 4.76-5.1 km/s, respectively (Prelicz, 2005), The seismic velocities calculated from the LPO of olivine in sample 448 showed that V_P was slightly higher (8.1-8.57 km/s; Fig. 2.5) and $<V_S>$ was similar to the ultrasound velocity data (4.78-4.8 km/s; Table 2.3). There are several explanations for these differences in seismic velocities: 1) Since sample 448 mainly consisted of olivine, only the LPO of olivine was considered for the calculation. Therefore, the effect of secondary minerals was excluded in this case, especially for the effect of hydrous minerals such as tremolite and chlorite. 2) In this study, the elastic constant of single-crystal olivine at ambient condition was used for calculation. Because the elastic constant of olivine is dependent on the pressure and temperature (Abramson et al., 1997), there may be a minor error related to the elastic constant because of low pressure and temperature condition of rocks. 3) Because the calculated seismic anisotropy only considers the volume fraction, density, elastic constants, and the LPO of the mineral (Mainprice, 1990), the effects of thermal cracks or pore on the seismic velocities were neglected.

Because S-wave anisotropies in the A- and B-type LPO of olivine negatively interfere (Jung and Karato, 2001a; Jung et al., 2006), the mixing of these two olivine fabrics may result in a significant weakening of the seismic anisotropy (Cao et al., 2015) or change in S-wave anisotropy (Precigout and Almqvist, 2014). In the case

of sample 448, large grains (i.e., porphyroclasts) showed A-type LPO of olivine and small recrystallized grains (448 small grain) showed B-type LPO of olivine (Fig. 2.4C). The seismic velocity and anisotropy calculated from the LPOs of the olivine in sample 448 showed that with more than 60 % of fabric transition from A-type to B-type LPO of olivine, the polarization direction of the fast shear wave at the center of stereonet (vertical propagation of S-wave) changed, to become subnormal to the flow direction (trench-parallel; Fig. 2.5). Comparing the seismic anisotropy of the 60 % fabric transition (60:40) with that of the 100 % fabric transition to B-type LPO (0:100), S-wave anisotropy (AV_S) at the center of stereonet was decreased to ~42 % and the estimated thickness of the anisotropic layer for a given delay time was increased to ~80 % (Table 2.3). Assuming that the olivine fabric is partially changed from an A- to B-type LPO of olivine in the forearc mantle wedge (Fig. 2.9), the shear wave seismic anisotropy of the olivine in the forearc mantle wedge would be significantly decreased (Table 2.3). This mixed olivine fabric in the mantle wedge could be a possible explanation for the relatively small delay time (~ 0.2 s) observed at various subduction zones such as in NE Japan or Mexico (Cao et al., 2015; Huang et al., 2011; Long and Wirth, 2013; Soto et al., 2009).

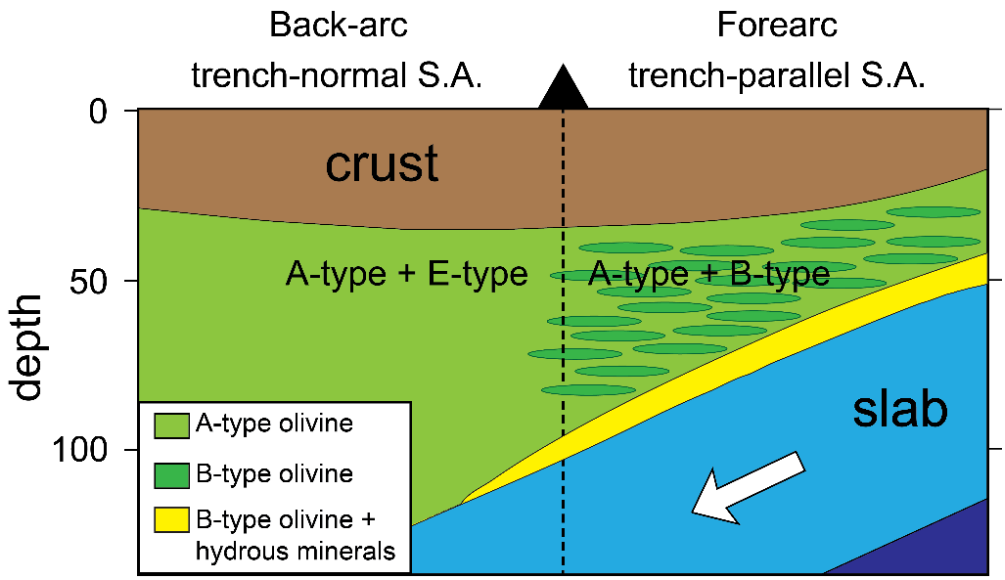

Figure 2.9. Schematic diagram of the proposed olivine fabrics in the mantle wedge of a cold subduction zone. Hydrous minerals: serpentine, chlorite, tremolite, etc. S.A.: seismic anisotropy.

To understand trench-parallel seismic anisotropy in subduction zones and assuming a mantle flow that is dipping alongside the slab, it is important to consider the effect that hydrous minerals are expected to have on the seismic anisotropy of a subduction zone (Jung, 2017; Mainprice and Ildefonse, 2009) such as the formation of serpentine (Jung, 2011; Katayama et al., 2009) and chlorite (Kim and Jung, 2015). Under a slab dipping angle of approximately 45°, the polarization direction of the fast shear wave was oblique to the lineation (flow) direction when only the LPO of olivine of sample 443 was considered (Fig. 2.6A). However, the polarization direction of the fast shear wave became subnormal to the flow direction when the tremolite LPO was mixed with the LPO of the olivine in sample 443 (Fig. 2.6A). Comparing the seismic anisotropy of the ol + trm mixture (50:50) with that of the olivine, AV_S was increased to ~79 % and the estimated thickness of the anisotropic layer for the given delay time was decreased to ~47 % (Table 2.3). This result suggested that the amphibole can have a similar effect on the trench-parallel shear wave splitting as other hydrous minerals such as serpentine and chlorite in the mantle wedge (Fig. 2.9).

Because of strong seismic anisotropy of antigorite, overall seismic velocity and anisotropy of the olivine, antigorite, and tremolite mixture were governed by the LPO of antigorite (Fig. 2.6B). Maximum AV_S of the antigorite was 2.4 times larger than that of the tremoloite, and the pattern of the seismic velocity and anisotropy of Ol+Atg+Trm mixture mostly followed that of the antigorite. However, AV_S values of the tremolite (Tremolite 443) for the vertically propagating seismic wave (at the center of the stereonet) was 3.75 times higher than that of antigorite (VM3) with a slab dipping angle of 55° (Table 2.3). In addition, amphibole can produce trench-

parallel seismic anisotropy (Fig. 2.6A) in a relatively lower slab dipping angle (45°) than that of the serpentine (Jung, 2011).

The maximum V_P/V_S values of the olivine, tremolite, and olivine + tremolite mixture are 1.74, 1.70, and 1.71, respectively (Fig. 2.6A). Calculated maximum V_P/V_S value of the tremolite (1.70) was close to the isotropic V_P/V_S value ($\beta_0 = 1.718$) in amphibolite reported by Ji et al. (Ji et al., 2013). The seismic velocity and anisotropy calculated from the LPOs of the olivine and tremolite in the tremolite-rich layer of sample 443 showed that the V_P/V_S ratio of the tremolite was smaller than that of the olivine (Fig. 2.6A). The V_P/V_S ratio of the mixed olivine + tremolite layer was also smaller than that of the olivine. High V_P/V_S zones have been observed at various subduction zones such as those near Cascadia, Nankai, and in central Mexico (Audet et al., 2009; Kim et al., 2010; Kodaira et al., 2004; Peacock et al., 2011; Shelly et al., 2006). These high V_P/V_S zones are usually interpreted as being the result of regionally high pore fluid pressure (Audet et al., 2009; Kodaira et al., 2004) or presence of talc (Kim et al., 2013b). Our result indicates that unlike talc or serpentine, amphibole does not influence much on the formation of the high V_P/V_S zones.

2.6. Summary

The microstructures of the amphibole peridotites from the Gusdal quarry in Åheim, Norway were studied and evidence for multiple stages of deformation during the Scandian Orogeny and subsequent exhumation was found. The Åheim amphibole peridotites showed a porphyroclastic texture with abundant undulose extinctions and

subgrain boundaries in the olivine. The LPOs of the olivine in the Åheim amphibole peridotites were closely related to the grain size of olivine and mineral assemblage of the samples. The coarse grains including porphyroclasts showed an A-type LPO of the olivine, which corresponds to the initial stage of deformation in the mantle. During the exhumation process, deformation was associated with the infiltration of fluid and enhanced dynamic recrystallization under water-rich conditions that resulted in the fabric transition of olivine from A-type to C- or B-type LPO. Olivines in the spinel-bearing assemblage showed a C-type LPO of olivine which can be interpreted as a result of deformation under water-rich condition after granulite facies metamorphism. The small recrystallized olivine grains showed a B-type LPO of olivine, which represents the deformation in amphibolite facies. A high water content (370 ± 50 ppm H/Si) and abundant dislocations in the olivine suggest that the B-type LPOs of olivine that were observed in the recrystallized olivine grains were developed via deformation by dislocation creep under water-rich conditions. In addition, the existence of small recrystallized grains and four-grain junctions indicate that the fabric transition from A-type to B-type was also influenced by the DisGBS process related to the grain size reduction. The microstructural evolution of the Åheim amphibole peridotites can be a good example of the fabric change of the olivine from A- to B-type that is observed in naturally deformed peridotite. Seismic anisotropy of the olivine in the Åheim amphibole peridotite calculated with a different ratio of coarse grains (showing an A-type LPO) and the fine recrystallized grains (showing a B-type LPO) of olivine indicates that with the 60 % recrystallization rate, a trench-parallel S-wave anisotropy is expected from the mantle wedge. Tremolites from the tremolite-rich layer showed Type-III LPO of amphibole. A stronger fabric strength was observed in the tremolite than that in the

olivine, and the resultant seismic anisotropy of the tremolite implies that amphibole can perform a similar role to other hydrous minerals such as serpentine and chlorite on the formation of trench-parallel seismic anisotropy.

CHAPTER 3

Deformation mechanism of olivine and amphibole in amphibole peridotite from the Åheim, Norway.

This chapter will be submitted for publication:

Jung, S., Yamamoto, T., Ando, J., and Jung, H., 2020. Deformation mechanism of olivine and amphibole in amphibole peridotite from the Åheim, Norway. in prep.

Abstract

The Western Gneiss Region had undergone UHP metamorphism and subsequent retrogression associated with the Scandian Orogeny. The microstructure of the amphibole peridotite samples from the Åheim, Norway was analyzed to understand the deformation mechanism of olivine and amphibole and the evolution of the microstructure through the Scandian Orogeny. The Åheim amphibole peridotite showed porphyroclastic texture and subgrain boundaries frequently occurred in the olivine. The electron back-scattered diffraction (EBSD) mapping and transmission electron microscope (TEM) observation revealed that most olivine subgrain boundaries consist of the dislocations with (001)[100] slip systems. These subgrain boundaries might be resulted from the deformation with moderate water content in olivine or low strain deformation. TEM observation with the thickness-fringe method found that the free dislocations with (010)[100] slip system of olivine were dominant for both samples. Our data suggest that the subgrain boundaries and free dislocations in the olivines represent the later stage deformation associated with the exhumation process. EBSD mapping on the tremolite-rich layer revealed intracrystalline plasticity in the amphibole which can be interpreted as activation of (100)[001] slip system in the tremolite.

3.1. Introduction

The relationship between lattice preferred orientation (LPO) of minerals and the active slip system of the dislocation is well understood by the theoretic and experimental studies (Karato, 2008; Mainprice and Nicolas, 1989). Deformation of the crystal associated with the dislocation creep is considered as an important mechanism of LPO, and generally, LPO is heavily influenced by the easiest slip system (Karato, 2008). Various theoretical models such as the Taylor-Bishop-Hill model (Lister et al., 1978; van Houtte and Wagner, 1985) and the self-consistent approach (Molinari et al., 1987; Winger et al., 1980) have been developed to calculate the formation of LPO by dislocation glide. The deformation mechanism and rheology of olivine has been the key to understand the kinematics and the seismic anisotropy of the upper mantle (Ben Ismail and Mainprice, 1998; Nicolas and Christensen, 1987). Previous experimental studies on the olivine aggregates reported that there can be various types of olivine LPO depending on the physico-chemical conditions during the deformation (Jung and Karato, 2001a; Jung et al., 2006; Katayama et al., 2004). For example, A-type LPO of olivine is characterized by the [100] axes aligned subparallel to lineation, and the [010] axes aligned normal to foliation. For the B-type LPO of olivine, the [001] axes are aligned subparallel to lineation and the [010] axes are aligned normal to the foliation. Various experimental studies reported that indeed there is close relationship between the LPO of olivine and the dominant dislocation slip system (Demouchy et al., 2014; Jung et al., 2006; Raterron et al., 2009). However, actual comparison between the LPO of minerals and the slip system of the dislocation for the naturally deformed peridotite specimen is still limited.

Various hydrous minerals such as serpentines, chlorites, and amphiboles in the subduction zone are elastically highly anisotropic and are very important for understanding seismic anisotropy at a subduction zone (Almqvist and Mainprice, 2017; Lee et al., 2020; Mainprice and Ildefonse, 2009; Mookherjee and Mainprice, 2014). Amphibole can be produced by the hydration reaction of pyroxene in the mantle wedge above the subducting slab (Cao et al., 2016; Evans, 1977). There have been many studies on the LPO and seismic anisotropy of amphibole from both experimentally deformed amphibole and natural amphibole samples (Ji et al., 2013; Kang and Jung, 2019; Kim and Jung, 2019; Ko and Jung, 2015; Tatham et al., 2008). Amphibole can be deformed by a variety of deformation mechanisms; rigid body rotation (Aspiroz et al., 2007; Getsinger et al., 2013; Tatham et al., 2008), cataclastic flow (Ko and Jung, 2015; Nyman et al., 1992), or diffusional creep (dissolution–precipitation creep) (Getsinger and Hirth, 2014; Imon et al., 2004) and dislocation creep (Cao et al., 2010; Rooney et al., 1975; Skrotzki, 1992). However, studies on the relationship between amphibole fabric and dislocation creep of the amphibole in the subduction zone are still very limited.

To understand the relationship between the slip system and the LPO of olivine and amphibole, detailed microstructural studies were performed on the amphibole peridotites from Åheim, Norway. Electron back-scattered diffraction (EBSD) mapping was performed to identify evidence of intracrystalline plasticity in the olivine and amphibole. The slip system of the olivine was determined by using a transmission electron microscope (TEM). These detailed microstructural analyses would lead to a better understanding of the deformation mechanism of the olivine

and amphibole and the evolution of microstructure in the Åheim amphibole peridotite during the orogenic event.

3.2. Geological setting and sample description

Amphibole peridotite samples were collected from the Gusdal quarry in Åheim, which is located in Western Gneiss Region (WGR) of the Norway (Fig 2.1; page 12). Among the samples which were analyzed in Chapter 2, three amphibole peridotite samples (443, 447, and 448) were selected for a more detailed microstructural study. Geological setting of the WGR were described in Chapter 2.2 in pages 12-14.

All samples have a porphyroclastic texture and dominantly consist of olivine (>90%) with a minor amount of chlorite, orthopyroxene, amphibole (tremolite), biotite, and spinel (Fig. 3.1A, B, C, D). However, sample 443 showed a locally tremolite-rich layer with an approximately 50 % modal composition of tremolite (Fig.3.1E, F). Abundant cracks and microfractures are observed from the tremolite (Fig.3.1F). The foliation of samples was well defined by the compositional layering of olivine, amphibole, and chlorite. Elongated olivine grains are also well aligned along the foliation plane (Fig. 3.1A, B). The sample 447 was relatively more recrystallized than the sample 448 (Fig. 3.1A), with the average grain size of 0.5 mm for the sample 447 (Jung et al., 2020). The sample 448 showed clear porphyroclastic texture (Fig. 3.1B); the average grains size was 0.35 mm for the fine grains in sample 448 and 1.2 mm for the coarse grains in sample 448 (Jung et al., 2020). Olivine porphyroclasts have curvy grain boundaries, showing the evidence of

recrystallization by the grain boundary migration. On the other hand, straight grain boundaries and triple junction are often observed for the smaller recrystallized grains, which indicate the annealing process takes place during exhumation (Fig. 3.1). Undulose extinction and subgrain boundaries were very common in all samples (Fig. 3.1C, D).

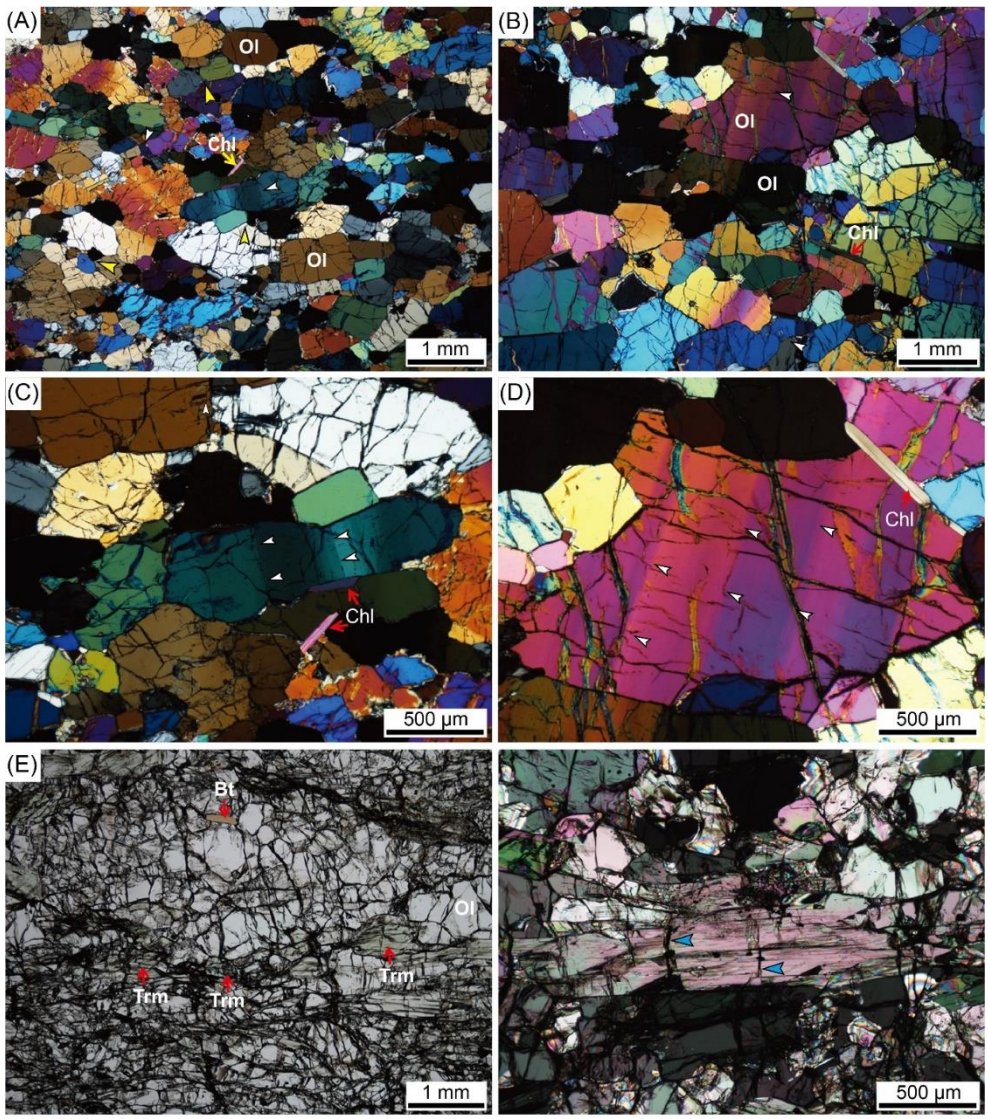

Figure 3.1. Optical photomicrographs of the samples in transmitted light. (A, B) Representative wide-view images of sample 447 (A) and the sample 448 (B). Olivine grains are well elongated along the foliation plane. White arrows mark the olivine crystals showing clear subgrain boundaries. Olivine and chlorite grain is indicated as Ol and Chl, respectively. (C, D) Enlarged image of the olivine crystals showing clear subgrain boundaries for the sample 447 (C) and sample 448 (D). White arrows indicate the subgrain boundaries and the chlorites are also noted as Chl. (E) Tremolite-rich layer observed from sample 443. Tremolite and biotite grains are

indicated as Trm and Bt, respectively. (F) Tremolite from sample 443. Blue arrows mark the fractures in the tremolite.

The previous study on the microstructure of the Åheim amphibole peridotite samples presented evidence for multiple stages of deformation during the Scandian Orogeny and subsequent exhumation (Jung et al., 2020). The coarse grains including porphyroclasts in sample 448 showed the A-type olivine LPO, which corresponds to the initial stage of deformation. On the other hand, recrystallized olivine grains in the sample 447 and 448 showed the B-type of olivine LPO and it represents the later stage deformation associated with the exhumation process. Observation of abundant hydrous minerals and hydrous inclusions in olivine, as well as the high water content of olivine, suggest that fabric transition of olivine from the A-type to B-type LPO was resulted from the deformation in a water-rich condition during the exhumation process (Jung et al., 2020).

3.3. Experimental method

3.3.1. EBSD data acquisition and processing

Thin sections for the EBSD analysis were prepared in the x-z plane of the Åheim amphibole peridotite sample (x: lineation, z: normal to foliation). Lineation was determined by examining the shape-preferred orientation of elongated olivines in the foliation plane using the projection-function method (Panozzo, 1984). EBSD data were collected using a scanning electron microscope (SEM) equipped with an EBSD detector (JEOL JSM-6380 and JSM-7100F) housed at the School of Earth and Environmental Sciences (SEES) in the Seoul National University (SNU). Collected

EBSD data were processed by using HKL Channel 5 software and AZtec software.

For the olivine grains with the subgrain boundaries, EBSD mappings along the olivine subgrain boundaries were performed to determine the dominant slip system of dislocations in subgrain walls with the rotation axes of olivine across the subgrain boundaries (Lloyd et al., 1997; Prior et al., 1999; Wheeler et al., 2001). By comparing the rotation axes and the subgrain boundary from each olivine single grain, slip direction and slip system of the subgrain boundary can be specified. This method has been applied to define activated slip system of porphyroclastic natural peridotite samples from various localities (Cao et al., 2014; Kaczmarek and Reddy, 2013; Katayama et al., 2011; Kumamoto et al., 2019; Palasse et al., 2012; Precigout and Hirth, 2014; Yamamoto et al., 2017). EBSD mappings were performed by JEOL JSM-6380 SEM with a tilt angle of 70° and an acceleration voltage of 20 kV. A total of 20 olivine grains showing well-defined subgrain boundaries were analyzed for each sample to gather the rotation axes with a misorientation angle around 2-10°. The step size for the EBSD mapping was in the range of 3-8 μm depending on the size of the analyzed grain.

In addition, a crystallographic orientation map was constructed for the tremolite-rich layer from sample 443 (Fig 3.1E, F; Jung et al. (2020)) to analyze the microstructure of amphibole. EBSD data were collected by JEOL JSM-7100F SEM with a tilt angle of 70°, an acceleration voltage of 15 kV, and a step size of 25 μm. Collected EBSD data were cleaned up in AZtec software. Very small grains with a grain size of 1 pixel were removed and non-indexed pixels with a minimum of 5 identical neighbors were replaced by the same orientation. Using the EBSD map,

internal misorientation inside a grain was determined with Channel 5 software.

3.3.2. Dislocation microstructure observation

Electron transparent thin foil specimens were prepared from the thin sections parallel to the x-z plane of the Åheim peridotite samples. The x-z plane thin sections were mechanically thinned to around 30 μm thicknesses and optically polished with colloidal silica on both sides. Electron-transparent areas of the foil were obtained by ion thinning with an argon ion beam accelerated with 6 kV and 0.6 mA (Precision Ion Polishing System, Gatan). Dislocation microstructures in olivine were observed with the JEOL JEM-2010 TEM at the Natural Science Center for Basic Research and Development (N-BARD) of Hiroshima University, using 200 kV accelerating voltage. The dislocation density (ρ) of the olivine was calculated from TEM images by counting the number of free dislocations (N) in the measured area (S); $\rho = N / S$ (Ando et al., 1993).

To identify the Burgers vector and the slip system of dislocation, the thickness-fringe method (Ishida et al., 1980; Miyajima and Walte, 2009) was applied in weak-beam dark-field (WBDF) TEM image. The thickness-fringe method defines the Burgers vector of dislocation by counting the number of terminating thickness fringes at the extremity of dislocation from WBDF TEM images. With this method, the exact value of $\mathbf{g} \cdot \mathbf{b} = n$ (g: diffraction vector, b: Burgers vector, and n: integer) can be obtained from the TEM image as a number of terminating thickness fringes so the Burgers vector of the dislocation can be more precisely determined than the

conventional invisibility criteria, $\mathbf{g} \cdot \mathbf{b} = 0$. The slip system of the dislocation can be defined by the relationship between the Burgers vector and the dislocation direction vector.

3.4. Result

3.4.1. EBSD mapping

The results of EBSD mapping along the subgrain boundaries in the olivine are illustrated in Fig. 3.2 and summarized in Table 3.1. For most olivine subgrain boundaries, subgrain walls were subparallel to the (100) plane and rotation axes were aligned parallel to the [010] axes (Fig. 3.2), which indicates that the (001)[100] slip system was activated (Lloyd et al., 1997). 15 out of a total of 20 subgrain boundaries were identified as (001)[100] subgrain boundaries in both samples (Table 3.1). Minor slip systems of (010)[100], (0kl)[100], (100)[001], and (010)[001] were also identified from subgrain boundaries in the olivine (Table 3.1).

Table 3.1. Summary of olivine slip systems determined by the subgrain boundaries.

Slip system	Sample 447	Sample 448
(001)[100]	15	15
(010)[100]	1	4
(0kl}[100]	2	1
(100)[001]	1	-
(010)[001]	1	-

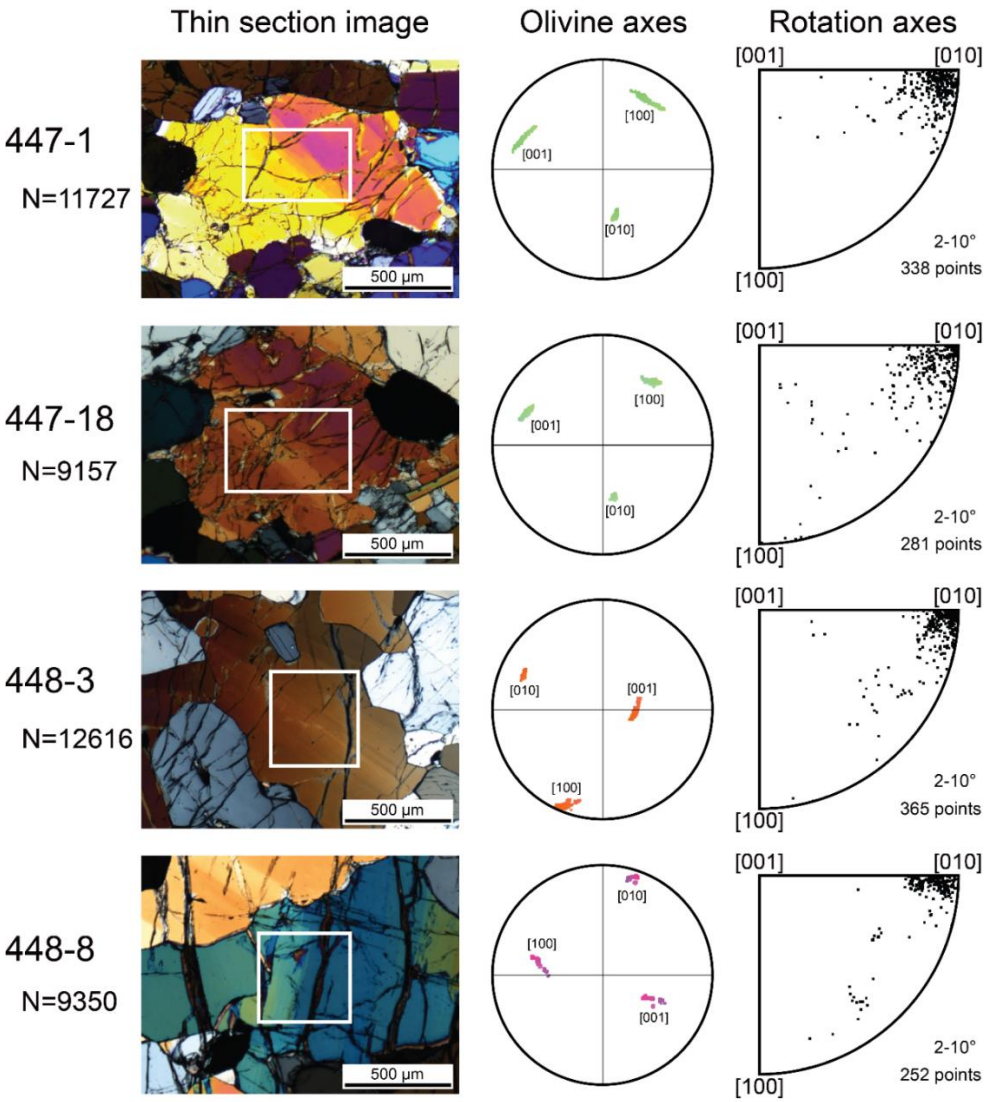

Figure 3.2. Cross-polarized light image of samples and the result of EBSD mapping for the single olivine crystal across the subgrain boundary. Olivine axes distribution is shown in the lower hemisphere stereonet pole figures, and rotation axes are illustrated in the inverse pole figure. White rectangles in the photomicrographs are the actual EBSD mapping area. [100], [010], and [001] olivine crystallographic axes are plotted in the stereonet. The rotational axes distributions with a misorientation angle of 2-10° are plotted in the inverse pole figure.

Constructed orientation map and pole figures of tremolite in the tremolite-rich layer of sample 443 (Jung et al., 2020) are illustrated in Fig. 3.3. The orientation map of tremolite showed strong shaped preferred orientation (SPO) and LPO of tremolite (Fig. 3.3A). Tremolite grains are elongated parallel to the foliation plane and [100] axes of tremolite are aligned subnormal to the foliation. The LPO of tremolite obtained by EBSD mapping was almost identical to the manually indexed result from the previous study (Jung et al., 2020); [001] axes and {010 poles of tremolite formed a girdle distribution along the foliation with some concentration of [001] axes clustered subparallel to the lineation direction and [100] axes of tremolite are aligned subnormal to the foliation (Fig. 3.3B). This LPO of tremolite can be identified as a type-III LPO of amphibole (Ko and Jung, 2015). Rotation axes of tremolite with intracrystalline misorientation angles (from 2 to 10°) are distributed along [010] and [001] direction and along [010] and [110] direction, with some concentration at [010] and [001] direction (Fig. 3.3C).

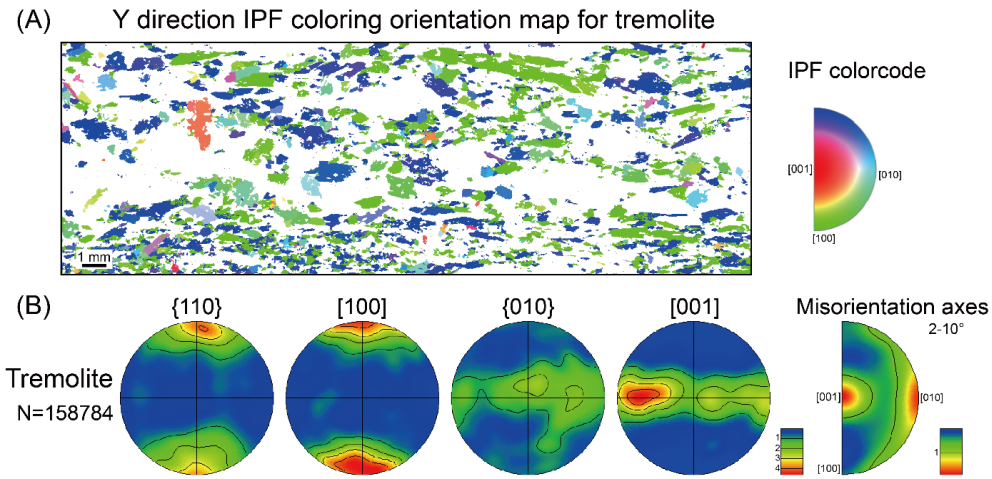

Figure 3.3. The result of EBSD mapping of the tremolite-rich layer of sample 443. (A) Y direction inverse pole figure (IPF) coloring orientation maps for tremolite. (B) Pole figure of the tremolite presented in the lower hemisphere using equal-area projection. The white line (S) represents foliation and the red dot (L) represents lineation. (C) The rotation axes distributions with a misorientation angle of 2-10° are plotted in the inverse pole figure. A half-scatter width of 20° was used. "N" represents the number of grains. The color-coding indicates the density of the data points. The numbers in the legend correspond to multiples of uniform distribution.

3.4.2. Dislocation microstructure of olivine

The Burgers vectors and the slip systems of the observed olivine dislocations are summarized in Table 3.2. TEM observation revealed that both samples had a dominant [100] edge dislocation on the (010) slip plane (Table 3.2). The average dislocation density of sample 447 and 448 were values of 2.3×10^7 and 8.4×10^6 cm^{-2}, respectively. Examples of (010)[100] dislocations are illustrated in Fig 3.4A-C for sample 447 and in Fig 3.5A-C for sample 448. Figs 3.4A-C are showing the same dislocations in different diffraction vector. The number of terminating thickness fringe for each WBDF images was +2 for Fig 3.4A (**g** = 211), +1 for Fig 3.4B (**g** = 122), and +1 for Fig 3.4C (**g** = 112). Thus the Burgers vector of this dislocation is [100] and the slip system of the dislocation is (010)[100] because dislocation was parallel to the olivine [001] axes. In case of Figs 3.5A-C, the number of terminating thickness fringe for each WBDF images were +1 for Fig 3.5A (**g** = 131), 0 for Fig 3.5B (**g** = 004), and +1 for Fig 3.5C (**g** = 140), therefore the Burgers vector of this dislocation is also [100] and the slip system is (010)[100]. In addition, the minor amount of (010)[001] (Fig 3.4D-F and Fig 3.4D-F) and (001)[100] (Fig 3.4G- I and Fig 3.5G-I) dislocations were observed from the sample (Table 3.2).

Table 3.2. Summary of olivine slip systems determined from the thickness fringe method in sample 447 and 448.

Sample	Burgers vector	Slip system	Numbers of identified dislocations			
			Foil-1	Foil-2	Foil-3	Sum
447	[100]	(010)[100]	5	7	0	12
		(001)[100]	0	0	7	7
		Screw dislocation	0	0	1	1
	[001]	(010)[001]	0	3	0	3
448	[100]	(010)[100]	5	6	0	11
		(001)[100]	0	0	4	4
		Screw dislocation	0	0	1	1
	[001]	(010)[001]	2	0	1	3

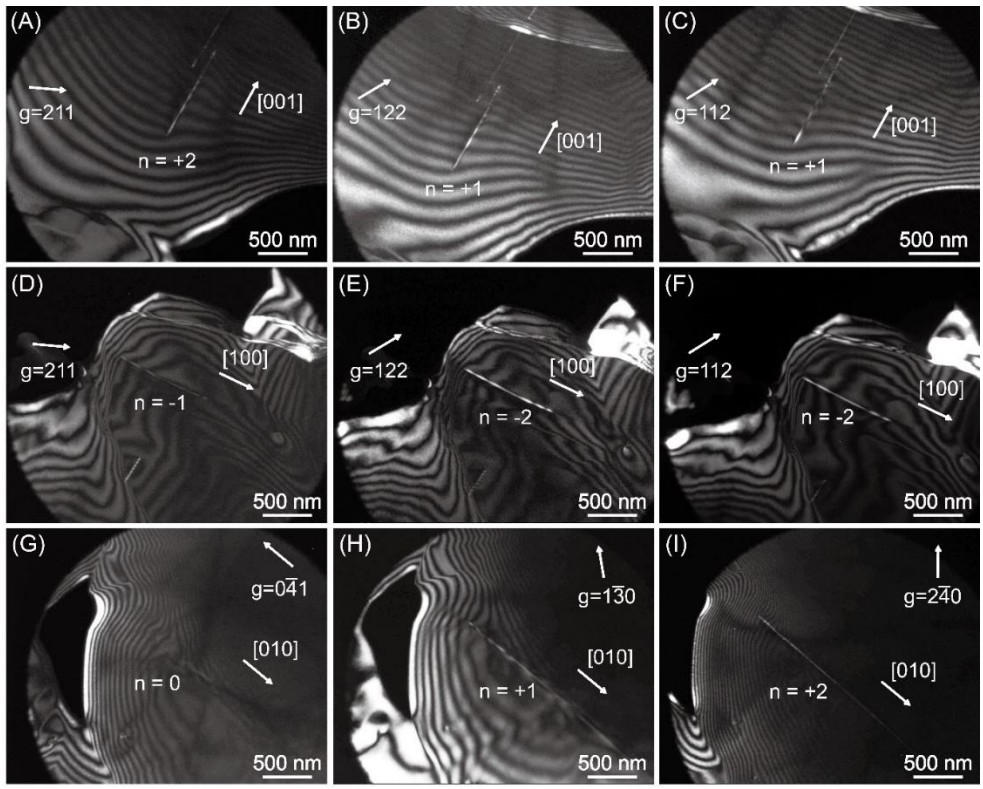

Figure 3.4. Representative weak-beam dark-field images showing dislocation microstructure of olivine in sample 447. The diffraction vectors for each image are noted as g and the white arrow and n value indicate the number of the terminating thickness fringes for each image. (A, B, C) WBDF images of the same location with different diffraction vector: **g** = 211 for (A), **g** = 122 for (B), and **g** = 112 for (C). (D, E, F) WBDF images of the same location with different diffraction vector: **g** = 211 for (D), **g** = 122 for (E), and **g** = 112 for (F). (G, H, I) WBDF images of the same location with different diffraction vector: **g** = 0$\bar{4}$1 for (G), **g** = 1$\bar{3}$0 for (H), and **g** = 2$\bar{4}$0 for (I).

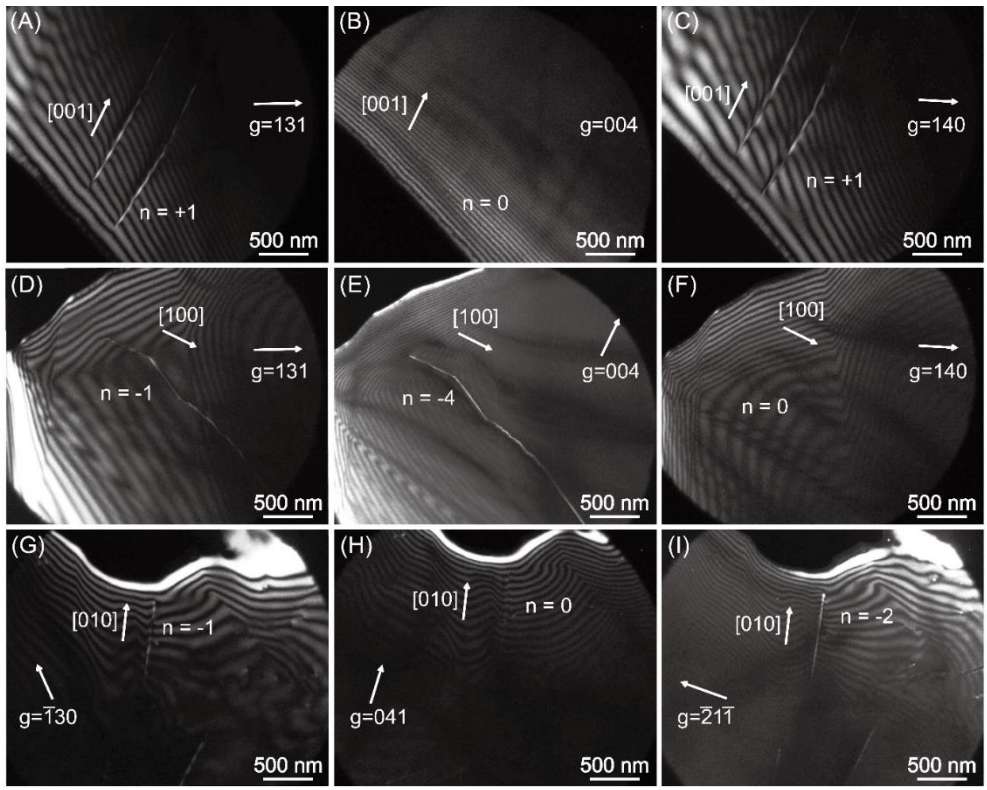

Figure 3.5. Representative weak-beam dark-field images showing dislocation microstructure of olivine in sample 448. The diffraction vectors for each image are noted as g and the white arrow and n value indicate the number of the terminating thickness fringes for each image. (A, B, C) WBDF images of the same location with different diffraction vector: **g** = 131 for (A), **g** = 004 for (B), and **g** = 140 for (C). (D, E, F) WBDF images of the same location with different diffraction vector: **g** = 131 for (D), **g** = 004 for (E), and **g** = 140 for (F). (G, H, I) WBDF images of the same location with different diffraction vector: **g** = $\bar{1}$30 for (G), **g** = 041 for (H), and **g** = $\bar{2}1\bar{1}$, for (I).

Subgrain boundary which consists of (001)[100] dislocations was observed during TEM observation on sample 448 (Fig 3.6). In Fig 3.6, the number of terminating thickness fringe for each WBDF images was +1 for Fig 3.6A ($\mathbf{g} = \bar{1}30$), 0 for Fig 3.6B ($\mathbf{g} = 041$), and +2 for Fig 3.6C ($\mathbf{g} = \bar{2}1\bar{1}$), so the Burgers vector of this dislocation is [100]. The dislocations consist of this subgrain boundary are parallel to the [010] axes, thus the slip system of these dislocations can be defined as (001)[100]. This TEM observation coincides well with the result of the EBSD mapping across the subgrain boundary.

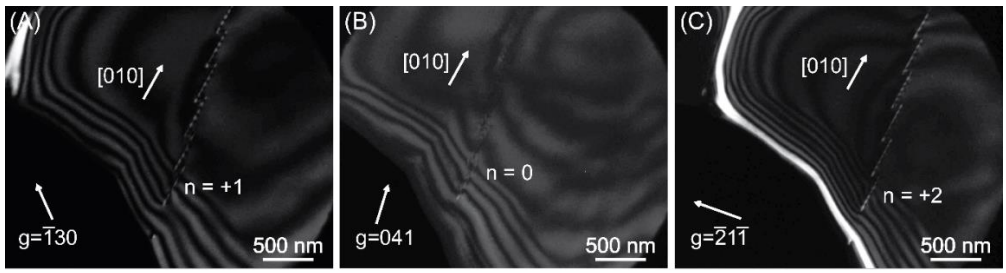

Figure 3.6. Weak-beam dark-field images showing subgrain boundary in the olivine in sample 448. The diffraction vectors for each image are noted as g and the white arrow and n value indicate the number of the terminating thickness fringes for each image. (A, B, C) WBDF images of the same location with different diffraction vector: **g** = $\bar{1}$30 for (A), **g** = 041 for (B), and **g** = $\bar{2}1\bar{1}$, for (C).

3.5. Discussion

3.5.1. Deformation mechanism of the olivine

Subgrain boundaries which consist of (001)[100] dislocations were dominant for both samples (Fig 3.3, Table 3.2). This dominant (001)[100] subgrain boundaries are reported from many other natural peridotites (Cao et al., 2014; Falus et al., 2011; Kaczmarek and Reddy, 2013; Katayama et al., 2011; Soustelle et al., 2010). One possible mechanism for this dominant (001)[100] subgrain boundary is the activation of (001)[100] slip system under water-rich condition (Katayama et al., 2011). Previous experimental researches showed that the E-type LPO of olivine, which can be related to (001)[100] slip system, is obtained under water-rich conditions (Jung et al., 2006; Katayama et al., 2004). Besides, recent experimental studies reported that the evidence of the (001)[100] slip system was observed from the olivine single crystal deformed under water-rich conditions (Tielke et al., 2019; Wang et al., 2019). The Åheim amphibole peridotite has undergone multiple stages of aqueous fluid infiltration during late Caledonian uplift and retrogressive metamorphism (Kostenko et al., 2002). The previous study on the Åheim amphibole peridotite reported that the olivines contained 370 ± 50 ppm H/Si and numerous dislocations were observed in the olivine (Jung et al., 2020). Thus the (001)[100] subgrain boundary may be formed by the deformation under water-rich conditions during the exhumation process.

The other possible mechanism for the formation of subgrain boundaries is the dominant (001)[100] subgrain boundary under low strain deformation (Hansen et al.,

2014). In the experimental study by Hansen et al. (2014), the dominant slip system determined by rotation axes gradually changed from the (001)[100] slip system to the (010)[100] slip system as strain increases. The (001)[100] subgrain boundary might be related to the low strain deformation during the late Caledonian uplift.

Free dislocations in the olivine had (010)[100] slip system with minor slip system of (010)[001] and (001)[100] (Fig. 3.4, 5; Table 3.2). Classical studies on the olivine slip system proposed that the temperature should be at least over 1000 °C to active (010)[100] slip system of olivine (Carter and Lallemant, 1970; Phakey et al., 1972) but the peak metamorphic temperature of the WGR was 800 °C (Hacker et al., 2010). However, recent deformation experiment on the single-crystal olivine showed that dislocation mobility in the (010)[100] and (010)[001] slip system of olivine is almost identical at low-stress condition, with dislocation mobility in the (010)[100] slip system slightly lower than that of (010)[001] slip system (Wang et al., 2017; Wang et al., 2016). Therefore, free dislocations with the (010)[100] slip system in the olivine can be the result of low-stress deformation during the exhumation process.

3.5.2. Deformation mechanism of the amphibole

The LPO of tremolite in the tremolite-rich layer of sample 443 obtained by EBSD mapping showed that the [001] axes and the {010 poles of tremolite formed a girdle distribution along the foliation with some concentration of the [001] axes clustered subparallel to the lineation direction and the [100] axes of tremolite are aligned subnormal to the foliation (Fig. 3.3B). Rotation axes of tremolite showed

some concentration at the [010] direction (Fig. 3.3C), which can be interpreted as activation of (100)[001] or (001)[100] dislocation slip system in tremolite (Lloyd et al., 1997). Between these two slip systems, the (100)[001] slip system is compatible with the observed LPO of tremolite; the [001] axes of tremolite aligned subparallel to the lineation direction and [100] axes aligned subnormal to the foliation (Fig. 3.3B). In addition, the (100)[001] slip system is reported as one of the easy slip systems of amphibole from previous studies (Dollinger and Blacic, 1975; Morrison-Smith, 1976; Rooney et al., 1975; Rooney et al., 1970). Observed LPO and the rotation axes of the tremolite in the tremolite-rich layer of sample 443 suggest that the (100)[001] dislocation slip system was activated during deformation and influenced on the tremolite LPO development.

The rotation axes of tremolite also showed some concentration along the [001] axis (Fig. 3.3B). The rotation axes clustered along the [001] axis are reported in naturally deformed amphiboles from various other localities (Aspiroz et al., 2007; Elyaszadeh et al., 2018; Soret et al., 2019). To explain rotation axes clustered along the [001] axis with only dislocation creep, it requires an activation of (010)[001] and or (001)[010] dislocation slip system (Lloyd et al., 1997). However, major slip systems of amphibole reported from the previous studies are (100)[001], and (hk0)[001], with minor {1101/2<110>, (010)[001], (001)[100], and (010)[100] slip systems (Biermann and Vanroermund, 1983; Cumbest et al., 1989; Morrison-Smith, 1976; Rooney et al., 1975; Skrotzki, 1992), so (100)[010] dislocation slip system has not been reported as the easy slip system of amphibole. There is a report of the (010)[100] slip system of amphibole from the previous study (Morrison-Smith, 1976; Reynard et al., 1989), but the (010)[100] slip systems are not compatible with the

LPO of tremolite, which showed that the {010 poles of tremolite formed a girdle distribution along the foliation and the [100] axes aligned normal to the foliation (Fig. 3.3B). Soret et al. (2019) proposed that preferential microfracturing along planes including the [001] crystallographic axis together with small rigid body rotations might explain apparent intracrystalline misorientations in amphibole around the [001] rotation axis. Tremolites in sample 443 also showed abundant fractures and microfractures (Fig. 3.1E, F), so rigid body rotation along these fracture planes may be related to the rotation axes of tremolite clustered along the [001] axis.

3.5.3. Microstructural evolution of the Åheim amphibole peridotite

The result of detailed microstructural analysis on the Åheim amphibole peridotite in the previous study and this study is summarized in Table 3.3. The previous study on the microstructure of the Åheim amphibole peridotite samples revealed the evidence of the multiple stages of deformation during the Scandian Orogeny (Jung et al., 2020). The coarse grains including porphyroclasts showed A-type olivine LPO, which corresponds to the initial stage of deformation. On the other hand, recrystallized olivine grains show the B-type of olivine LPO and it represents the later stage deformation associated with the exhumation process. Unlike the LPO of olivine, the dominant slip systems of the subgrain boundaries and the free dislocations obtained from two samples are identical (Table 3.3). So, the slip systems of dislocation microstructures (free dislocation and subgrain boundaries) cannot explain what caused olivine fabric transition from the A- to B-type LPO of olivine observed from the Åheim amphibole peridotite. Instead, the olivine fabric transition

seems to be finished before the formation of subgrain boundaries and free dislocations in the olivine. The A-type olivine LPO observed from the porphyroclast can be interpreted as the original olivine fabric before the uplift process (Jung et al., 2020). During the uplift process and associated retrogression, the fluid infiltration triggered retrogression in the amphibole peridotite stability field and the recrystallization of olivine (Brueckner et al., 2010; Kostenko et al., 2002). These recrystallized olivine grains were deformed under the water-rich condition in the following stage of deformation and resulted in the B-type LPO of olivine (Jung et al., 2020). Since SPO of amphibole was well-matched with that of olivine grains (Fig. 3E, 4A), LPO of amphibole seems to have been made simultaneously with the B-type LPO of olivine.

Table 3.3. Summary of the microstructural analysis on the olivine.

Sample	LPO of olivine (Jung et al., 2020)	Dominant slip systems of subgrain boundary	Dominant slip systems of free dislocations
447	B-type	(001)[100]	(010)[100]
448 fine	B-type	(001)[100]	(010)[100]
448 coarse	A-type	(001)[100]	(010)[100]

Subgrain boundaries in the olivine observed from the Åheim amphibole peridotite (Fig 3.1) represent the secondary stage of deformation. As discussed above, the possible mechanisms of the subgrain boundary generation are the deformation under water-rich condition induced by fluid infiltration (Katayama et al., 2011; Tielke et al., 2019; Wang et al., 2019) or low strain deformation (Hansen et al., 2014). And both these two mechanisms can be interpreted as the deformation during the uplifting process. Thus, two samples were deformed under the same condition during the uplifting stage and as a result, identical subgrain boundaries were formed. However, the formation of subgrain boundaries and following dynamic recrystallizations could not change the olivine fabric from the previous stage deformation (Boneh and Skemer, 2014). Because of the low strain, the second stage deformation couldn't renew the olivine fabric but instead inherited the original olivine fabric with weakened the fabric strength (Skemer and Karato, 2008).

Because free dislocation is relatively easier to be formed than LPO and subgrain boundaries (Matsumoto and Toriumi, 1989; Yamamoto et al., 2017), free dislocations observed in the olivine can be related to the final stage of the deformation. As discussed above, the free dislocations with the (010)[100] slip system in the olivine can be interpreted as the result of low-stress deformation during the exhumation process (Wang et al., 2017; Wang et al., 2016). Relatively low dislocation density observed from the olivine also coincides with the low-stress deformation (Toriumi, 1979).

3.6. Summary

The microstructure of the amphibole peridotite samples from the Åheim, Norway reveals the evidence of the multiple stages of deformation during the Scandian Orogeny. The Åheim amphibole peridotite has porphyroclastic texture with frequent undulose extinctions and subgrain boundaries. The coarse grains including porphyroclasts show A-type olivine LPO, which corresponds to the initial stage of deformation (Jung et al., 2020). On the other hand, recrystallized olivine grains show the B-type of olivine LPO and it represents the later stage deformation associated with the fluid infiltration (Jung et al., 2020). Type-III LPO of amphibole observed from tremolite in the tremolite-rich layer of sample 443 can be interpreted as activation of (100)[001] slip system in the tremolite. The subgrain boundaries and the free dislocations in the olivines represent the final of the exhumation process. The slip systems of the subgrain boundaries determined by the EBSD mapping and TEM observation were predominantly (001)[100], which might be related to the deformation under water-rich conditions (Katayama et al., 2011) or low strain deformation (Hansen et al., 2014). TEM observation revealed that the free dislocations with (010)[100] slip system were dominant for both samples. The (010)[100] dislocations can be interpreted as the final stage deformation at low-stress condition (Wang et al., 2016).

CHAPTER 4

Microstructural analysis of the experimentally deformed amphibole in blueschist using transmission electron microscope

Abstract

Transmission electron microscopy (TEM) can provide micro- to nano-scale images and detailed information on crystalline defects. The lawsonite and epidote blueschist deformed by simple shear deformation experiments were analyzed to understand the fault-triggering mechanism in the subducting slab and the deformation mechanism of the amphibole. The microstructure of the amphibole in the experimentally deformed lawsonite blueschist and epidote blueschist was examined by TEM. TEM observation of the fault gouge consisting of glaucophane grain revealed amorphous material and nanocrystals, which can enable the initiation of the instability by reducing the frictional coefficient of the blueschist. Detailed TEM observation of the glaucophane in the epidote blueschist revealed dislocations with a Burgers vector **b** = [001].

4.1. Introduction

Transmission electron microscope (TEM) is a useful tool to image specimen micro- to nanoscale and to observe crystalline defects. It has been widely applied to various geological materials, too. For example, TEM observation on the experimental fault gouges revealed that there are amorphous materials and nanocrystalline aggregates in the vicinity of the fault plane (Green et al., 2015; Yung et al., 1990). These amorphous materials and nanocrystals are reported to enable initiation of the instability and to lubricate sliding (Han et al., 2011; Rowe et al., 2019; Yung et al., 1990). In addition, TEM has been used to observe dislocation microstructure from various minerals such as quartz (Hirth and Tullis, 1992; Mainprice et al., 1986), olivine (Carter and Lallemant, 1970; Phakey et al., 1972), amphibole (Rooney et al., 1975; Skrotzki, 1992), etc. The slip system of the dislocation can only be precisely determined by using visibility criterion with the weak-beam dark-field images obtained by TEM observation (Ishida et al., 1980; Miyajima and Walte, 2009).

Amphibole is an important mineral in the middle to lower crust and subduction zone. Deformation characteristic and the lattice preferred orientation (LPO) of the amphibole provide knowledge on the kinematics (Cao et al., 2010; Imon et al., 2004) and the seismic anisotropy of the lower crust and subduction zone (Ji et al., 2013; Ji et al., 2015; Ko and Jung, 2015; Tatham et al., 2008). Major dislocation slip systems of amphibole reported from the previous TEM studies are (100)[001], and (hk0)[001], with minor {1101/2<110>, (010)[001], (001)[100], and (010)[100] slip systems (Biermann and Vanroermund, 1983; Cumbest et al., 1989; Morrison-Smith,

1976; Rooney et al., 1975; Skrotzki, 1992). In many cases, dislocation creep governed by the dominant dislocation slip system creates LPO in minerals (Karato, 2008; Mainprice and Nicolas, 1989). However, previous studies reported that the LPO of amphibole can be developed by a variety of deformation mechanisms such as rigid body rotation (Aspiroz et al., 2007; Getsinger et al., 2013; Tatham et al., 2008), cataclastic flow (Ko and Jung, 2015; Nyman et al., 1992), or diffusional creep (dissolution–precipitation creep) (Getsinger and Hirth, 2014; Imon et al., 2004). Even though there is some reports of LPO of amphibole related to the dislocation creep from natural amphibole sample (Cao et al., 2010; Elyaszadeh et al., 2018) the study on the relationship between the dislocation slip system and the LPO of amphibole deformed by high-pressure experiment is still limited.

In this study, the lawsonite blueschist which were deformed by simple shear deformation experiments was studied to understand the fault-triggering mechanism in the subducting slab. In addition, epidote blueschist which were deformed by simple shear deformation experiments were studied the deformation mechanism of the amphibole. The microstructure of the amphibole (glaucophane) in the experimentally deformed lawsonite blueschist and epidote blueschist was analyzed by using TEM. To find amorphous materials and nanocrystals, we performed TEM observation on the fault gouge crosscutting the glaucophane grain. In addition, the slip system of the dislocation microstructure in the glaucophane aggregates was determined by TEM observation.

4.2. Experimental method

4.2.1. Starting material

For starting material, natural lawsonite and epidote samples with massive texture and fine grain size were used (Fig. 4.1). The lawsonite blueschist sample was collected from Panoche Pass Road, California, USA. The lawsonite blueschist was mainly composed of glaucophane (~55%), lawsonite (~35%), and minor minerals (10%) such as titanite, omphacite, and chlorite (Fig. 4.1A, B). The epidote blueschist sample was collected from Voltri massif, Italy, and consisted of glaucophane (~55%) epidote (~15%), albite (~15%), titanite (~5%), chlorite (~5%), and garnet (~5%) (Fig. 4.1C, D). Both samples were core-drilled to make cylindrical rods with a diameter of 3.1 mm without any crack. Core-drilled specimens were cut at 45° and polished to the thickness of 300-400 μm for the shear deformation experiment.

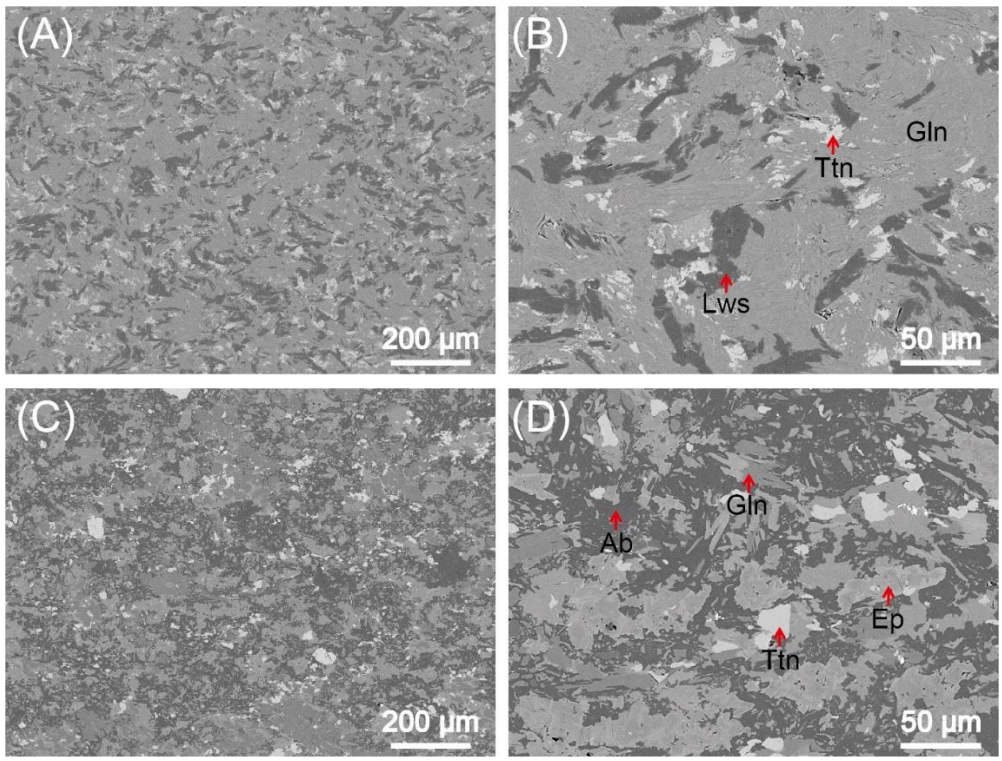

Figure 4.1. Scanning electron microscope (SEM) backscattered electron (BSE) images of the starting materials. (A) BSE image of the lawsonite blueschist sample. (B) Magnified BSE image of the lawsonite blueschist sample. Gln: glaucophane, Lws: lawsonite, Ttn: titanite. (C) BSE image of the epidote blueschist sample. (D) Magnified BSE image of the epidote blueschist sample. Gln: glaucophane, Ep: Epidote, Ab: albite, Ttn: titanite.

4.2.2. Shear deformation experiments

The samples of lawsonite blueschist and epidote blueschist was deformed at the pressure of 1-2 GPa and temperatures of 330 to 500 °C by using a modified Griggs apparatus at the School of Earth and Environmental Sciences (SEES), Seoul National University (SNU), Korea. Blueschist samples were sandwiched between two alumina pistons cut at 45° to the maximum principal stress inside Ni jacket (Fig. 4.2). The shear strain was determined by a rotation of a thin nickel strain marker placed in the center of the sample with a direction normal to the shear plane. Weak NaCl or CsCl was used as the pressure medium. During the experiments, stress and temperature were monitored with an external load cell and thermocouples (70% Pt, 30% Rh, and 94% Pt, 6% Rh), respectively. The confining pressure was increased first to target pressure over 14 hours and the temperature was increased to the target temperature over 1 hour. After reaching the target pressure and temperature, the sample was annealed at least for 1 hour to remove any possible defect produced during pressurization. The sample was deformed by moving the alumina (Al_2O_3) piston downward with a constant strain rate. After every experiment, the sample was quenched to room temperature by shutting off the power to preserve the deformation microstructures. Retrieved blueschist sample was cut along σ_1 and polished for further analysis. Experimental conditions for each experiment are noted in Table 4.1.

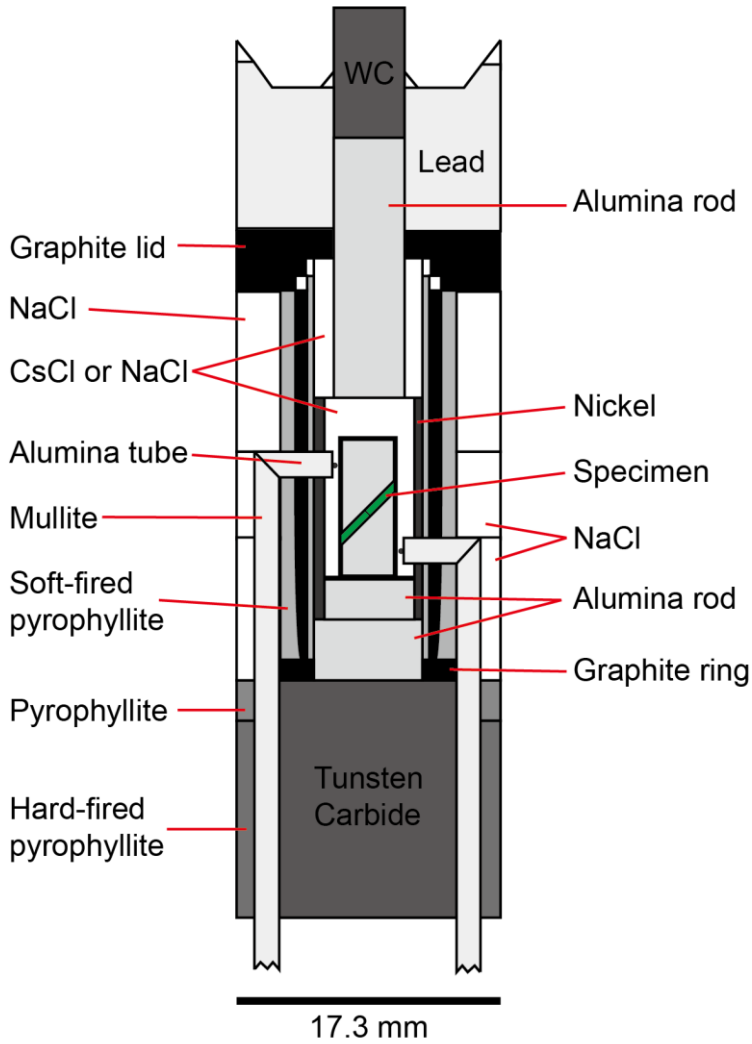

Figure 4.2. A schematic diagram showing the example of sample assembly for shear deformation experiment at high pressure and temperature. WC: Tungsten Carbide.

Table 4.1. Experimental conditions.

Run no.	Starting material*	Pressure (GPa)	Temperature (°C)	Shear strain (γ)	Shear strain rate (s^{-1})
JH98	EB	1.5	500	0.6±0.3	3.4 X 10^{-5}
JH106	LB	2.0	400	1.2±0.1	5.1 X 10^{-5}
JH113	LB	1.0	330	2.1±0.3	1.0 X 10^{-5}

*EB: epidote blueschist, LB: lawsonite blueschist.

4.2.3. TEM foil preparation

TEM foils were prepared from the retrieved sample using the focused ion beam system (FIB, Helios 650) housed at the National Center for Inter-University Research Facilities (NCIRF) of Seoul National University (SNU). FIB is a site-specific sample preparation technique that can produce thin TEM foils from the exact point of interest with a focused gallium ion beam (Wirth, 2009). To observe the microstructure of the fault gouge, TEM foils were cropped normal to the fault plane which was observed from glaucophane deformed by the high-pressure (HP) experiment (JH 106 and JH113; Fig. 4.3A). In addition, TEM foils were cropped from glaucophane grain to observe dislocation microstructure in the glaucophane deformed by the HP experiments (JH98). The platinum protection layer was deposited on the sampling position to protect it during the FIB procedure (Fig. 4.3A). Two trenches are milled in front and back of the sampling position for taking the TEM foil out of the excavation site (Fig. 4.3 B). After excavation, TEM foil was thinned to approximately 70–80 nm and was cleaned (Fig. 4.2C). Dimensions of the TEM foil was 8–10 μm wide, 3–5 μm high. Finished TEM foil was mounted on the copper mount for TEM observation (Fig. 4.3D).

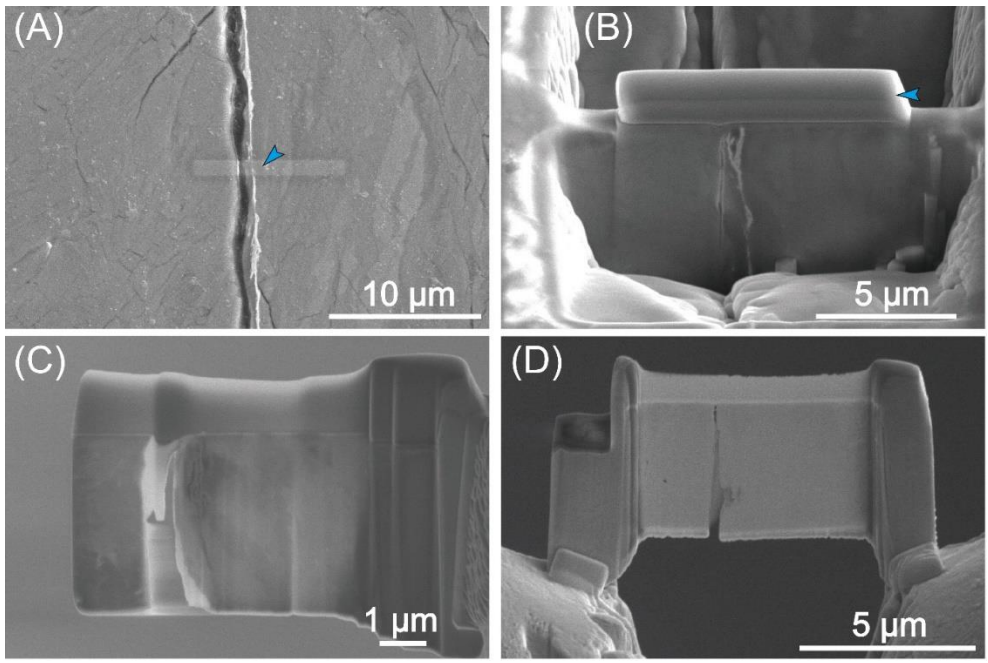

Figure 4.3. Procedure for preparing TEM foil by using FIB. All images are taken by FE-SEM attached to the FIB (Helios 650). (A) Sample surface (JH113) with the location of the TEM foil to be cropped. Blue arrow marks the platinum protection layer deposited on the sampling position. (B) TEM foil excavation site. Two trenches are milled in front and back of the sampling position. Blue arrow marks the platinum protection layer. (C) TEM foil in a thinning process. (D) Prepared TEM foil mounted on the Cu sample holder.

4.2.4. TEM observation

Deformation microstructures of the fault zone were observed with HR-TEM (JEM-3010) housed at NCIRF of SNU. All TEM images are bright-field images obtained with 300 kV accelerating voltage. Selected area diffraction (SAD) patterns were acquired to identify amorphous material in the fault gouge and to determine the crystallographic orientation of glaucophane. To identify the Burgers vector and the slip system of dislocation, invisibility criterion was applied in dark-field (DF) images obtained from HR-TEM observation. The visibility of the dislocation increases as n = $\mathbf{g} \cdot \mathbf{b}$ increases (n: integer, g: diffraction vector, and b: Burgers vector). When $\mathbf{g} \cdot \mathbf{b} = 0$, the dislocation is invisible in the DF images. So, Burgers vector of the dislocation can be determined by comparing the visibility of the given dislocation between several DF images with different diffraction vector.

4.3. Result

4.3.1. Amorphous material and nanocrystal

TEM images of the fault gouge observed from the experimentally deformed glaucophane are shown in Fig. 4.4. TEM observation revealed amorphous material in the vicinity of the fault plane (Fig. 4.4A, C). SAD pattern from the glaucophane showed diffuse ring diffraction patterns with some or no discrete reflections (Fig. 4.4B, D), which is expected diffraction pattern from the amorphous material. In

addition, nanocrystals with a size of 10-20 nm were found in the middle of amorphous material (Fig. 4.4B).

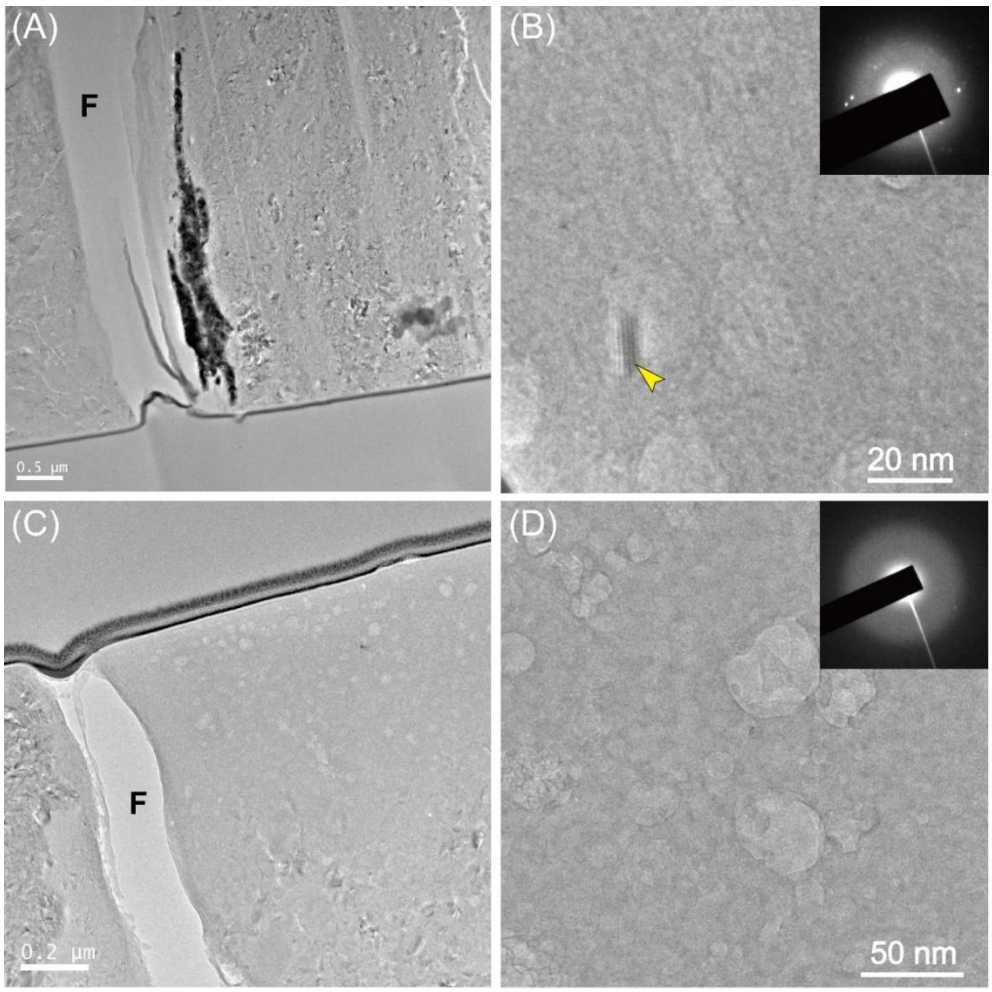

Figure 4.4. TEM images of the fault gouges produced by HP-experiment. All TEM images are bright-field images taken by HR-TEM. (A) HR-TEM image showing a wide view of fault gouge in the JH113. The fault plane is marked as "F". (B) HR-TEM image of amorphous glaucophane and glaucophane nanocrystal (yellow arrow) in the JH113 and SAD pattern obtained from the same location. (C) HR-TEM image showing a wide view of fault gouge in the JH106. The fault plane is marked as an "F". (D) HR-TEM image of the amorphous glaucophane in the JH106 and SAD pattern obtained from the same location.

4.3.2. Dislocation microstructure of glaucophane

TEM images of glaucophane deformed under the HP experiment are illustrated in Fig. 4.5. Abundant tilt boundary and free dislocations were observed from the glaucophane (Fig. 4.5A, B). The dislocations were visible in the DF image with diffraction vector **g** = 101 (Fig. 4.5C) but out of a contrast in the DF image with diffraction vector **g** = 020 (Fig. 4.5D) or **g** = 150 (Fig. 4.5E). Therefore, the Burgers vector of the dislocations would be **b** = [001]. The curved or looped dislocations was observed from the glaucophane (Fig. 4.5F).

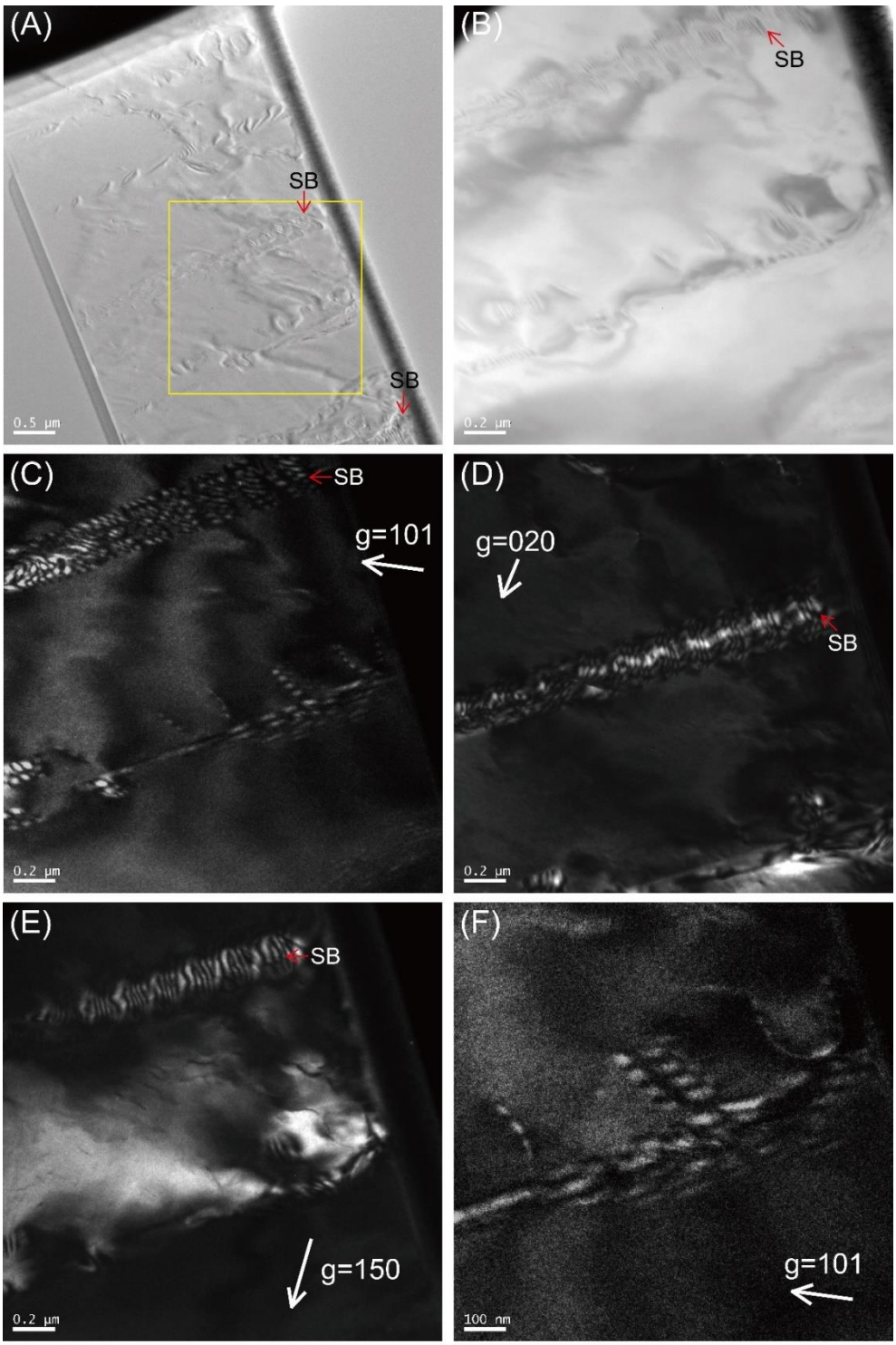

Figure 4.5. Representative HR-TEM images showing dislocation microstructure of glaucophane in the JH98. (A) BF image showing a wide view. The location of (B) is

marked as a yellow rectangle. SB: subgrain boundary. (B) BF image of the dislocation and tilt boundary observed from glaucophane. SB: subgrain boundary. (C, D, E) DF images of the same location with different diffraction vector: **g** = 101 for (C), **g** = 020 for (D), and **g** = 150 for (E). The diffraction vectors for each image are noted as g and the white. (F) Curved dislocation observed from glaucophane.

4.4. Discussion

4.4.1. Microstructure of the fault plane

Amorphous material and nanocrystals were found in the vicinity of the fault plane by the TEM observation (Fig. 4.4). The presence of the amorphous material and nanocrystals in the fault gouge may reduce friction coefficients of the blueschist, which leads to the slip weakening (Han et al., 2011; Rowe et al., 2019; Yung et al., 1990). Lawsonite blueschist is believed to be stable at the cold subduction zones such as NE Japan or Alaska (Hacker et al., 2003b; Peacock and Wang, 1999). Reduction of a frictional coefficient related to the amorphous material and nanocrystals in the fault gouge observed from the lawsonite blueschist can be the fault-triggering mechanism for the shallow- and intermediate-depth earthquake observed from cold subduction zones (Han et al., 2011; Rowe et al., 2019; Yung et al., 1990).

4.4.2. Slip system of glaucophane

DF images of the dislocation in the glaucophane showed that the Bergers vector of the dislocation was **b** = [001] (Fig. 4.5). Previous studies on the dislocation slip system of the amphibole showed that the primary Burgers vector in clinoamphibole is [001] (Cumbest et al., 1989; Rooney et al., 1975), which coincide with this study. The (100)[001] slip system is reported as one of the major slip systems of

glaucophane from previous TEM studies (Reynard et al., 1989). In addition, the activation of the (100)[001] slip system in the glaucophane may lead to the formation of a type-I LPO of amphibole, which exhibits that the (100) poles aligned subnormal to the shear plane and the [001] axes aligned subparallel to the shear direction (Ko and Jung, 2015). Indeed there are some reports of the type-I LPO of amphibole resulted from the dominant (100)[001] slip system from the natural hornblende sample (Cao et al., 2010; Elyaszadeh et al., 2018). Dislocations with **b** = [001] observed from the experimentally deformed glaucophane aggregate can be related to the Type-I LPO of amphibole. The glaucophane in the blueschist with type-I LPO of amphibole has strong seismic anisotropy and may have a strong influence on the seismic anisotropy in the subducting slab (Kim et al., 2013a; Ko and Jung, 2015)

4.5. Summary and future work

By using TEM, the microstructure of the glaucophane in the experimentally deformed lawsonite blueschist and epidote blueschist was examined. TEM observation on the fault gouge crosscutting the glaucophane grain revealed amorphous material and nanocrystals in the vicinity of the fault plane. The presence of amorphous materials and nanocrystals in the lawsonite blueschist can be related to the fault-triggering mechanism in the cold subduction zone. In addition, dislocations with **b** = [001] were observed from the glaucophane in the epidote blueschist, which might provoke the formation of LPO of glaucophane.

For the future study, TEM observation on the fault gouge in the epidote

blueschist will be followed. The epidote blueschist is expected to be stable at the P-T condition of the warm subduction zone such as North Cascadia or Mexico (Hacker et al., 2003b; Peacock and Wang, 1999). By observing the fault gouge in the epidote blueschist, the fault-triggering mechanism in the warm-subduction zone might be identified. In addition, slip system determination for more dislocations should be followed. At the current state, the number of dislocations of which slip system is determined is not enough to determine the major slip system of glaucophane in epidote lawsonite. In addition, the slip system of the dislocation in the lawsonite blueschist will be determined to find out the dominant slip system of glaucophane in cold-subduction zone conditions.

CHAPTER 5

Conclusion

The LPO of the olivine and amphibole has been proposed as one of the major sources of the seismic anisotropy observed from the subduction zone. Because deformation in the dislocation creep may result in the LPO of minerals, understanding the relationship between the LPO and the dominant slip system of the minerals is crucial. The LPO and the dislocation slip system of the olivine and amphibole were studied to understand the deformation mechanism and microstructural evolution of the amphibole peridotites in Åheim, Norway. Additionally, TEM observation on the experimentally deformed amphibole was conducted to determine the slip system of amphibole and to observe the microstructure of the fault gouge in the lawsonite blueschist.

In the Chapter 2, the detailed microstructural analysis on the olivine and amphibole in the amphibole peridotite revealed the evidence for multiple stages of deformation during the Scandian Orogeny and subsequent exhumation. The coarse grains including porphyroclasts showed an A-type LPO of olivine and it can be interpreted as the initial stage of deformation in the mantle. During the exhumation process, deformation associated with the fluid infiltration resulted in the fabric transition of olivine from A-type to C- or B-type LPO. Seismic anisotropy of the

olivine calculated with the LPO of the olivine showed that the partial fabric transition of olivine observed from the Åheim peridotite may explain the trench-parallel polarization direction of the fast shear wave in the mantle wedge and the relatively small delay time (~ 0.2 s) observed at various subduction zones such as in NE Japan or Mexico. Tremolites from the tremolite-rich layer in the amphibole peridotite showed Type-III LPO of amphibole and had stronger fabric strength than olivine. The result of seismic anisotropy of the tremolite indicates that amphibole can perform a similar role to other hydrous minerals such as serpentine and chlorite on the formation of trench-parallel seismic anisotropy in subduction zones.

In the Chapter 3, it was found that the subgrain boundaries and the dislocation microstructure of the olivine in the amphibole peridotite samples from the Åheim, Norway were resulted from the final stage of deformation during the exhumation process following the Scandian Orogeny. The subgrain boundaries in the olivine were composed of the dislocations with the (001)[100] slip system, which might be related to the deformation under water-rich condition or low strain deformation. The dominant slip system of the free dislocations was (010)[100] slip system, which can be interpreted as the result of the final stage deformation at low-stress. The EBSD mapping of minerals in the tremolite-rich layer revealed the possible evidence of the activation of (100)[001] slip system of tremolite and resultant type-III LPO of amphibole.

In the Chapter 4, the characteristics of the fault gouge crosscutting the glaucophane in the experimentally deformed lawsonite blueschist were examined by using the TEM. Amorphous material and nanocrystals were observed at the vicinity

of the fault plane, which can reduce the frictional coefficient of the blueschist. In addition, TEM observation of glaucophane in the experimentally deformed epidote blueschist revealed abundant dislocations with **b** = [001], which can be the evidence of the activation of dislocation creep.

In this thesis, the LPO and the dislocation slip system of olivine and amphibole were analyzed and compared to achieve true understanding of the LPO development of the minerals in the various physic-chemical conditions. Furthermore, the microstructural evolution of the natural sample during the orogenic event was identified by analyzing the LPO and dislocation slip system. Complex deformation history of the Åheim amphibole peridotites was recorded as the fabric transition of olivine and intracrystalline plasticity in the olivine and amphibole. Calculated results of seismic anisotropy revealed that the LPOs of olivine and amphibole have a strong effect on the seismic anisotropy in the subduction zone. TEM observation and the EBSD mapping of amphibole revealed the evidence of the activation of dislocation creep in amphibole leading to the development of the LPO of amphibole. In addition, a possible cause of the low friction coefficient in the deformed lawsonite blueschist was identified by using the TEM observation.

References

Abramson, E.H., Brown, J.M., Slutsky, L.J., Zaug, J., 1997. The elastic constants of San Carlos olivine to 17 GPa. Journal of Geophysical Research 102, 12,253-212,263.

Adams, B.L., Wright, S.I., Kunze, K., 1993. Orientation imaging: the emergence of a new microscopy. Metallurgical Transactions A 24, 819-831.

Almqvist, B.S.G., Mainprice, D., 2017. Seismic properties and anisotropy of the continental crust: Predictions based on mineral texture and rock microstructure. Rev. Geophys. 55, 367-433.

Andersen, T.B., 1998. Extensional tectonics in the caledonides of southern Norway, an overview. Tectonophysics 285, 333-351.

Andersen, T.B., Jamtveit, B., Dewey, J.F., Swensson, E., 1991. Subduction and eduction of continental crust: major mechanisms during continent-continent collision and orogenic extensional collapse, a model based on the south Norwegian Caledonides. Terr. Nova 3, 303-310.

Ando, J., Fujino, K., Takeshita, T., 1993. Dislocation microstructures in naturally deformed silicate garnets. Phys. Earth Planet. Inter. 80, 105-116.

Ashby, M.F., Verral, R.A., 1973. Diffusion accommodated flow and superplasticity. Acta Metallurgica 21, 149-163.

Aspiroz, M.D., Lloyd, G.E., Fernandez, C., 2007. Development of lattice preferred orientation in clinoamphiboles deformed under low-pressure metamorphic conditions. A SEM/EBSD study of metabasites from the Aracena metamorphic belt (SW Spain). Journal of Structural Geology 29, 629-645.

Audet, P., Bostock, M.G., Christensen, N.I., Peacock, S.M., 2009. Seismic evidence for overpressured subducted oceanic crust and megathrust fault sealing. Nature 457, 76-78.

Austrheim, H., 2013. Fluid and deformation induced metamorphic processes around Moho beneath continent collision zones: Examples from the exposed root zone of the Caledonian mountain belt, W-Norway. Tectonophysics 609, 620-635.

Austrheim, H., Corfu, F., Bryhni, I., Andersen, T.B., 2003. The Proterozoic Hustad igneous complex: a low strain enclave with a key to the history of the Western Gneiss Region of Norway. Precambrian Res. 120, 149-175.

Behr, W.M., Smith, D., 2016. Deformation in the mantle wedge associated with Laramide flat-slab subduction. Geochem. Geophys. Geosyst. 17, 2643-2660.

Ben Ismail, W., Mainprice, D., 1998. An olivine fabric database: an overview of upper mantle fabrics and seismic anisotropy. Tectonophysics 296, 145-157.

Beyer, E.E., Brueckner, H.K., Griffin, W.L., O'Reilly, S.Y., 2012. Laurentian Provenance of Archean Mantle Fragments in the Proterozoic Baltic Crust of the Norwegian Caledonides. Journal of Petrology 53, 1357-1383.

Bezacier, L., Reynard, B., Bass, J.D., Sanchez-Valle, C., Van de Moortele, B.V., 2010. Elasticity of antigorite, seismic detection of serpentinites, and anisotropy in subduction zones. Earth and Planetary Science Letters 289, 198-208.

Biermann, C., Vanroermund, H.L.M., 1983. Defect structures in naturally deformed clinoamphiboles - a TEM study. Tectonophysics 95, 267-278.

Boneh, Y., Morales, L.F.G., Kaminski, E., Skemer, P., 2015. Modeling olivine CPO evolution with complex deformation histories: Implications for the interpretation of seismic anisotropy in the mantle. Geochem. Geophys. Geosyst. 16, 3436-3455.

Boneh, Y., Skemer, P., 2014. The effect of deformation history on the evolution of olivine CPO. Earth and Planetary Science Letters 406, 213-222.

Brown, J.M., Abramson, E.H., 2016. Elasticity of calcium and calcium-sodium amphiboles. Phys. Earth Planet. Inter. 261, 161-171.

Brueckner, H.K., Carswell, D.A., Griffin, W.L., Medaris, L.G., Van Roermund, H.L.M., Cuthbert, S.J., 2010. The mantle and crustal evolution of two garnet peridotite suites from the Western Gneiss Region, Norwegian Caledonides: An isotopic investigation. Lithos 117, 1-19.

Bunge, H.-J., 1982. Texture Analysis in Materials Science: Mathematical Models. Butterworths, London.

Cao, S.Y., Liu, J.L., Leiss, B., 2010. Orientation-related deformation mechanisms of naturally deformed amphibole in amphibolite mylonites from the Diancang Shan, SW Yunnan, China. Journal of Structural Geology 32, 606-622.

Cao, Y., Jung, H., Song, S., Park, M., Jung, S., Lee, J., 2014. Plastic deformation and seismic implications in a fore-arc mantle: Constraints from microstructures, petrofabrics, mineral composition, and water contents in the Yushigou harzburgites from the North Qilian suture zone, NW China. Journal of Petrology In press.

Cao, Y., Jung, H., Song, S.G., 2017. Olivine fabrics and tectonic evolution of fore-arc mantles: A natural perspective from the Songshugou dunite and harzburgite in the Qinling orogenic belt, central China. Geochem. Geophys. Geosyst. 18, 907-934.

Cao, Y., Jung, H., Song, S.G., Park, M., Jung, S., Lee, J., 2015. Plastic Deformation and Seismic Properties in Fore-arc Mantles: A Petrofabric Analysis of the Yushigou Harzburgites, North Qilian Suture Zone, NW China. Journal of

Petrology 56, 1897-1943.

Cao, Y., Song, S.G., Su, L., Jung, H., Niu, Y.L., 2016. Highly refractory peridotites in Songshugou, Qinling orogen: Insights into partial melting and melt/fluid-rock reactions in forearc mantle. Lithos 252, 234-254.

Carswell, D.A., 1986. The metamorphic evolution of Mg-Cr type Norwegian garnet peridotites. Lithos 19, 279-297.

Carter, N.L., Lallemant, H.G.A., 1970. High temperature flow of dunite and peridotite. Geological Society of America Bulletin 81, 2181-&.

Chatzaras, V., Kruckenberg, S.C., Cohen, S.M., Medaris, L.G., Withers, A.C., Bagley, B., 2016. Axial-type olivine crystallographic preferred orientations: The effect of strain geometry on mantle texture. Journal of Geophysical Research-Solid Earth 121, 4895-4922.

Cordellier, F., Boudier, F., Boullier, A.M., 1981. Structural study of the Almklovdalen peridotite massif (southern-Norway). Tectonophysics 77, 257-281.

Cumbest, R.J., Vanroermund, H.L.M., Drury, M.R., Simpson, C., 1989. Burgers vector determination in clinoamphibole by computer-simulation. Am. Miner. 74, 586-592.

Demouchy, S., Mussi, A., Barou, F., Tommasi, A., Cordier, P., 2014. Viscoplasticity of polycrystalline olivine experimentally deformed at high pressure and 900 degrees C. Tectonophysics 623, 123-135.

Dobrzhinetskaya, L.F., Eide, E.A., Larsen, R.B., Sturt, B.A., Tronnes, R.G., Smith, D.C., Taylor, W.R., Posukhova, T.V., 1995. Microdiamond in high-grade metamorhic rocks of the Western Gneiss Region, Norway. Geology 23, 597-600.

Dollinger, G., Blacic, J.D., 1975. Deformation mechanisms in experimentally and

naturally deformed amphiboles. Earth and Planetary Science Letters 26, 409-416.

Elyaszadeh, R., Prior, D.J., Sarkarinejad, K., Mansouri, H., 2018. Different slip systems controlling crystallographic preferred orientation and intracrystalline deformation of amphibole in mylonites from the Neyriz mantle diapir, Iran. Journal of Structural Geology 107, 38-52.

Evans, B.W., 1977. Metamorphism of alpine metaperidotite and serpentinite. Annual Review of Earth and Planetary Sciences 5, 397-447.

Falus, G., Tommasi, A., Soustelle, V., 2011. The effect of dynamic recrystallization on olivine crystal preferred orientations in mantle xenoliths deformed under varied stress conditions. Journal of Structural Geology 33, 1528-1540.

Frese, K., Trommsdorff, V., Kunze, K., 2003. Olivine 100 normal to foliation: lattice preferred orientation in prograde garnet peridotite formed at high H2O activity, Cima di Gagnone (Central Alps). Contrib. Mineral. Petrol. 145, 75-86.

Fumagalli, P., Poli, S., 2005. Experimentally determined phase relations in hydrous peridotites to 6.5 GPa and their consequences on the dynamics of subduction zones. Journal of Petrology 46, 555-578.

Gee, D.G., 1975. Tectonic model for central part of Scandinavian Caledonides. Am. J. Sci. A275, 468-515.

Getsinger, A.J., Hirth, G., 2014. Amphibole fabric formation during diffusion creep and the rheology of shear zones. Geology 42, 535-538.

Getsinger, A.J., Hirth, G., Stunitz, H., Goergen, E.T., 2013. Influence of water on rheology and strain localization in the lower continental crust. Geochem. Geophys. Geosyst. 14, 2247-2264.

Gifkins, R.C., 1970. Optical Microscopy of Metals. Elsevier, New York.

Goldsby, D.L., Kohlstedt, D.L., 2001. Superplastic deformation of ice: Experimental observations. Journal of Geophysical Research-Solid Earth 106, 11017-11030.

Green, H.W., Shi, F., Bozhilov, K., Xia, G., Reches, Z., 2015. Phase transformation and nanometric flow cause extreme weakening during fault slip. Nat. Geosci. 8, 484-U491.

Hacker, B.R., 2007. Ascent of the ultrahigh-pressure Western Gneiss Region, Norway. Geological Society of America Special Papers 419, 171-184.

Hacker, B.R., Abers, G.A., Peacock, S.M., 2003a. Subduction factory - 1. Theoretical mineralogy, densities, seismic wave speeds, and H2O contents. Journal of Geophysical Research-Solid Earth 108, 26.

Hacker, B.R., Andersen, T.B., Johnston, S., Kylander-Clark, A.R.C., Peterman, E.M., Walsh, E.O., Young, D., 2010. High-temperature deformation during continental-margin subduction & exhumation: The ultrahigh-pressure Western Gneiss Region of Norway. Tectonophysics 480, 149.

Hacker, B.R., Peacock, S.M., Abers, G.A., Holloway, S.D., 2003b. Subduction factory - 2. Are intermediate-depth earthquakes in subducting slabs linked to metamorphic dehydration reactions? Journal of Geophysical Research-Solid Earth 108, 20.

Han, R., Hirose, T., Shimamoto, T., Lee, Y., Ando, J., 2011. Granular nanoparticles lubricate faults during seismic slip. Geology 39, 599-602.

Hansen, L.N., Zhao, Y.H., Zimmerman, M.E., Kohlstedt, D.L., 2014. Protracted fabric evolution in olivine: Implications for the relationship among strain, crystallographic fabric, and seismic anisotropy. Earth and Planetary Science Letters 387, 157-168.

Hansen, L.N., Zimmerman, M.E., Kohlstedt, D.L., 2011. Grain boundary sliding in

San Carlos olivine: Flow law parameters and crystallographic-preferred orientation. Journal of Geophysical Research-Solid Earth 116, 16.

Hejrani, B., Balling, N., Jacobsen, B.H., England, R., 2017. Upper-mantle velocities below the Scandinavian Mountains from P- and S-wave traveltime tomography. Geophysical Journal International 208, 177-192.

Hess, H.H., 1964. Seismic Anisotropy of the Uppermost Mantle under Oceans. Nature 203, 629-&.

Hirth, G., Kohlstedt, D., 2003. Rheology of the Upper Mantle and the Mantle Wedge: A View from the Experimentalists. Geophysical Monograph 138, 83-105.

Hirth, G., Tullis, J., 1992. Dislocation creep regimes in quartz aggregates. Journal of Structural Geology 14, 145-159.

Holtzman, B.K., Kohlstedt, D.L., Zimmerman, M.E., Heidelbach, F., Hiraga, T., Hustoft, J., 2003. Melt segregation and strain partitioning: Implications for seismic anisotropy and mantle flow. Science 301, 1227-1230.

Huang, Z.C., Zhao, D.P., Wang, L.S., 2011. Shear wave anisotropy in the crust, mantle wedge, and subducting Pacific slab under northeast Japan. Geochem. Geophys. Geosyst. 12, 17.

Imon, R., Okudaira, T., Kanagawa, K., 2004. Development of shape- and lattice-preferred orientations of amphibole grains during initial cataclastic deformation and subsequent deformation by dissolution-precipitation creep in amphibolites from the Ryoke metamorphic belt, SW Japan. Journal of Structural Geology 26, 793-805.

Ishida, Y., Ishida, H., Kohra, K., Ichinose, H., 1980. Determination of the Burgers vector of a dislocation by weak-beam imaging in a HVEM. Philos. Mag. A-Phys. Condens. Matter Struct. Defect Mech. Prop. 42, 453-462.

Jamtveit, B., Carswell, D.A., Mearns, E.W., 1991. Chronology of the high-pressure metamorphism of Norwegian garnet peridotites pyroxenites. J. Metamorph. Geol. 9, 125-139.

Ji, S.C., Shao, T.B., Michibayashi, K., Long, C.X., Wang, Q., Kondo, Y., Zhao, W.H., Wang, H.C., Salisbury, M.H., 2013. A new calibration of seismic velocities, anisotropy, fabrics, and elastic moduli of amphibole-rich rocks. Journal of Geophysical Research-Solid Earth 118, 4699-4728.

Ji, S.C., Shao, T.B., Michibayashi, K., Oya, S., Satsukawa, T., Wang, Q., Zhao, W.H., Salisbury, M.H., 2015. Magnitude and symmetry of seismic anisotropy in mica- and amphibole-bearing metamorphic rocks and implications for tectonic interpretation of seismic data from the southeast Tibetan Plateau. Journal of Geophysical Research-Solid Earth 120, 6404-6430.

Jung, H., 2009. Deformation fabrics of olivine in Val Malenco peridotite found in Italy and implications for the seismic anisotropy in the upper mantle. Lithos 109, 341-349.

Jung, H., 2011. Seismic anisotropy produced by serpentine in mantle wedge. Earth and Planetary Science Letters 307, 535-543.

Jung, H., 2017. Crystal preferred orientations of olivine, orthopyroxene, serpentine, chlorite, and amphibole, and implications for seismic anisotropy in subduction zones: a review. Geosci. J. 21, 985-1011.

Jung, H., Karato, S., 2001a. Water-Induced Fabric Transitions in Olivine. Science 293, 1460-1463.

Jung, H., Karato, S., 2001b. Effects of water on dynamically recrystallized grain-size of olivine. Journal of Structural Geology 23, 1337-1344.

Jung, H., Katayama, I., Jiang, Z., Hiraga, T., Karato, S., 2006. Effect of water and

stress on the lattice-preferred orientation of olivine. Tectonophysics 421, 1-22.

Jung, H., Lee, J., Ko, B., Jung, S., Park, M., Cao, Y., Song, S.G., 2013. Natural type-C olivine fabrics in garnet peridotites in North Qaidam UHP collision belt, NW China. Tectonophysics 594, 91-102.

Jung, H., Mo, W., Green, H.W., 2009. Upper mantle seismic anisotropy resulting from pressure-induced slip transition in olivine. Nat. Geosci. 2, 73-77.

Jung, S., Jung, H., Austrheim, H., 2014. Characterization of olivine fabrics and mylonite in the presence of fluid and implications for seismic anisotropy and shear localization. Earth Planets Space 66, 21.

Jung, S., Jung, H., Austrheim, H., 2020. Microstructural Evolution of Amphibole Peridotites in Åheim, Norway, and the Implications for Seismic Anisotropy in the Mantle Wedge. Minerals 10, 345.

Kaczmarek, M.A., Reddy, S.M., 2013. Mantle deformation during rifting: Constraints from quantitative microstructural analysis of olivine from the East African Rift (Marsabit, Kenya). Tectonophysics 608, 1122-1137.

Kang, H., Jung, H., 2019. Lattice-preferred orientation of amphibole, chlorite, and olivine found in hydrated mantle peridotites from Bjørkedalen, southwestern Norway, and implications for seismic anisotropy. Tectonophysics 750, 137-152.

Karato, S., 1987. Scanning Electron Microscope Observation of Dislocations in Olivine. Phys. Chem. Miner. 14, 245-248.

Karato, S., 2008. Deformation of Earth Materials: An Introduction to the Rheology of Solid Earth. Cambridge University Press, New York.

Karato, S., Jung, H., Katayama, I., Skemer, P., 2008. Geodynamic Significance of Seismic Anisotropy of the Upper Mantle: New Insights from Laboratory Studies. Annual Review of Earth and Planetary Sciences 36, 59-95.

Katayama, I., Hirauchi, H., Michibayashi, K., Ando, J., 2009. Trench-parallel anisotropy produced by serpentine deformation in the hydrated mantle wedge. Nature 461, 1114-1117.

Katayama, I., Jung, H., Karato, S., 2004. New type of olivine fabric from deformation experiments at modest water content and low stress. Geology 32, 1045-1048.

Katayama, I., Karato, S., 2006. Effect of temperature on the B- to C-type olivine fabric transition and implication for flow pattern in subduction zones. Phys. Earth Planet. Inter. 157, 33-45.

Katayama, I., Karato, S., Brandon, M., 2005. Evidence of high water content in the deep upper mantle inferred from deformation microstructures. Geology 33, 613-616.

Katayama, I., Michibayashi, K., Terao, R., Ando, J., Komiya, T., 2011. Water content of the mantle xenoliths from Kimberley and implications for explaining textural variations in cratonic roots. Geological Journal 46, 173-182.

Khisina, N.R., Wirth, R., Andrut, M., Ukhanov, A.V., 2001. Extinction and intrinsic mode of hydrogen occurrence in natural olivine: FTIR and TEM investigation. Phys. Chem. Miner. 28, 291-301.

Kim, D., Jung, H., 2015. Deformation microstructures of olivine and chlorite in chlorite peridotites from Almklovdalen in the Western Gneiss Region, southwest Norway, and implications for seismic anisotropy. International Geology Review 57, 650-668.

Kim, D., Katayama, I., Michibayashi, K., Tsujimori, T., 2013a. Deformation fabrics of natural blueschists and implications for seismic anisotropy in subducting oceanic crust. Phys. Earth Planet. Inter. 222, 8-21.

Kim, J., Jung, H., 2019. New Crystal Preferred Orientation of Amphibole Experimentally Found in Simple Shear. Geophys. Res. Lett. 46, 12996-13005.

Kim, Y., Clayton, R.W., Asimow, P.D., Jackson, J.M., 2013b. Generation of talc in the mantle wedge and its role in subduction dynamics in central Mexico. Earth and Planetary Science Letters 384, 81-87.

Kim, Y., Clayton, R.W., Jackson, J.M., 2010. Geometry and seismic properties of the subducting Cocos plate in central Mexico. Journal of Geophysical Research-Solid Earth 115, 22.

Ko, B., Jung, H., 2015. Crystal preferred orientation of an amphibole experimentally deformed by simple shear. Nat. Commun. 6, 10.

Kodaira, S., Iidaka, T., Kato, A., Park, J.O., Iwasaki, T., Kaneda, Y., 2004. High pore fluid pressure may cause silent slip in the Nankai Trough. Science 304, 1295-1298.

Kohlstedt, D.L., Goetze, C., Durham, W.B., Vandersande, J., 1976. New technique for decorating dislocations in olivine. Science 191, 1045-1046.

Koptev, A., Cloetingh, S., Burov, E., Francois, T., Gerya, T., 2017. Long-distance impact of Iceland plume on Norway's rifted margin. Scientific Reports 7, 11.

Kostenko, O., Jamtveit, B., Austrheim, H., Pollok, K., Putnis, C., 2002. The mechanism of fluid infiltration in peridotites at Almklovdalen, western Norway. Geofluids 2, 203-215.

Kumamoto, K.M., Warren, J.M., Hansen, L.N., 2019. Evolution of the Josephine Peridotite Shear Zones: 2. Influences on Olivine Cpo Evolution. Journal of Geophysical Research-Solid Earth 124, 12763-12781.

Kylander-Clark, A.R.C., Hacker, B.R., Mattinson, J.M., 2008. Slow exhumation of UHP terranes: Titanite and rutile ages of the Western Gneiss Region, Norway.

Earth and Planetary Science Letters 272, 531-540.

Lapen, T.J., Medaris, L.G., Beard, B.L., Johnson, C.M., 2009. The Sandvik peridotite, Gurskoy, Norway: Three billion years of mantle evolution in the Baltica lithosphere. Lithos 109, 145-154.

Lee, J., Jung, H., Klemd, R., Tarling, M.S., Konopelko, D., 2020. Lattice preferred orientation of talc and implications for seismic anisotropy in subduction zones. Earth and Planetary Science Letters 537, 1-11.

Lister, G.S., Paterson, M.S., Hobbs, B.E., 1978. The simulation of fabric development in plastic deformation and its application to quartzite: The model. Tectonophysics 45, 107-158.

Liu, X., Zhao, D.P., 2017. Depth-varying azimuthal anisotropy in the Tohoku subduction channel. Earth and Planetary Science Letters 473, 33-43.

Lloyd, G.E., Farmer, A.B., Mainprice, D., 1997. Misorientation analysis and the formation and orientation of subgrain and grain boundaries. Tectonophysics 279, 55-78.

Long, M.D., 2013. Constraints on subduction geodynamics from seismic anisotropy. Rev. Geophys. 51, 76-112.

Long, M.D., Becker, T.W., 2010. Mantle dynamics and seismic anisotropy. Earth and Planetary Science Letters 297, 341-354.

Long, M.D., Silver, P.G., 2008. The subduction zone flow field from seismic anisotropy: A global view. Science 319, 315-318.

Long, M.D., van der Hilst, R.D., 2006. Shear wave splitting from local events beneath the Ryukyu arc: Trench-parallel anisotropy in the mantle wedge. Phys. Earth Planet. Inter. 155, 300-312.

Long, M.D., Wirth, E.A., 2013. Mantle flow in subduction systems: The mantle

wedge flow field and implications for wedge processes. Journal of Geophysical Research-Solid Earth 118, 583-606.

Mainprice, D., 1990. A FORTRAN program to calculate seismic anisotropy from the lattice preferred orientation of minerals. Computers & Geosciences 16, 385-393.

Mainprice, D., 2007. Seismic anisotropy of the deep Earth from a mineral and rock physics perspective, in: Schubert, G. (Ed.), Treatise on Geophysics. Elsevier, Oxford, pp. 487-538.

Mainprice, D., Bouchez, J.L., Blumenfeld, P., Tubia, J.M., 1986. Dominant c slip in naturally deformed quartz: Implications for dramatic plastic softening at high temperature Geology 14, 819-822.

Mainprice, D., Ildefonse, B., 2009. Seismic Anisotropy of Subduction Zone Minerals–Contribution of Hydrous Phases, Subduction Zone Geodynamics. Springer, pp. 63–84.

Mainprice, D., Nicolas, A., 1989. Development of shape and lattice preferred orientations: application to the seismic anisotropy of the lower crust. Journal of Structural Geology 11, 175-189.

Marquardt, K., De Graef, M., Singh, S., Marquardt, H., Rosenthal, A., Koizuimi, S., 2017. Quantitative electron backscatter diffraction (EBSD) data analyses using the dictionary indexing (DI) approach: Overcoming indexing difficulties on geological materials. Am. Miner. 102, 1843-1855.

Matsumoto, K., Toriumi, M., 1989. Mechanical states of the upper mantle under the island arc as inferred from the microstructures of peridotite nodules, in: Karato, S., Toriumi, M. (Eds.), Rheology of Solids and of the Earth. Oxford Scientific Publications, New York, pp. 374–392.

Maupin, V., Agostini, A., Artemieva, I., Balling, N., Beekman, F., Ebbing, J.,

England, R.W., Frassetto, A., Gradmann, S., Jacobsen, B.H., Kohler, A., Kvarven, T., Medhus, A.B., Mjelde, R., Ritter, J., Sokoutis, D., Stratford, W., Thybo, H., Wawerzinek, B., Weidle, C., 2013. The deep structure of the Scandes and its relation to tectonic history and present-day topography. Tectonophysics 602, 15-37.

Mehl, L., Hacker, B.R., Hirth, G., Kelemen, P.B., 2003. Arc-parallel flow within the mantle wedge: evidence from the accreted Talkeetna arc, south central Alaska. Journal of Geophysical Research-Solid Earth 108, 18.

Miller, G.H., Rossman, G.R., Harlow, G.E., 1987. The natural occurrence of hydroxide in olivine. Phys. Chem. Miner. 14, 461-472.

Miyajima, N., Walte, N., 2009. Burgers vector determination in deformed perovskite and post-perovskite of CaIrO3 using thickness fringes in weak-beam dark-field images. Ultramicroscopy 109, 683-692.

Molinari, A., Canova, G.R., Ahzi, S., 1987. A self-consistent approach of the large deformation polycrstal viscoplasticity. Acta Metallurgica 35, 2983-2994.

Mookherjee, M., Mainprice, D., 2014. Unusually large shear wave anisotropy for chlorite in subduction zone settings. Geophys. Res. Lett. 41, 1506-1513.

Morrison-Smith, D.J., 1976. Transmission electron microscopy of experimentally deformed hornblende. Am. Miner. 61, 272-280.

Nagaya, T., Walker, A.M., Wookey, J., Wallis, S.R., Ishii, K., Kendall, J.M., 2016. Seismic evidence for flow in the hydrated mantle wedge of the Ryukyu subduction zone. Scientific Reports 6, 13.

Nakajima, J., Hasegawa, A., 2004. Shear-wave polarization anisotropy and subduction-induced flow in the mantle wedge of northeastern Japan. Earth and Planetary Science Letters 225, 365-377.

Nicolas, A., Christensen, N.I., 1987. Formation of anisotropy in upper mantle peridotites: A review. Geodynamics Series 16, 111–123.

Nyman, M.W., Law, R.D., Smelik, E.A., 1992. Cataclastic deformation mechanism for the development of core-mantle structures in amphibole. Geology 20, 455-458.

Ohtani, E., 2005. Water in the mantle. Elements 1, 25-30.

Ohuchi, T., Kawazoe, T., Nishihara, Y., Nishiyama, N., Irifune, T., 2011. High pressure and temperature fabric transitions in olivine and variations in upper mantle seismic anisotropy. Earth and Planetary Science Letters 304, 55-63.

Palasse, L.N., Vissers, R.L.M., Paulssen, H., Basu, A.R., Drury, M.R., 2012. Microstructural and seismic properties of the upper mantle underneath a rifted continental terrane (Baja California): An example of sub-crustal mechanical asthenosphere? Earth and Planetary Science Letters 345, 60-71.

Panozzo, R., 1984. Two-dimensional strain from the orientation of lines in a plane. Journal of Structural Geology 6, 215-221.

Park, M., Jung, H., Kil, Y., 2014. Petrofabrics of olivine in a rift axis and rift shoulder and their implications for seismic anisotropy beneath the Rio Grande rift. Isl. Arc. 23, 299-311.

Paterson, M.S., 1982. The determination of hydroxyl by infrared-absorption in quartz, silicate-glasses and similar materials. Bulletin De Mineralogie 105, 20-29.

Peacock, S.M., Christensen, N.I., Bostock, M.G., Audet, P., 2011. High pore pressures and porosity at 35 km depth in the Cascadia subduction zone. Geology 39, 471-474.

Peacock, S.M., Wang, K., 1999. Seismic consequences of warm versus cool

subduction metamorphism: Examples from southwest and northeast Japan. Science 286, 937-939.

Pera, E., Mainprice, D., Burlini, L., 2003. Anisotropic seismic properties of the upper mantle beneath the Torre Alfina area (Northern Appennines, Central Italy). Tectonophysics 370, 11-30.

Phakey, P., Dollinger, G., Christie, J., 1972. Transmission electron microscopy of experimentally deformed olivine crystals. Flow and Fracture of rocks, 117-138.

Precigout, J., Almqvist, B.S.G., 2014. The Ronda peridotite (Spain): A natural template for seismic anisotropy in subduction wedges. Geophys. Res. Lett. 41, 8752-8758.

Precigout, J., Hirth, G., 2014. B-type olivine fabric induced by grain boundary sliding. Earth and Planetary Science Letters 395, 231-240.

Prelicz, R.M., 2005. Seismic anisotropy in peridotites from the Western Gneiss Region (Norway) laboratory measurements at high PT conditions and fabric based model predictions, ETH Zürich. ETH Zürich, Switzerland.

Prior, D.J., Boyle, A.P., Brenker, F., Cheadle, M.C., Day, A., Lopez, G., Peruzzo, L., Potts, G.J., Reddy, S., Spiess, R., Timms, N.E., Trimby, P., Wheeler, J., Zetterstrom, L., 1999. The application of electron backscatter diffraction and orientation contrast imaging in the SEM to textural problems in rocks. Am. Miner. 84, 1741-1759.

Puelles, P., Abalos, B., Ibarguchi, J.I.G., Sarrionandia, F., Carracedo, M., Fernandez-Armas, S., 2016. Petrofabric and seismic properties of lithospheric mantle xenoliths from the Calatrava volcanic field (Central Spain). Tectonophysics 683, 200-215.

Qi, C., Hansen, L.N., Wallis, D., Holtzman, B.K., Kohlstedt, D.L., 2018.

Crystallographic Preferred Orientation of Olivine in Sheared Partially Molten Rocks: The Source of the "a-c Switch". Geochem. Geophys. Geosyst. 19, 316-336.

Raterron, P., Amiguet, E., Chen, J.H., Li, L., Cordier, P., 2009. Experimental deformation of olivine single crystals at mantle pressures and temperatures. Phys. Earth Planet. Inter. 172, 74-83.

Reynard, B., Gillet, P., Willaime, C., 1989. Deformation mechanisms in naturally deformed glaucophanes - A TEM and HREM study. European Journal of Mineralogy 1, 611-624.

Rickers, F., Fichtner, A., Trampert, J., 2013. The Iceland-Jan Mayen plume system and its impact on mantle dynamics in the North Atlantic region: Evidence from full-waveform inversion. Earth and Planetary Science Letters 367, 39-51.

Roberts, D., 2003. The Scandinavian Caledonides: event chronology, palaeogeographic settings and likely, modern analogues. Tectonophysics 365, 283-299.

Rooney, T.P., Riecker, R.E., Gavasci, A.T., 1975. Hornblende deformation features. Geology 3, 364-366.

Rooney, T.P., Riecker, R.E., Ross, M., 1970. Deformation twins in hornblende. Science 169, 173-&.

Root, D.B., Hacker, B.R., Gans, P.B., Ducea, M.N., Eide, E.A., Mosenfelder, J.L., 2005. Discrete ultrahigh-pressure domains in the Western Gneiss Region, Norway: implications for formation and exhumation. J. Metamorph. Geol. 23, 45-61.

Rowe, C.D., Lamothe, K., Rempe, M., Andrews, M., Mitchell, T.M., Di Toro, G., White, J.C., Aretusini, S., 2019. Earthquake lubrication and healing explained

by amorphous nanosilica. Nat. Commun. 10, 11.

Roy, C., Ritter, J.R.R., 2013. Complex deep seismic anisotropy below the Scandinavian Mountains. J. Seismol. 17, 361-384.

Savage, M.K., 1999. Seismic anisotropy and mantle deformation: What have we learned from shear wave splitting? Rev. Geophys. 37, 65-106.

Schmidt, M.W., Poli, S., 1998. Experimentally based water budgets for dehydrating slabs and consequences for arc magma generation. Earth and Planetary Science Letters 163, 361-379.

Shelly, D.R., Beroza, G.C., Ide, S., Nakamula, S., 2006. Low-frequency earthquakes in Shikoku, Japan, and their relationship to episodic tremor and slip. Nature 442, 188-191.

Silver, P.G., 1996. Seismic anisotropy beneath the continents: Probing the depths of geology. Annual Review of Earth and Planetary Sciences 24, 385-+.

Skemer, P., Hansen, L.N., 2016. Inferring upper-mantle flow from seismic anisotropy: An experimental perspective. Tectonophysics 668, 1-14.

Skemer, P., Karato, S.I., 2008. Sheared lherzolite xenoliths revisited. Journal of Geophysical Research-Solid Earth 113, 14.

Skemer, P., Katayama, I., Jiang, Z., Karato, S., 2005. The misorientation index: Development of a new method for calculating the strength of lattice-preferred orientation. Tectonophysics 411, 157-167.

Skrotzki, W., 1992. Defect structure and deformation mechanisms in naturally deformed hornblende. Phys. Status Solidi A-Appl. Res. 131, 605-624.

Smith, G.P., Wiens, D.A., Fischer, K.M., Dorman, L.M., Webb, S.C., Hildebrand, J.A., 2001. A complex pattern of mantle flow in the Lau backarc. Science 292, 713-716.

Soper, N.J., Strachan, R.A., Holdsworth, R.E., Gayer, R.A., Greiling, R.O., 1992. Sinistral transpression and the closure of Iapetus. J. Geol. Soc. 149, 871-880.

Soret, M., Agard, P., Ildefonse, B., Dubacq, B., Prigent, C., Rosenberg, C., 2019. Deformation mechanisms in mafic amphibolites and granulites: record from the Semail metamorphic sole during subduction infancy. Solid Earth 10, 1733-1755.

Soto, G.L., Ni, J.F., Grand, S.P., Sandvol, E., Valenzuela, R.W., Speziale, M.G., Gonzalez, J.M.G., Reyes, T.D., 2009. Mantle flow in the Rivera-Cocos subduction zone. Geophysical Journal International 179, 1004-1012.

Soustelle, V., Manthilake, G., 2017. Deformation of olivine-orthopyroxene aggregates at high pressure and temperature: Implications for the seismic properties of the asthenosphere. Tectonophysics 694, 385-399.

Soustelle, V., Tommasi, A., Demouchy, S., Ionov, D.A., 2010. Deformation and Fluid-Rock Interaction in the Supra-subduction Mantle: Microstructures and Water Contents in Peridotite Xenoliths from the Avacha Volcano, Kamchatka. Journal of Petrology 51, 363-394.

Sundberg, M., Cooper, R.F., 2008. Crystallographic preferred orientation produced by diffusional creep of harzburgite: Effects of chemical interactions among phases during plastic flow. Journal of Geophysical Research-Solid Earth 113, 16.

Tatham, D.J., Lloyd, G.E., Butler, R.W.H., Casey, M., 2008. Amphibole and lower crustal seismic properties. Earth and Planetary Science Letters 267, 118-128.

Tielke, J., Mecklenburgh, J., Mariani, E., Wheeler, J., 2019. The Influence of Water on the Strength of Olivine Dislocation Slip Systems. Journal of Geophysical Research-Solid Earth 124, 6542-6559.

Tommasi, A., Vauchez, A., 2015. Heterogeneity and anisotropy in the lithospheric

mantle. Tectonophysics 661, 11-37.

Toriumi, M., 1979. Relation between dislocation density and subgrain size of naturally deformed olivine in peridotites. Contrib. Mineral. Petrol. 68, 181-186.

Torsvik, T.H., Cocks, L.R.M., 2005. Norway in space and time: A Centennial cavalcade. Norw. J. Geol. 85, 73-86.

van Houtte, P., Wagner, F., 1985. Development of textures by slip and twinning, inPreferred Orientation in deformed Metals and Rocks: An Introduction to Modern Texture Analysis. Academic Press, New York.

Vrijmoed, J.C., Van Roermund, H.L.M., Davies, G.R., 2006. Evidence for diamond-grade ultra-high pressure metamorphism and fluid interaction in the Svartberget Fe-Ti garnet peridotite-websterite body, Western Gneiss Region, Norway. Mineral. Petrol. 88, 381-405.

Wada, I., Behn, M.D., Shaw, A.M., 2012. Effects of heterogeneous hydration in the incoming plate, slab rehydration, and mantle wedge hydration on slab-derived H2O flux in subduction zones. Earth and Planetary Science Letters 353, 60-71.

Walpole, J., Wookey, J., Kendall, J.M., Masters, T.G., 2017. Seismic anisotropy and mantle flow below subducting slabs. Earth and Planetary Science Letters 465, 155-167.

Wang, L., Blaha, S., Kawazoe, T., Miyajima, N., Katsura, T., 2017. Identical activation volumes of dislocation mobility in the 100 (010) and 001 (010) slip systems in natural olivine. Geophys. Res. Lett. 44, 2687-2692.

Wang, L., Blaha, S., Pinter, Z., Farla, R., Kawazoe, T., Miyajima, N., Michibayashi, K., Katsura, T., 2016. Temperature dependence of 100 (010) and 001 (010) dislocation mobility in natural olivine. Earth and Planetary Science Letters 441, 81-90.

Wang, L., Miyajima, N., Kawazoe, T., Katsura, T., 2019. Activation of 100 (001) slip system by water incorporation in olivine and the cause of seismic anisotropy decrease with depth in the asthenosphere. Am. Miner. 104, 47-52.

Wang, Q., Xia, Q.K., O'Reilly, S.Y., Griffin, W.L., Beyer, E.E., Brueckner, H.K., 2013. Pressure- and stress-induced fabric transition in olivine from peridotites in the Western Gneiss Region (Norway): implications for mantle seismic anisotropy. J. Metamorph. Geol. 31, 93-111.

Wawerzinek, B., Ritter, J.R.R., Roy, C., 2013. New constraints on the 3D shear wave velocity structure of the upper mantle underneath Southern Scandinavia revealed from non-linear tomography. Tectonophysics 602, 38-54.

Wheeler, J., Prior, D.J., Jiang, Z., Spiess, R., Trimby, P.W., 2001. The petrological significance of misorientations between grains. Contrib. Mineral. Petrol. 141, 109-124.

Winger, L.A., Bradt, R.C., Hoke, J.H., 1980. Transformational Superplasticity of Bi_2WO_6 and Bi_2MoO_6. J. Am. Ceram. Soc. 63, 291-294.

Wirth, R., 2009. Focused Ion Beam (FIB) combined with SEM and TEM: Advanced analytical tools for studies of chemical composition, microstructure and crystal structure in geomaterials on a nanometre scale. Chemical Geology 261, 217-229.

Wright, S.I., Nowell, M.M., Lindeman, S.P., Camus, P.P., De Graef, M., Jackson, M.A., 2015. Introduction and comparison of new EBSD post-processing methodologies. Ultramicroscopy 159, 81-94.

Yamamoto, T., Ando, J., Tomioka, N., Kobayashi, T., 2017. Deformation history of Pinatubo peridotite xenoliths: constraints from microstructural observation and determination of olivine slip systems. Phys. Chem. Miner. 44, 247-262.

Yung, R.A., Blanpied, M.L., Tullis, T.E., Weeks, J.D., 1990. Amorphous material in high strain experimental fault gouges. Journal of Geophysical Research-Solid Earth and Planets 95, 15589-15602.

Zhao, D.P., Yu, S., Liu, X., 2016. Seismic anisotropy tomography: New insight into subduction dynamics. Gondwana Research 33, 24-43.

국문초록

맨틀 웨지와 섭입하는 슬랩에서 나타나는 지진파 비등방성은 감람석과 각섬석의 격자선호방향에 큰 영향을 받고, 전위 크리프는 격자선호방향이 형성되는데 있어서 중요한 메커니즘 중 하나이다. 따라서, 다양한 물리적-화학적 조건들 속에서의 격자선호방향의 형성을 이해하는데 있어서 격자선호방향과 전위의 슬립계를 함께 비교 분석하는 것이 필요하다. 본 박사학위 논문에서는 노르웨이 오하임 지역에서 채취한 각섬석 감람암의 미세구조 분석을 통하여 스칸디안 조산운동에 의한 각섬석 감람암의 미세구조 진화에 대하여 이해하고자 하였다. 또한 각섬석 감람암의 미세구조 분석 결과들을 섭입대 지진파 비등방성에도 적용해보았다. 추가적으로, 고압고온 암석변형실험을 통해 변형된 각섬석의 미세구조 분석을 통해 각섬석의 전위 슬립계를 결정하고 각섬석에서 나타난 단층 가우지의 미세구조를 관찰하였다. 광물의 격자선호방향은 격자후방산란회절법(EBSD)을 사용하여 결정하였고, 전위 슬립계는 투과전자현미경(TEM)을 활용하여 결정하였다.

오하임 각섬석 감람암은 거정질을 띄고 있고 아입자경계면이 흔히 나타나며 투각섬석과 같은 수화광물들이 다량 관찰된다. 미세구조 분석 결과, 오하임 각섬석 감람암이 여러 번의 과정을 거쳐 변형되었음이 드러났다. 결정이 큰 부분들에서는 A-타입의 감람석 격자선호방향이 관찰되었는데, 이는 첫번째 변형단계의 결과로 보인다. 스피넬이 나타나는 부분들에서는 B-타입과 C-타입이 혼합된 형태의 감람석 격자선호방향이 나타나는데, 물이 많은 환경에서 이루어진 두번째 변형단계로 해석할 수 있다. 재결정화가 많이 진행되어 결정 크기가 작은 부분들에서는 B-타입의 감람석 격자선호방향이 나타났는데, 이는 물이 많은 환경에서 이루어진 세번째 변형단계로 해석될 수 있다. 이러한 B-타입 감람석 격자선호방향의 관찰은 섭입대 지진파 비등방성을 이해하는데 중요하게 활용될 수 있다. 투각섬석의 격자선호방향을 바탕으로 얻어진 투각섬석의 지

진파 비등방성 계산 결과, 투각섬석이 다른 수화광물들처럼 섭입대에서 해구에 평행한 방향의 지진파 비등방성 형성에 크게 기여할 수 있음을 확인하였다.

EBSD 매핑과 TEM 관찰 결과 감람석 아입자면의 주요 전위 슬립계는 (001)[100]인 것을 확인하였다. 이 감람석 아입자면들은 감람석 내부에 물이 존재하는 상태에서의 변형이나 변위가 적은 변형으로 인해 만들어진 것으로 볼 수 있다. TEM을 활용해 두께 줄무늬 방법을 적용하여 전위의 슬립계를 결정한 결과 자유전자의 대부분이 (010)[100] 슬립계를 갖고 있음을 확인하였다. 이러한 결과들을 볼 때 감람석의 아입자면과 자유전자들이 감람암의 융기과정 중에 마지막 단계의 변형을 지시한다고 해석할 수 있다. 투각섬석에 대한 EBSD 매핑 결과, 투각섬석에서 (100)[001] 전위 슬립계로의 변형이 활발했음을 밝혀냈다.

섭입하는 슬랩에서의 단층발생 메커니즘과 각섬석(남섬석)의 변형 메커니즘을 이해하기 위하여, 단순 전단 변형 실험으로 변형된 청색편암 시료들에 대한 연구를 진행하였다. 청색편암의 TEM 분석 결과, 남섬석 결정을 끊고 나타난 단층 가우지에서 나노미터 단위의 미세 결정들과 비정질 물질들이 관찰되었다. 이들은 청색편암에서 단층이 만들어지는 원리를 규명하는데 있어서 중요한 역할을 할 수 있다. 남섬석에서 전위들이 다량 관찰되었는데, 남석석의 전위의 버거스 벡터는 [001]로 각섬석에서 흔히 나타나는 LPO와 잘 일치함을 확인하였다.

주요어: 미세구조, 격자선호방향, 전위, 슬립계, 각섬석 감람암, 지진파 비등방성

학번: 2011-30922